Fast Mesh-Based Physical Optics for Large-Scale Electromagnetic Analysis

by

Daopu Xiang

Dissertation presented for the degree of Doctor of Philosophy in the Faculty of Engineering at Stellenbosch University

Supervisor: Prof. Matthys M. Botha

December 2016

Declaration

By submitting this dissertation electronically, I declare that the entirety of the work contained therein is my own, original work, that I am the sole author thereof (save to the extent explicitly otherwise stated), that reproduction and publication thereof by Stellenbosch University will not infringe any third party rights and that I have not previously in its entirety or in part submitted it for obtaining any qualification.

This dissertation includes four original papers published in peer-reviewed journals or books and three unpublished publications. The development and writing of the papers (published and unpublished) were the principal responsibility of myself and, for each of the cases where this is not the case, a declaration is included in the dissertation indicating the nature and extent of the contributions of co-authors.

Date: ..... December 2016

Abstract

Fast Mesh-Based Physical Optics for Large-Scale Electromagnetic Analysis

D. P. Xiang

Department of Electric and Electronic Engineering,
University of Stellenbosch,
Private Bag X1, Matieland 7602, South Africa.

Dissertation: PhD

November 2016

At sufficiently high frequencies, the electrical size of scattering objects become very large. The electromagnetic field simulation of such objects becomes prohibitively expensive with physically rigorous (full wave) computational electromagnetics methods. In such cases, methods based on asymptotic assumptions can be employed instead, to approximately solve Maxwell's equations. The physical optics (PO) approximation for a conducting surface, is a well-known asymptotic assumption. The multiple-reflection PO (MRPO) method is obtained by applying the PO approximation recursively, to model multiple reflections occurring internally to an object. The overall research goal of this work is to significantly accelerate the mesh-based MRPO for electromagnetic scattering analysis. A standard representation was chosen for the surface current, namely Rao-Wilton-Glisson (RWG) basis functions on a mesh of triangle elements. Since the MRPO is an extension of the single-reflection PO (SRPO), the main bottleneck in the SRPO, namely incident field shadowing determination, is addressed first. An adaptive, multi-level, buffer-based shadowing determination algorithm is developed which is robustly optimal, yielding O(N) time-scaling results for extreme test cases (N denotes the number of mesh elements). Secondly, the first ever, comprehensively accelerated version of the mesh-based MRPO method (which rigorously takes internal shadowing into account), denoted fast MRPO (FMRPO), is developed. The FMRPO uses the multi-level, fast multipole method (MLFMM) to accelerate internal reflected field calculations. The inter-group interaction criterion of the MLFMM is altered to account for shadowing. Inter-group shadowing status flags are efficiently evaluated. The runtime scaling of the conventional MRPO is O(N^2), while the runtime of the FMRPO scales as quasi-O(N log N), depending on the specific geometry. Results are presented for practical geometries with larger electrical sizes than have ever before been considered with the MRPO, but which can now for the first time be solved in realistically fast runtimes. With the FMRPO there is no fundamental limit to the electrical size of the scattering objects that can be solved.

Opsomming

Vinnige Maas-Gebaseerde Fisiese Optika vir Grootskaalse Elektromagnetiese Analise

D. P. Xiang

Departement van Elektriese en Elektroniese Ingenieurswese,
Universiteit van Stellenbosch,
Privaatsak X1, Matieland 7602, Suid Afrika.

Proefskrif: PhD

November 2016

By genoegsaam hoë frekwensies is die elektriese grootte van verstrooiingsvoorwerpe baie groot. Die elektromagnetiese veldsimulasie van sulke voorwerpe met fisies omvattende (volgolf) numeriese elektromagnetika metodes word dan te duur. In sulke gevalle kan metodes gebaseer op asimptotiese aannames eerder ingespan word, om Maxwell se vergelykings by benadering op te los. Die fisiese optika (FO) benadering vir 'n geleidende oppervlak is 'n welbekende asimptotiese aanname. Die multi-refleksie FO (MRFO) metode word verkry deur die FO benadering rekursief toe te pas, om veelvoudige refleksies te modelleer wat intern tot 'n voorwerp plaasvind. Die hoof navorsingsdoelwit van hierdie werk is om die maas-gebaseerde MRFO noemenswaardig te versnel vir elektromagnetiese verstrooiingsanalise. 'n Standaard voorstelling is gekies vir die oppervlaktestroomdigtheid, naamlik Rao-Wilton-Glisson (RWG) basisfunksies op 'n maas van driehoek elemente. Gegee dat MRFO 'n uitbreiding van enkel-refleksie FO (ERFO) is, word die hoof bottelnek van die ERFO, naamlik invallende-veld skaduweebepaling, eerste aangespreek. 'n Aanpassingsvaardige, multivlak, buffer-gebaseerde, skaduweebepalingsalgoritme is ontwikkel wat robuust optimaal is, met O(N) tydskaleringsresultate vir uiterste toetsgevalle (N verwys na die aantal maaselemente). Tweedens is die heel eerste, omvattend versnelde weergawe van die maas-gebaseerde MRFO metode (wat interne skaduwees streng in ag neem), genoem vinnige MRFO (VMRFO), ontwikkel. Die VMRFO inkorporeer die multivlak, vinnige multipool metode (MVVMM) om interne, weerkaatste veldberekeninge te versnel. Die intergroep interaksiekriterium van die MVVMM is aangepas om skaduwees in ag te neem. Intergroep skadustatusvlaggies word doeltreffend bepaal. Die berekeningstyd van die konvensionele MRFO skaleer as O(N^2), terwyl die berekeningstyd van die VMRFO skaleer as kwasi-O(N log N), na gelang van die spesifieke geometrie. Resultate word getoon vir praktiese verstrooiingsvoorwerpe wat elektries groter is as wat ooit vantevore met die MRFO aangepak is, wat nou vir die eerste keer opgelos kan word in realisties vinnige berekeningstye. Met die VMRFO is daar geen fundamentele beperking op die elektriese grootte van die verstrooiingsvoorwerpe wat kan opgelos word nie.

Acknowledgements

I would like to express my sincere gratitude to my supervisor, Prof. Matthys Botha, for providing invaluable assistance to ultimately make this thesis a reality, who showed me the most wonderful top class research on Computational Electromagnetics. He taught me not only how to be a true scholar but also to have a rigorous attitude for all the work not limited to the research area. This thesis could not have been done without his numerous guidance and patience over the past three years.

I'm also grateful to Idesbald van den Bosch, the author of the open source project *Puma-EM*, without his sincere help and discussions on the MLFMM method and code, I could not have finished my research work quickly.

Financial support has been provided by Altair Development S.A. (Pty) Ltd, developers of the EM simulation software suite FEKO. I want to say thank you to Dr Ulrich Jakobus, the vice president of electromagnetic solutions at Altair, for providing me this opportunity to work on this topic and to gain part-time work experience at the company.

At last, I need to thank my parents and my parents in law for their endless support and love through my life. And for my wife Hui Gao, she is a great qualified partner for me, I want to express my deepest thanks for her unconditional emotional support and patience. I also want to express my big sorry to my daughter, I missed many big moments during your growing period.

Contents

Declaration i

Abstract ii

Opsomming iii

Acknowledgements iv

Contents v

1 Introduction 1
- 1.1 Overview . . . 1
- 1.2 Summary of high frequency asymptotic methods . . . 3
- 1.3 Research motivation . . . 5
- 1.4 Main objectives . . . 6
- 1.5 Original contributions . . . 7
  - 1.5.1 Fast shadowing determination for SRPO . . . 7
  - 1.5.2 Fast MRPO . . . 8
- 1.6 List of appended papers . . . 9
  - 1.6.1 Journal papers . . . 9
  - 1.6.2 Conference papers . . . 10
- 1.7 Conclusion . . . 10

Bibliography 12

A Journal paper — fast shadowing [51] 16

B Journal paper — fast shadowing [50] 23

C Journal paper — fast MRPO [52] 42

D Conference paper — fast shadowing [46] 75

E Conference paper — fast shadowing [47] 82

F Conference paper — fast MRPO [49] 89

G Conference paper — fast shadowing and MRPO [48] 96

Chapter 1

Introduction

1.1 Overview

Electromagnetic scattering analysis is relevant to many applications, including radar systems, wireless communication systems, propagation channel modelling, antenna placement, etc. [31, 5, 37]. In the low frequency and resonant regions, when the scattering object is smaller in size than the wavelength (λ) or up to a few wavelengths in size, all parts interact with each other; in the high frequency region, when the electrical size of the object is greater than roughly 10λ (electrically large), the scattering mechanisms become increasingly localized and the elements of the body are independent of one another [15]. To study scattering experimentally is very expensive, requiring specialized facilities and equipments; on the other hand, computer simulation is relatively inexpensive and typically more convenient. Electromagnetic simulation methods have been developed for many years and this technical field is referred to as computational electromagnetics (CEM).

CEM is the process of modeling the interaction of electromagnetic fields with physical objects and the environment [7]. Two classes of CEM methods exist, namely full wave (also known as exact methods) and asymptotic methods. Full wave methods are integral equation-based (for example the method of moments (MoM)) or differential equation-based (for example the finite difference time domain method (FDTD) and finite element method (FEM)). Such methods approximate solutions to the integral and differential form of Maxwell's equations respectively. These methods typically subdivide the problem of interest into a grid with cell size proportional to the wavelength, leading to a system matrix of dimension proportional to the number of cells/elements [15]. These methods thus become computationally expensive as the electrical size of the object is increased. For example, if N represents the number of elements in the MoM mesh, the memory required to store the matrix is of order N^2 and the runtime to solve the problem is of order N^3 with a direct linear equation solver.

High frequency, asymptotic methods for scattering analysis have the property that the accuracy increases, as the electrical size of features on the scatterer increases [13]. These methods can be divided into ray-based methods, such as Geometric Optics (GO) and current-based methods, based on the Physical Optics (PO) approximation. For ray-based asymptotic methods, the wave properties of electromagnetism is neglected entirely. This underlying assumption inherently implies that ray based methods work well when the

dimensions of the scatterer are very large in comparison to the wavelength, i.e. hundreds of wavelengths. Current-based asymptotic methods are intermediate methods, between ray-based methods which ignore wave effects, and full-wave electromagnetic analysis, which involves solving Maxwell's equations without physical approximations [8]. In this work, the focus is on the development of very efficient, PO-based methods, since PO can in principle, address a wide class of scattering problems of practical interest.

Since the surface current is effectively solved all over the structure with PO, its numerical representation is an important aspect in any PO-based method. Two types of surface current representations are often used in PO methods: a non-uniform rational basis spline (NURBS)-based, CAD model representation [29, 17, 16], or a mesh of triangle elements with size proportional to the wavelength, upon which standard MoM basis functions are used (e.g. [21, 53, 2]). The number of basis function coefficients will be proportional to the scatterer's surface area, as measured in square wavelengths. Working with a CAD model has the advantage that a large mesh does not need to be generated or stored. However, resolving wavelength-scale details in the current representation can be a challenge with a CAD-based approach. Here the focus is on mesh-based PO. As the underlying principles for mesh-based PO and CAD model-based PO are the same, some of the work in this thesis could possibly be extended in future to CAD model-based PO.

For multiple reflection scattering mechanisms, the work that has been published in the PO field, is limited. Multiple reflections was first treated with PO in [27]. The computational complexity is $\mathcal{O}(N^2)$, due to internal shadowing determination being required for every pair of mesh elements/basis functions, as well as due to internal reflected field calculations. For the electrically large problems asymptotic methods are intended for, this complexity is prohibitively expensive. Later on, a dramatically simplified shadowing rule (essentially geometry between an observation point and the source is ignored) was incorporated into the method in order to reduce shadowing determination cost [9, 10] — the method is called iterative PO (IPO). This opened up the possibility of convergence problems, as the IPO method requires an iterative solution, rather than being a method of strictly modeling a fixed number of physical reflections [52]. Indeed, the IPO can be viewed as an iterative solution of the magnetic field integral equation (MFIE). Convergence is not guaranteed and can thus hamper the method's practical application. Since 2001, numerous researchers have used the simplified IPO concept of [9], as basis for their work on applications or on accelerations of the method (cf. [33, 42, 34, 28]).

In order to distinguish the present work from the IPO as formulated in [9, 10], the term *multiple-reflection physical optics* (MRPO) is used. It refers to PO with multiple reflections taken into account with rigorous internal shadowing determination [27]. Thus, physical reflections are being modeled with MRPO, as opposed to an iterative process to solve the MFIE in the IPO, where the solution after each iteration does not have a clear physical interpretation.

The overall research objective of the present work is to significantly accelerate the mesh-based MRPO method. The work is divided into three sub-objectives, the first is to develop a highly efficient single-reflection PO (SRPO) solver; the second is to use the SRPO shadowing determination method to calculate the visibility information required in the MRPO method; the third and final objective is to use the multi-level fast multipole method (MLFMM) [12] to accelerate the internal field calculation in the MRPO, which requires the design of a new inter-group shadowing status calculation method, to incorporate shadowing into the MLFMM interaction tree, so as to preserve the improved

cost-scaling property of the MLFMM.

The format of this thesis is to give an overview in Chapter 1 of the research field and the research work that was done, after which all of the publications that resulted from this work are appended, as individual Appendices. These publications are referenced in the overview and they indeed serve as the primary documentation of the work. With regards to Chapter 1: Section 1.2 gives a general summary of asymptotic methods and where PO fits into this field. Section 1.3 gives a specialized motivation for the thesis research work, in the context of asymptotic methods. Section 1.4 describes the main objectives of the thesis work. Section 1.5 discusses the two main original, research contributions of the thesis. In Section 1.6, the appended papers are listed and their contents are placed into context, with regards to the original contributions of the thesis. An overall conclusion to the thesis work is given in Section 1.7.

1.2 Summary of high frequency asymptotic methods

In this section a summary is given of significant asymptotic methods, to show where PO fits into this technical field.

Various asymptotic methods exist to predict scattering characteristics and these asymptotic methods can be divided into two categories: ray-based methods (such as GO, GTD and UTD) and current-based methods (such as PO, PTD) [8].

- **Geometric optics (GO):** This method is based on ray tracing of specular reflections [8]. GO can erroneously predict infinite scattering results for flat or singly curved surfaces and does not account for diffraction.

- **Geometric theory of diffraction (GTD):** This ray tracing technique was introduced in [23] as an extension to GO, taking diffractions into account as well.

- **Uniform theory of diffraction (UTD):** This is a refinement within the GTD context [24], to yield results that are more generally applicable.

- **Shooting and bouncing rays (SBR):** This is a ray launching method, meaning that ray (tubes) are launched with sufficient density from the source, and in such directions that the whole scatterer is covered. The specular reflections are traced. Equivalent sources are placed where rays interact with the structure, or at the points where they leave an enclosing surface [25]. Integration over the equivalent sources then yields the scattered field.

  There are various significant extensions to the standard SBR formulation. Multi-resolution rays have been proposed to reduce the total number of rays that need to be launched [40]. The KD-tree scheme has been proposed to significantly accelerate the ray-patch intersection testing [41]. Fast SBR solvers are mature enough for commercial use, e.g. the SBR solver in CST [14] and the "ray-launching GO" solver in FEKO [20].

- **Physical Optics (PO):** The asymptotic, physical optics (PO) approximation relates the incident magnetic field to the induced surface current at points on a scatterer's surface with line-of-sight visibility to the source [6, 3, 39]. Since the scattered

field is obtained by integrating over these sources, no problems with infinite results, as with GO, occurs with PO. The drawbacks of PO are that it does not account for surface currents in shadowed regions and the contributions from surface waves, multiple reflections and edge diffractions are also not included. An improvement to the standard PO approximation, termed Modified PO (MPO) [38], has been proposed to enhance solutions with respect to diffraction effects.

- **Physical theory of diffraction (PTD):** This techniques was developed as an improvement to PO, adding local corrections to the uniform PO solution [43]. The incremental length diffraction coefficient (ILDC) technique [26] is an improvement to the PTD, as well as the work in [44].

- **Multiple-reflection physical optics (MRPO):** The PO approximation with rigorous, geometric shadowing is applied to the field radiated by the present current solution, to affect successive reflections [27, 52]. The MRPO models a specified number of internal reflections.

- **Iterative physical optics (IPO):** The iterative physical optics (IPO) was developed by Burkholder in [9], which is like the MRPO, but with a sweeping, simplifying assumption on shadowing determination. Geometry in between any given source basis function and an observation point is effectively ignored. This means that an IPO iteration cannot be interpreted as a physical reflection. Rather, the IPO can be understood as a Picard-type iterative solution (cf. [4]) of the magnetic field integral equation (MFIE), with partial inclusion of shadowing properties, to accelerate convergence for PO-suitable scatterers.

The relationships between these methods are shown in Figure 1.1. From the figure it can be seen that ray-based methods and current-based methods have corresponding aspects, meaning that if there is an idea in ray-based methods, then there will be an analogous idea used in current-based methods. For example, for specular reflections, GO corresponds to PO; for multiple reflections, SBR corresponds to MRPO; for diffractions, GTD/UTD corresponds to PTD. Even though MRPO is thus quite similar to SBR, there is the crucial difference that successive reflections are based on full integration over all sources in the MRPO, rather than just tracking of ray tube reflections in SBR.

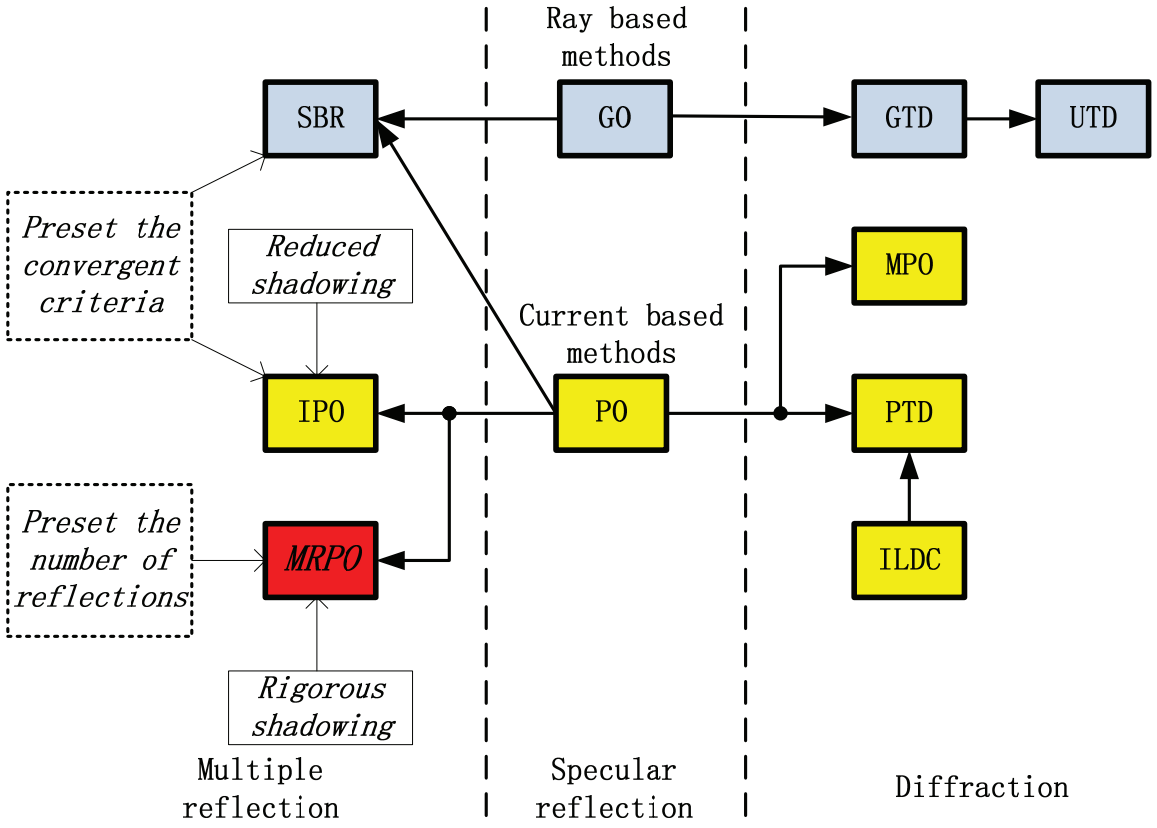

Figure 1.1: Summary of the key properties and relationships between asymptotic, high frequency methods. The MRPO is shown in red, as it is the focus of the work in this thesis. Blue refers to ray-based methods and yellow refers to current-based methods.

1.3 Research motivation

As already mentioned, electromagnetic scattering analysis is an important tool for modern engineering practice. As electrical size grows, so do asymptotic methods become more attractive than full-wave methods (MoM, FEM or FDTD), from a computational cost perspective. In the past 50 years, much effort has been poured into the methods shown in Figure 1.1. Techniques to incorporate different effects are available for ray-based as well as current-based methods. For specular reflections, no matter if ray-based SBR or current-based PO is used, they work very well for large and smooth structures which do not support significant multiple reflection mechanisms. However, for multiple reflections, the ray-based SBR and its extensions are more mature with regards to optimized implementations, than the MRPO (see the discussions in Section 1.2).

After the MRPO was introduced in 1995 [27], there has not been any performance improvements developed for the MRPO to date. Rather, its prohibitive shadowing cost scaling has caused it to not receive much further attention, even though it holds rigorously to the PO approximation (specifically with regards to shadowing), while IPO does not; and even though its accuracy will clearly be more accurate or at least the same as that of the SBR [45, 11, 16]. These points motivate the work in this thesis, which is focused on significantly accelerating the mesh-based MRPO.

1.4 Main objectives

The three main objectives which together address the overall objective of significantly accelerating the mesh-based MRPO, are listed below. Figure 1.2 illustrates the main aspects of these objectives, as well as the relationships between them. With the focus on mesh-based PO, the discretization scheme was chosen to be a conforming mesh of flat triangle elements, with edge-associated, Raviart-Thomas, mixed first-order basis functions, also known as Rao-Wilton-Glisson (RWG) basis functions [32, 30, 22]. This is a very standard, well-known and widely-adopted discretization scheme. Exploring the use of higher-order basis functions is beyond the scope of this thesis.

1. **Development and implementation of efficient SRPO:** The work starts with the SRPO, because for the MRPO, the first reflection solution is simply the SRPO solution. The first reflection is different from subsequent ones, as it involves visibility with respect to the source, rather than internal visibility for successive reflections. Apart from the substantial work involved in implementing the method in computer code, the main task here was to establish an algorithm to determine the shadowing status of all basis functions with reliable efficiency.

2. **Implementation of conventional MRPO:** After completing the SRPO objective, the next step was to use the SRPO code as a starting point for implementing the conventional MRPO; "conventional" refers to using standard integration over all visible basis functions, to calculate internally reflected fields and to base these calculations on inter-basis function shadowing information that is rigorously determined for every pair of basis functions in the mesh, using the algorithm developed for the SRPO. The purpose of the conventional MPRO implementation was firstly to establish a reference implementation for later, when considering an accelerated MRPO formulation. Secondly, the purpose was to become very well acquainted with the subtle details of the MRPO — for example, that currents must be modelled on both sides of open surfaces independently and that this leads to effectively four interaction matrices ("positive" sides with "positive" sides, "positive" sides with "negative" sides, etc.) [52].

3. **Development and implementation of fast MRPO (FMRPO):** This was the main objective of the thesis. It firstly entailed the algorithmic development of an accelerated method, based on using the MLFMM to accelerate internal, reflected field evaluations. A method was needed to incorporate internal shadowing effects into the fast MLFMM scheme without compromising its computational efficiency. This objective secondly entailed the implementation in computer code, of the fast MRPO. This implementation was a substantial task [52].

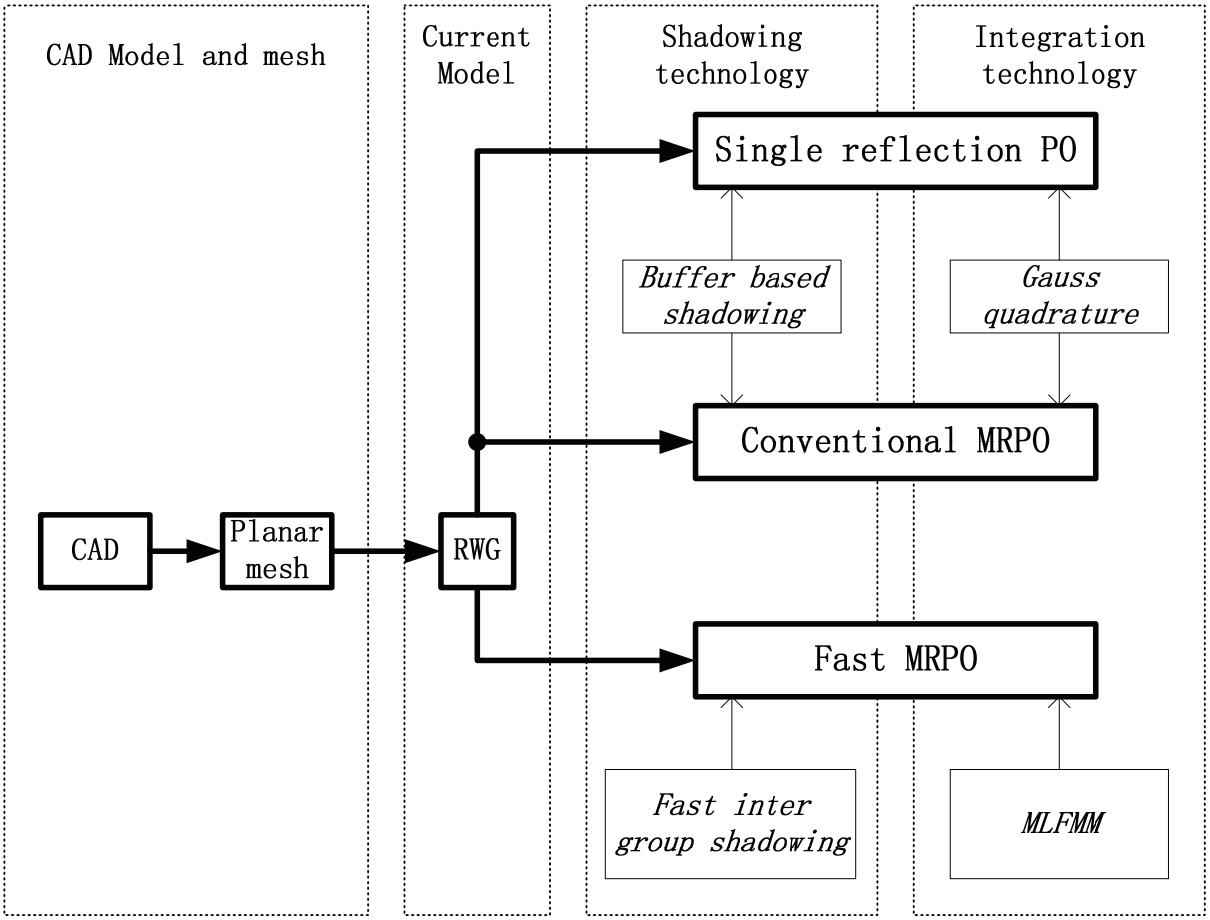

Figure 1.2: Main framework of thesis objectives.

1.5 Original contributions

This thesis makes two main, original contributions. These are now each discussed. References to the appended papers are provided, where the details of this work are documented.

1.5.1 Fast shadowing determination for SRPO

Shadowing determination constitutes the dominant contribution to the mesh-based SRPO runtime and can be very time-consuming, especially when many different source/geometry configurations must be considered (e.g. monostatic RCS calculation and optimization cycles). Therefore, an efficient and robust shadowing determination algorithm is very important. Following a direct approach, the shadowing runtime complexity will be $\mathcal{O}(N^2)$. A well-known improvement is to use a buffer which splits up the source's field of view [19, 16, 46], such that the shadowing status of a point can be determined by first identifying the buffer box it falls into, and then only testing it against the mesh elements listed as projecting into that buffer box. Implementations of this idea are either pixel-based (employing the graphics processor [36, 35]), or take the form of an algorithm which may be implemented in any suitable way [53, 54]. The algorithmic approach is not restricted in resolution and does not need a graphics processor. In [53] a uniformly divided buffer

scheme is presented, which yields $\mathcal{O}(N)$ complexity for homogeneous meshes and non-grazing incidence. A homogeneous mesh is defined as one where the individual elements' sizes are of the same order as the average element size. In [54] a scheme based on quad-tree subdivision is presented, which yields $\mathcal{O}(N \log N)$ complexity for homogeneous meshes in general.

In this thesis, a field-of-view buffer based, shadowing determination algorithm was developed. As noted above, such schemes have already been proposed, yielding linear time-scaling, however, the efficiency of those schemes deteriorate dramatically when grazing incidence takes place and when the mesh is inhomogeneous. Though one might not think so, the latter case effectively occurs very often. This is because the buffer plane is the unit sphere in case of point source illumination. Even for a homogeneous mesh, upon projecting it onto the unit sphere, the resulting representation can be severely inhomogeneous.

In [46, 51] a method is presented which ensures that efficiency is maintained in case of plane wave illumination of homogeneous meshes, at grazing incidence. This involved adding a second, fine-level buffer to effectively separate grazing-view elements into small groups, in the buffer — see the papers for further details.

In [47, 50], a generalization of the above work is presented (in [47] an overview is given and [50] gives the full details). It is an adaptive multi-level buffer scheme, which yields $\mathcal{O}(N)$ shadowing runtime complexity for all meshes under all illumination conditions (both point source and plane wave). An important feature is that grazing view and normal view elements are separated and from there on, treated as two separate objects [50]. Each object is then handled with the adaptive multi-level buffer scheme, to separate its set of elements efficiently into groups in the field-of-view plane. This scheme thus takes comprehensive care of grazing incidence. Mesh inhomogeneity is handled by way of the adaptive aspect. At any given level (which can also be the whole structure at the top level, then considered to be a single buffer box), each buffer box is considered for subdivision. It can be subdivided according to the average element size in the box, but if this leads to an excessive number of lower-level boxes, then it is rather subdivided according to the number of elements inside the box. A test for mesh inhomogeneity was developed, and boxes found to be inhomogeneous, as further subdivided. This process is continued until all boxes contain homogeneous mesh elements and not an excessive amount. For the grazing view object, a special fine-level division is done according to the procedure proposed in [51], at the leaf level of the multi-level subdivision. See [47, 50] for further details. This adaptive multi-level buffer scheme is found to yield $\mathcal{O}(N)$ shadowing runtime scaling under very extreme circumstances (extremely inhomogeneous meshes and/or extreme grazing incidence) — see the results in [47, 50]).

1.5.2 Fast MRPO

A bottleneck that is common to both MRPO and IPO, is the cost of evaluating internal reflected fields. These fields are evaluated by integrating over all visible sources. Doing this conventionally, the runtime cost scales as $\mathcal{O}(N^2)$, with N denoting the number of mesh elements (all visible basis functions contribute to the incident field at every basis function). Such integrals can be accelerated with the MLFMM or similar fast methods for evaluating integral equations at a large number of observation points. In [9, 10] the fast far field approximation (FaFFA) is used for this purpose, bringing down the field evaluation

cost to $\mathcal{O}(N^{3/2})$. In [34, 49, 1] the MLFMM is used, which brings down the cost to $\mathcal{O}(N \log N)$. This same cost scaling is achieved using the multilevel non-uniform grid algorithm, in [18]. The second bottleneck relates to internal shadowing determination. The visibility status between every pair of basis functions is required. Determining this with the efficient SRPO method from [50] by treating every basis function as a point source, yields a runtime cost-scaling of $\mathcal{O}(N^2)$ for this task. In the accelerated MRPO work of [49, 1], this bottleneck is not dealt with, since only cases are treated where all internal shadowing can be incorporated a priori (e.g. full visibility). In the accelerated IPO results of [9, 10], test cases with internal shadowing are shown, but the incorporation of (reduced) shadowing into the fast field evaluation scheme is not discussed, nor the computational complexity of the shadowing determination. In [34] it is noted that (reduced) shadowing is incorporated into the MLFMM-accelerated IPO method, via the MLFMM translation operator. However, this is done based on average element normal vectors as an indication of group orientation and moreover, no mention is made of partial visibility. Apparently the MLFMM interaction tree is left unchanged. In [18] (reduced) shadowing is incorporated into the accelerated IPO via the use of two different kernels and iterative shadowing corrections to the current. The procedure for determining the shadowing information incorporated into the two kernels is not discussed. It follows that a comprehensively accelerated MRPO formulation has not been presented to date. Even for accelerated versions of the IPO, a clear and detailed explanation of how the IPO's reduced shadowing condition is incorporated into the accelerated integrals and how it affects the time-scaling, is not available in the literature.

For this thesis, a comprehensively accelerated version of the mesh-based MRPO method, denoted FMRPO, was developed. The MLFMM is used to accelerated internal reflection field calculations in the FMRPO, as explained in [49, 48, 52]. At first, only cases where shadowing can be established a priori (i.e. full visibility) were treated, to verify the use of MLFMM for the acceleration of internal field calculation [49, 48]. The key aspect to achieving acceleration for general geometries with non-trivial internal shadowing, was to incorporate internal shadowing into the MLFMM interaction tree. This requires an alteration to the inter-group interaction criterion of the MLFMM, as well as efficient evaluation of inter-group shadowing status flags [52]. The runtime of the FMRPO was theoretically and practically shown, to scale as quasi-$\mathcal{O}(N \log N)$, depending on the specific geometry, as discussed in [52].

1.6 List of appended papers

The details of the thesis research work is documented in the seven publications which are appended. In this section, the appended publications are listed and their contents are placed into context, with regards to the original contributions of the thesis.

1.6.1 Journal papers

1. **Appendix A: Efficient shadowing determination at grazing incidence, for mesh-based physical optics scattering analysis [51]:** This paper documents the efficient shadowing determination scheme developed for grazing incidence cases under plane wave incidence.

2. **Appendix B: A comprehensive, efficient shadowing determination algorithm for mesh-based physical optics analysis [50]:** The adaptive, multi-level, buffer-based, efficient shadowing determination algorithm which is efficient for very extreme cases and which is developed for both plane wave and point source illumination, is presented in this paper.

3. **Appendix C: MLFMM-based, fast multiple-reflection physical optics for large-scale electromagnetic scattering analysis [52]:** The newly developed, fast MRPO method is fully documented and rigorously tested in this paper. This is the main result from the thesis.

1.6.2 Conference papers

1. **Appendix D: Aspects of efficient shadowing calculation for physical optics analysis of meshed objects [46]:** This paper presents an efficient shadowing determination scheme for homogeneous meshes, including plane wave grazing incidence cases. It lead to the final result presented in [51].

2. **Appendix E: Further progress with fast and reliable shadowing determination for mesh-based PO analysis [47]:** This paper gives an overview of the adaptive, multi-level, buffer-based, efficient shadowing determination algorithm from [50].

3. **Appendix F: Acceleration of multiple reflection physical optics scattering analysis with the MLFMM [49]:** This paper presents an accelerated MRPO method with respect to internal, reflected field calculation. Internal shadowing determination is not considered here. This work lead to the final scheme presented in [52].

4. **Appendix G: Acceleration of mesh-based physical optics for electromagnetic scattering analysis [48]:** This paper presents progress with the thesis work, toward the final results which are presented in [50] and [52].

1.7 Conclusion

The overall goal of this research work was to significantly accelerate the mesh-based MRPO. A standard representation was chosen for the surface current, namely RWG basis functions on a mesh of triangle elements.

Since the MRPO is an extension of the SRPO, the first part of the work focussed on the main bottleneck in the SRPO, namely incident field shadowing determination. An adaptive, multi-level, buffer-based shadowing determination algorithm was developed which was shown to be robustly optimal, yielding $\mathcal{O}(N)$ time-scaling results for extreme test cases [50]. Secondly, the main goal was pursued. The first ever, comprehensively accelerated version of the mesh-based MRPO method (which rigorously takes internal shadowing into account), denoted FMRPO, was developed. The FMRPO uses MLFMM-based acceleration for internal reflected field calculation, which required an altered inter-group interaction criterion and the efficient evaluation of inter-group shadowing status flags. In comparison to the runtime scaling of the conventional MRPO which is $\mathcal{O}(N^2)$,

the runtime of the FMRPO is theoretically and practically shown, to scale as quasi-$\mathcal{O}(N \log N)$, depending on the specific geometry. Results are presented for practical geometries with larger electrical sizes than have ever before been considered with the MRPO, but which can now for the first time be solved in realistically fast runtimes. In fact, with the FMRPO there is no fundamental limit to the electrical size of the geometries that can be solved and it is ideal for situations where many different source configurations must be considered for the same scatterer, such as mono-static radar cross section (RCS) calculations.

Given that a path to accelerated MRPO has now been established, various future developments could be considered, e.g. edge-corrections to account for diffraction effects, higher-order basis functions and parallelization.

The work presented in this thesis could be useful to developers of electromagnetic scattering analysis tools for electrically large objects.

Bibliography

[1] M. Akbaş, L. Alatan, and Ö. Ergül. Accuracy and efficiency improvements in iterative hybridization of the method of moments (MoM) and physical optics (PO). In *10th European Conference on Antennas and Propagation (EuCAP2016)*. IEEE, 2016.

[2] J. Alvarez, I. Gómez-Revuelto, J. M. Alonso, L. E. Garcia-Castillo, and M. Salazar-Palma. Fully coupled multi-hybrid finite element method–method of moments–physical optics method for scattering and radiation problems. *Electromagnetics*, 30(1-2):3–22, 2010.

[3] J. S. Asvestas. The physical optics method in electromagnetic scattering. *Journal of Mathematical Physics*, 21(2):290–299, 1980.

[4] K. E. Atkinson. *The Numerical Solution of Integral Equations of the Second Kind*. Cambridge University Press, Cambridge, UK, 1997.

[5] C. A. Balanis. *Antenna theory and design*. John Wiley and Sons, 1997.

[6] N. Bojarski. A survey of the physical optics inverse scattering identity. *IEEE Transactions on Antennas and Propagation*, 30(5):980–989, 1982.

[7] A. Bondeson, T. Rylander, and P. Ingelström. *Computational electromagnetics*, volume 51. Springer Science & Business Media, 2005.

[8] D. Bouche, F. Molinet, and R. Mittra. *Asymptotic methods in electromagnetics*. Springer Science & Business Media, 2012.

[9] R. J. Burkholder. A fast and rapidly convergent iterative physical optics algorithm for computing the RCS of open-ended cavities. *Applied Computational Electromagnetics Society Journal*, 16(1):53–60, 2001.

[10] R. J. Burkholder, C. Tokgöz, C. J. Reddy, and W. O. Coburn. Iterative physical optics for radar scattering predictions. *Applied Computational Electromagnetics Society Journal*, 24(2):241–258, 2009.

[11] M. F. Cátedra, L. Lozano, I. González, E. García, and M. Jesús Algar. Efficient techniques for accelerating the ray-tracing for computing the multiple bounce scattering of complex bodies modeled by flat facets. *Applied Computational Electromagnetics Society Journal*, 25(5):395–409, 2010.

[12] W. C. Chew, E. Michielssen, J. M. Song, and J. M. Jin. *Fast and efficient algorithms in computational electromagnetics*. Artech House, Boston, 2001.

[13] H. T. Chou and T. H. Lee. Asymptotic high frequency methods. In *Novel Technologies for Microwave and Millimeter-Wave Applications*, pages 425–460. Springer, 2004.

[14] CST. CST STUDIO SUITE 2016 User Manual, March 2016. https://www.cst.com.

[15] D. B. Davidson. *Computational electromagnetics for RF and microwave engineering*. Cambridge University Press, 2005.

[16] S. F. de Adana, O. Gutiérrez, I. González, M. F. Cátedra, and L. Lozano. *Practical Applications of Asymptotic Techniques in Electromagnetics*. Artech House, Boston, 2011.

[17] M. Domingo, F. Rivas, J. Pérez, R. P. Torres, and M. F. Cátedra. Computation of the RCS of complex bodies modeled using NURBS surfaces. *IEEE Antennas and Propagation Magazine*, 37(6):36–47, 1995.

[18] I. Gershenzon, A. Boag, and Y. Brick. Fast iterative physical optics with shadowing. In *2016 IEEE International Symposium on Antennas and Propagation and USNC-URSI Radio Science meeting (APSURSI2016)*, volume 3, pages 1363–1364. IEEE, 2016.

[19] E. A. Haines and D. P. Greenberg. The light buffer: A shadow-testing accelerator. *IEEE Computer Graphics and Applications*, pages 6–16, September 1986.

[20] Altair Hyperworks. FEKO 14.0 User Manual, June 2016. http://www.feko.info.

[21] U. Jakobus and F. M. Landstorfer. Improved PO-MM hybrid formulation for scattering from three-dimensional perfectly conducting bodies of arbitrary shape. *IEEE Transactions on Antennas and Propagation*, 43(2):162–169, 1995.

[22] J. M. Jin. *Theory and Computation of Electromagnetic Fields*. John Wiley & Sons, New York, 2010.

[23] J. B. Keller. Geometrical theory of diffraction. *Journal of the Optical Society of America*, 52(2):116–130, 1962.

[24] R. G. Kouyoumjian and P. H. Pathak. A uniform geometrical theory of diffraction for an edge in a perfectly conducting surface. *Proceedings of the IEEE*, 62(11):1448–1461, 1974.

[25] H. Ling, R. C. Chou, and S. W. Lee. Shooting and bouncing rays: Calculating the RCS of an arbitrarily shaped cavity. *IEEE Transactions on Antennas and Propagation*, 37(2):194–205, 1989.

[26] K. M. Mitzner. Incremental length diffraction coefficients. Technical report, DTIC Document, 1974.

[27] F. Obelleiro-Basteiro, R. J. Luis, and R. J. Burkholder. An iterative physical optics approach for analyzing the electromagnetic scattering by large open-ended cavities. *IEEE Transactions on Antennas and Propagation*, 43(4):356–361, 1995.

[28] L. Pandolfo, P. de Vita, M. Bandinelli, G. Carluccio, and M. Albani. GPU acceleration of an iterative physical optics algorithm for the analysis of electrically large scatterers. In *9th European Conference on Antennas and Propagation (EuCAP)*, pages 1–5. IEEE, 2015.

[29] J. Pérez and M. F. Cátedra. Application of physical optics to the RCS computation of bodies modeled with nurbs surfaces. *IEEE Transactions on Antennas and Propagation*, 42(10):1404–1411, 1994.

[30] A. F. Peterson, S. L. Ray, and R. Mittra. *Computational methods for electromagnetics*. Oxford University Press and IEEE Press, Oxford & New York, 1998.

[31] G. A. Rao and S. P. Mahulikar. Integrated review of stealth technology and its role in airpower. *Aeronautical Journal*, 106(1066):629–641, 2002.

[32] S. M. Rao, D. Wilton, and A. Glisson. Electromagnetic scattering by surfaces of arbitrary shape. *IEEE Transactions on Antennas and Propagation*, 30(3):409–418, 1982.

[33] E. Rashidi-Ranjbar and M. Dehmollaian. Scattering of an object with impedance surfaces using IPO and MLFMM. In *22nd Iranian Conference on Electrical Engineering (ICEE2014)*, pages 1610–1613. IEEE, 2014.

[34] E. Rashidi-Ranjbar and M. Dehmollaian. Target above random rough surface scattering using a parallelized IPO accelerated by MLFMM. *IEEE Geoscience and Remote Sensing Letters*, 12(7):1481–1485, 2015.

[35] J. M. Rius, A. Carbo, J. Bjerkemo, E. Ubeda, A. Heldring, J. J. Mallorquí, and A. Broquetas. New graphical processing technique for fast shadowing computation in PO surface integral. *IEEE Transactions on Antennas and Propagation*, 62(5):2587–2595, February 2014.

[36] J. M. Rius, M. Ferrando, and L. Jofre. GRECO: Graphical electromagnetic computing for RCS prediction in real time. *IEEE Antennas and Propagation Magazine*, 35(2):7–17, 1993.

[37] T. K. Sarkar, Z. Ji, K. Kim, A. Medouri, and M. Salazar-Palma. A survey of various propagation models for mobile communication. *IEEE Antennas and propagation Magazine*, 45(3):51–82, 2003.

[38] T. Shijo, L. Rodriguez, and M. Ando. The modified surface-normal vectors in the physical optics. *IEEE Transactions on Antennas and Propagation*, 56(12):3714–3722, 2008.

[39] W. L. Stutzman and G. A. Thiele. *Antenna Theory and Design*. John Wiley & Sons, New York, 2nd edition, 1998.

[40] S. Suk, T. I. Seo, H. S. Park, and H. T. Kim. Multiresolution grid algorithm in the SBR and its application to the RCS calculation. *Microwave and Optical Technology Letters*, 29(6):394–397, 2001.

[41] Y. B. Tao, H. Lin, and H. J. Bao. KD-tree based fast ray tracing for RCS prediction. *Progress In Electromagnetics Research*, 81:329–341, 2008.

[42] A. Thomet, G. Kubické, C. Bourlier, and P. Pouliguen. Improvement of iterative physical optics using the physical optics shadow radiation. *Progress In Electromagnetics Research M*, 38:1–13, 2014.

[43] P. Y. Ufimtsev. Method of edge waves in the physical theory of diffraction. Technical report, DTIC Document, 1971.

[44] P. Y. Ufimtsev. Improved physical theory of diffraction: Removal of the grazing singularity. *IEEE Transactions on Antennas and Propagation*, 54(10):2698–2702, 2006.

[45] F. Weinmann. Ray tracing with PO/PTD for RCS modeling of large complex objects. *IEEE Transactions on Antennas and Propagation*, 54(6):1797–1806, 2006.

[46] D. P. Xiang and M. M. Botha. Aspects of efficient shadowing calculation for physical optics analysis of meshed objects. In *16th International Conference on Electromagnetics in Advanced Applications (ICEAA2014)*, pages 492–495. IEEE, 2014.

[47] D. P. Xiang and M. M. Botha. Further progress with fast and reliable shadowing determination for mesh-based PO analysis. In *17th International Conference on Electromagnetics in Advanced Applications (ICEAA2015)*, pages 958–961. IEEE, 2015.

[48] D. P. Xiang and M. M. Botha. Acceleration of mesh-based physical optics for electromagnetic scattering analysis. In *7th European Community on Computational Methods in Applied Sciences (ECCOMAS2016)*, 2016.

[49] D. P. Xiang and M. M. Botha. Acceleration of multiple reflection physical optics scattering analysis with the MLFMM. In *10th European Conference on Antennas and Propagation (EuCAP2016)*. IEEE, 2016.

[50] D. P. Xiang and M. M. Botha. A comprehensive, efficient shadowing determination algorithm for mesh-based physical optics analysis. In preparation.

[51] D. P. Xiang and M. M. Botha. Efficient shadowing determination at grazing incidence, for mesh-based physical optics scattering analysis. Submitted for publication.

[52] D. P. Xiang and M. M. Botha. MLFMM-based, fast multiple-reflection physical optics for large-scale electromagnetic scattering analysis. Submitted for publication.

[53] F. T. Zha, S. X. Gong, Y. X. Xu, Y. Guan, and W. Jiang. Fast shadowing technique for electrically large targets using z-buffer. *Journal of Electromagnetic Waves and Applications*, 23(2-3):341–349, 2009.

[54] Y. H. Zhao. Fast physical optics calculation for SAR imaging of complex scatterers. Master's thesis, Ohio State University, 2012.

Appendix A

Journal paper — fast shadowing [51]

D. P. Xiang and M. M. Botha, **"Efficient shadowing determination at grazing incidence, for mesh-based physical optics scattering analysis,"** August 2016, submitted for publication.

Efficient shadowing determination at grazing incidence, for mesh-based physical optics scattering analysis

Dao P. Xiang[a], Matthys M. Botha[a,*]

[a]*Department of Electrical and Electronic Engineering, Stellenbosch University, Private Bag X1, Matieland 7602, Stellenbosch, South Africa*

Abstract

Shadowing determination is a crucial step in methods based on the physical optics (PO) approximation, which are widely used for electromagnetic scattering analysis of electrically large, conducting bodies. When the surface current is represented by basis functions on a mesh of triangle elements, this involves determining for each mesh edge and/or elemental face whether it is visible to the source or obscured by another mesh element. A field-of-view buffer-based shadowing determination algorithm for plane wave illumination of homogeneous triangle-element meshes is presented, with special provision to maintain efficiency in case of grazing incidence. For homogeneous meshes the computational costs in runtime and memory are both directly proportional to the number of mesh elements.

1. Introduction

Methods based on the physical optics (PO) approximation are widely used for electromagnetic scattering analysis of electrically large, perfect electrically conducting (PEC) bodies [1, 2]. Shadowing determination is a crucial part of any PO-based analysis scheme, i.e. to determine which parts of an object are visible to the source. The focus here is on mesh-based PO analysis, where the surface current is represented with standard Method of Moments (MoM) basis functions on a triangle element mesh, cf. [2, 3, 4]. The visibility of edge midpoints must be determined when using edge-associated RWG basis functions [2] (i.e. checking the status of $\approx 1.5N$ points, with N denoting the number of mesh elements); for higher-order, face-associated basis functions, visibility of element centroids must also be determined (an additional N point checks). A point is shadowed when it is obscured by a mesh element, as viewed along the incident wave direction.

Following a direct approach, the shadowing runtime complexity will be $O(N^2)$. A well-known improvement is to use a buffer which splits up the source's field of view [5, 6, 7]. Implementations of this idea are either pixel-based (employing the graphics processor [8]), or take the form of an algorithm which may be implemented in any suitable way [3, 4]. The algorithmic approach is not restricted in resolution and does not need a graphics processor. Efficiency derives from separating the elements into smaller groups, such that a point's shadowing status can be determined by only considering a small subset of mesh elements. In [3] a uniformly divided buffer scheme is presented, which yields $O(N)$ complexity for homogeneous meshes and non-grazing incidence. A

*Corresponding author
Email address: mmbotha@sun.ac.za (Matthys M. Botha)

homogeneous mesh is defined as one where the individual elements' sizes are of the same order as the average element size. In [4] a scheme based on quad-tree subdivision is presented, which yields $\mathcal{O}(N \log N)$ complexity for homogeneous meshes in general.

Clearly, shadowing determination can be time consuming for large meshes, especially when many different source/geometry configurations must be considered (e.g. monostatic RCS calculation and optimization cycles). This letter presents a buffer-based shadowing determination algorithm with efficient grazing incidence treatment, for plane wave illumination of arbitrary geometries represented with homogeneous triangle meshes.

2. Buffer-based shadowing algorithm

Consider a PEC object represented by a homogeneous mesh of flat triangle elements. It is illuminated by a plane wave with angles of incidence $(\theta_{\text{inc}}, \phi_{\text{inc}})$ and direction of incidence $\hat{\eta} = -\sin\theta_{\text{inc}}\cos\phi_{\text{inc}}\hat{x} - \sin\theta_{\text{inc}}\sin\phi_{\text{inc}}\hat{y} - \cos\theta_{\text{inc}}\hat{z}$.

The algorithm starts by establishing a 2D, Cartesian coordinate system (a, b), in an orthogonal plane to $\hat{\eta}$ (i.e. an eikonal surface of the incident plane wave). This is the buffer plane. The orthogonal base vectors in this coordinate system are defined as $\hat{a} = \sin\phi_{\text{inc}}\hat{x} - \cos\phi_{\text{inc}}\hat{y}$ and $\hat{b} = -\cos\theta_{\text{inc}}\cos\phi_{\text{inc}}\hat{x} - \cos\theta_{\text{inc}}\sin\phi_{\text{inc}}\hat{y} + \sin\theta_{\text{inc}}\hat{z}$, with $\hat{a}\times\hat{b} = \hat{\eta}$. Project all triangles into the buffer plane and record their individual bounding boxes $(L_n^a \times L_n^b)$ and that of the whole projected mesh $(L_{\text{mesh}}^a \times L_{\text{mesh}}^b)$. Each triangle's depth information as well as orientation w.r.t. $\hat{\eta}$ are also calculated as $d_n = \vec{r}_n^{\,\text{min}} \cdot \hat{\eta}$ and $\cos\alpha_n = |\hat{n}_n \cdot \hat{\eta}|$, respectively; where $\vec{r}_n^{\,\text{min}}$ denotes the position vector to the vertex of the n-th triangle which yields the smallest depth; $\hat{n}_n$ denotes the unit normal vector to the n-th triangle. At this stage, triangles viewed edge-on, with $0 \leqslant \cos\alpha_n < \epsilon_{\text{edge}}$ are discarded from any further consideration for shadowing determination, as they are regarded as invisible. Points internal to or shared between such triangles are automatically regarded as shadowed. In the case of a double-precision implementation set the tolerance value to $\epsilon_{\text{edge}} = 10^{-12}$. Further calculate the average projected element bounding box size as $\ell_{\text{ave}} = \dfrac{\sum_{n=1}^{N} \max\left(L_n^a, L_n^b\right)}{N}$. The max-based measure is used to ensure that ℓ_{ave} is effectively independent of elemental orientations. Subdivide the buffer bounding box into a set of identical buffer boxes and for each buffer box create a list of all triangles of which any part of their individual bounding boxes projects into it. The numbers of subdivisions in the two directions are obtained as $N^a = \left\lceil \dfrac{L_{\text{mesh}}^a}{\ell_{\text{ave}}} \right\rceil$ and $N^b = \left\lceil \dfrac{L_{\text{mesh}}^b}{\ell_{\text{ave}}} \right\rceil$, where $\lceil\cdot\rceil$ refers to the ceiling function. Figure 1 illustrates these step.

If the incident wave is at grazing incidence to a large smooth surface of the geometry, then many triangles will project into single buffer boxes and equal separation of triangles in the field of view will not be achieved. Solve this by subdividing grazing view buffer boxes (boxes containing more grazing view triangles than standard ones) into fine-level buffer boxes with their own box lists. Grazing view triangles are identified using a threshold angle condition $90^\circ - \alpha_{\text{GV}} < \alpha_n \leqslant 90^\circ$. The idea is illustrated in Figure 2. The average normal vector of all grazing view triangles in the box is determined as $\hat{n}_{\text{GV}}$. This vector is projected onto the buffer plane and the resulting direction is denoted by $\hat{v}$, with orthogonal counterpart $\hat{u}$. In this local coordinate system a local buffer is defined with box dimension in the u-direction set to ℓ_{ave} and in the v-direction to the average v-dimension of the grazing view triangles' bounding boxes, yielding a set of 'flat' fine-level boxes. Grazing view triangles are listed in the fine-level box lists

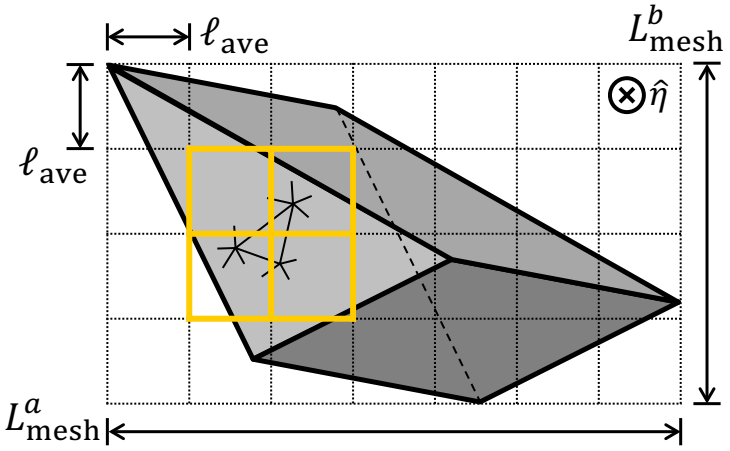

Figure 1: Example buffer bounding box and buffer boxes for a general object. A specific mesh triangle is shown, with highlighting of the four buffer boxes where it will be listed.

similarly as for the standard buffer. To each fine-level buffer box list, add all of the non-grazing view triangles listed in the corresponding standard buffer box and remove the grazing view triangles from the standard buffer box list. For a smooth curved surface at grazing incidence, many such fine level buffer box sets will be set up, each with its own orientation. As shown in the results section, set $\alpha_{GV} = 5^\circ$ for best performance.

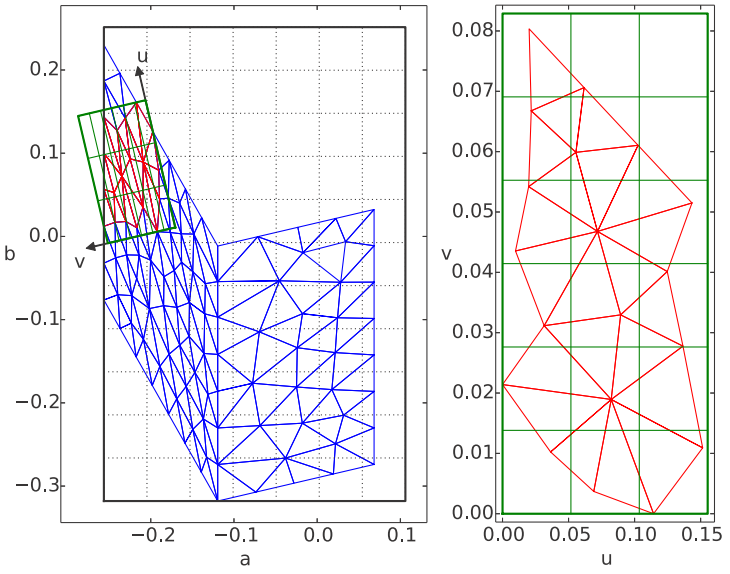

Figure 2: Example mesh visualization showing all the normal buffer boxes, as well as the fine-level buffer boxes for a specific grazing view box. An enlarged view of the fine-level buffer boxes shows that proper separation of the grazing view triangles is achieved.

The final step in preparing the buffer, is to sort every buffer box list according to the depth of its elements. With the buffer ready, each point for shadowing status checking is projected into the buffer plane and the box it belongs to is identified (standard or fine-level, whichever the case may be). Check the point for shadowing only against those triangles in the box list, with smaller depth than the point itself (no unnecessary checking of triangles behind the point). These triangles are checked in order of depth (closest first). This algorithm is guaranteed to be error-free.

The computational cost of setting up the buffer and storing it is $O(N)$, because the number of boxes and number of elements processed are both $O(N)$ (only non-empty

buffer boxes are stored). The cost of a single point check is $O(1)$, since the number of elements listed in any buffer box is independent of N, for a homogeneous mesh. The cost of performing $O(N)$ shadowing point checks is thus $O(N)$; therefore, the algorithm can be expected to yield optimal time scaling for all incident directions.

3. Numerical results

Figure 3 shows two test objects. To investigate the choice of the grazing view threshold angle α_{GV}, the faceted model is considered. Shadowing determination is done for incident angles in the range $\theta_{\mathrm{inc}} \in [0, 360^\circ]$, with $\phi_{\mathrm{inc}} = 180^\circ$. Figure 4 shows the shadowing runtime as a function of θ_{inc}, for fixed values of α_{GV}. With $\alpha_{\mathrm{GV}} = 0^\circ$ there is no grazing incidence treatment and sharp peaks in runtime is observed as $\hat{\eta}$ becomes close to tangential to various facets in the model. For $\alpha_{\mathrm{GV}} = 90^\circ$ the whole model is always handled with the grazing incidence treatment. No peaks are present, but the runtime is long. Both the $\alpha_{\mathrm{GV}} = 5^\circ$ and $\alpha_{\mathrm{GV}} = 15^\circ$ results eliminate the sharp peaks, while eliminating slow runtimes for non-grazing incidence. The optimal choice is found to be $\alpha_{\mathrm{GV}} = 5^\circ$, as also affirmed by other results not shown.

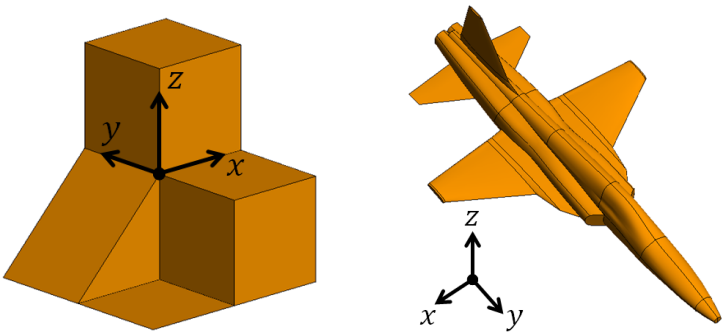

Figure 3: Test objects. Left: flat, faceted model. Right: aircraft model.

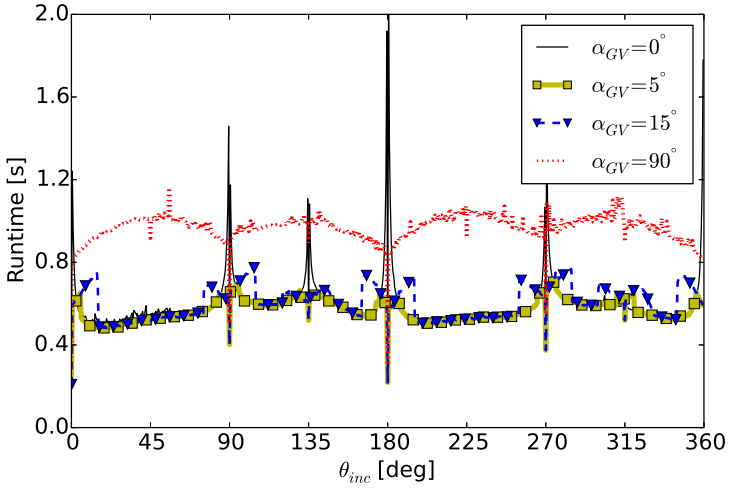

Figure 4: Investigation of the effect of grazing view threshold angle α_{GV} on runtime, with $\theta_{\mathrm{inc}} \in [0, 360^\circ]$ and $\phi_{\mathrm{inc}} = 180^\circ$ for the faceted model meshed homogeneously with 540,996 triangles.

Now investigate the performance of the proposed algorithm. Three directions of grazing incidence is chosen for each model (incidences at 89° for the faceted model and for the aircraft model $\hat{\eta} \in \{-\hat{x}, -\hat{y}, -\hat{z}\}$). The uniform mesh size is varied to obtain

runtime as a function of N in Figure 5. The results are compared with the mesh-based PO solver in FEKO [9] and the shadowing determination algorithm from [3]. All results are for edge midpoint shadowing testing, i.e. $\approx 1.5N$ shadowing checks. The proposed algorithm consistently yields $\mathcal{O}(N)$ time scaling while the others do not. The proposed algorithm is practically unaffected by different directions of incidence and geometry. To underscore the importance of the special grazing incidence treatment, results with this feature turned off are included, exhibiting higher-order complexity.

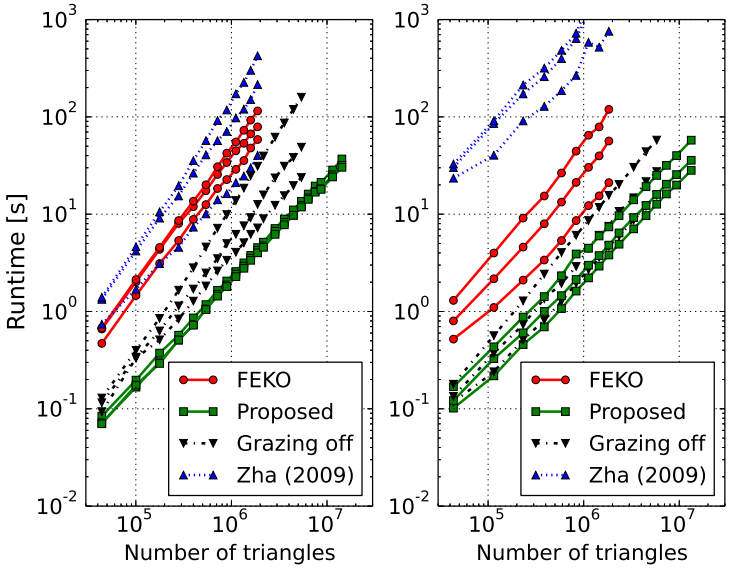

Figure 5: Shadowing determination runtime vs. number of mesh elements, with significant grazing incidence. The abscissa range is $[3 \times 10^4, 3 \times 10^7]$. Left: faceted model. Right: aircraft model.

4. Conclusion

A field-of-view buffer-based, physical optics shadowing determination algorithm with special treatment for grazing-view elements, was presented for plane wave illumination of triangle meshes. For arbitrary homogeneous meshes, both the runtime and memory exhibit $\mathcal{O}(N)$ computational complexity. This predicted, linear time-scaling was practically demonstrated for meshes over a very large range of sizes (up to almost twenty million elements). It is the first time that such results are presented in the literature, to the authors' knowledge. The scheme out-performs a commercial PO solver as well as the most competitive shadowing determination algorithm from the literature to date.

Acknowledgment

This work was funded by Altair Development S.A. (Pty) Ltd.

References

[1] N. Bojarski, "A survey of the physical optics inverse scattering identity," *IEEE Trans. Antennas Propag.*, vol. 30, no. 5, pp. 980–989, 1982.

[2] U. Jakobus and F. M. Landstorfer, "Improved PO-MM hybrid formulation for scattering from three-dimensional perfectly conducting bodies of arbitrary shape," *IEEE Trans. Antennas Propag.*, vol. 43, no. 2, pp. 162–169, 1995.

[3] F.-T. Zha, S.-X. Gong, Y.-X. Xu, Y. Guan, and W. Jiang, "Fast shadowing technique for electrically large targets using z-buffer," *Journal of Electromagnetic Waves and Applications*, vol. 23, no. 2-3, pp. 341–349, 2009.

[4] Y. Zhao, "Fast physical optics calculation for SAR imaging of complex scatterers," Master's thesis, Ohio State University, 2012.

[5] E. A. Haines and D. P. Greenberg, "The light buffer: A shadow-testing accelerator," *IEEE Computer Graphics and Applications*, pp. 6–16, September 1986.

[6] F. Saez de Adana, O. Gutiérrez, I. González, M. F. Cátedra, and L. Lozano, *Practical Applications of Asymptotic Techniques in Electromagnetics*. Boston: Artech House, 2011.

[7] D. P. Xiang and M. M. Botha, "Aspects of efficient shadowing calculation for physical optics analysis of meshed objects," in *2014 International Conference on Electromagnetics in Advanced Applications (ICEAA2014)*. IEEE, 2014, pp. 492–495.

[8] J. M. Rius, A. Carbo, J. Bjerkemo, E. Ubeda, A. Heldring, J. J. Mallorquí, and A. Broquetas, "New graphical processing technique for fast shadowing computation in PO surface integral," *IEEE Trans. Antennas Propag.*, vol. 62, no. 5, pp. 2587–2595, February 2014.

[9] Altair Engineering Inc, "FEKO User's Manual Suite 7.0," August 2014, http://www.feko.info.

Appendix B

Journal paper — fast shadowing [50]

D. P. Xiang and M. M. Botha, "**A comprehensive, efficient shadowing determination algorithm for mesh-based physical optics analysis,**" in preparation.

A comprehensive, efficient shadowing determination algorithm for mesh-based physical optics analysis

Dao P. Xiang[a], Matthys M. Botha[a,*]

[a]*Department of Electrical and Electronic Engineering, Stellenbosch University, Private Bag X1, Matieland 7602, Stellenbosch, South Africa*

Abstract

This paper presents a field-of-view, buffer-based shadowing determination algorithm for determining the illumination status of basis functions in the mesh-based, single-reflection physical optics (PO) method. The algorithm is tailored to triangle element meshes. The method makes provision for either plane wave or point source illumination. It is based on an adaptive, recursive, multi-level subdivision scheme of the projected mesh in the field-of-view, buffer plane. The method is completely general, making specific provision for handling inhomogeneous meshes and grazing incidence cases well. A direct approach to shadowing determination will yield O(N^2) runtime cost scaling (where N denotes the number of mesh elements). The algorithm proposed here, yields O(N) time scaling. It is exceedingly robust, as demonstrated by the numerical results. No competing scheme is available in the literature, to the best of the authors' knowledge.

1. Introduction

The physical optics (PO) approximation is widely used for electromagnetic scattering analysis of electrically large, conducting bodies [1, 2]. Shadowing determination forms a crucial part of any PO-based analysis scheme [3, 4]. With PO, the geometry can be either represented directly by a CAD model, or by a mesh of (e.g. triangle) elements. This paper is focussed on the latter. Many publications on mesh-based PO analysis schemes can be found in the engineering electromagnetics literature, e.g. [5, 6, 7]. However, the practical aspects of efficient shadowing determination for mesh-based PO analysis has rarely been considered in depth. Shadowing determination can be time consuming for electrically large, meshed objects; especially when many different source configurations must be considered (e.g. monostatic RCS calculations, optimization cycles).

In this paper, an optimally efficient and exceedingly robust shadowing determination method is presented for plane wave and point source illumination of arbitrary triangle element, meshed objects. The method is based on the well-knowns field-of-view buffer concept [8, 9, 10, 11].

This paper is organized as follows. Section 2 presents an overview of the algorithm. Section 3 presents details on specific aspects of the algorithm. Section 4 presents numerical results. The conclusion follows in Section 5.

*Corresponding author

Email address: mmbotha@sun.ac.za (Matthys M. Botha)

2. Flowchart describing the multi-level, recursive buffer-based shadowing algorithm

Figure 1 shows a flowchart describing the algorithm. In this section, the overall shadowing algorithm is described according to the details in the flowchart. Subsequent sections in the paper describe some of the steps in further details. The algorithm is based on the field-of-view buffer concept, where the source's field of view is split up into boxes [8, 10, 11], such that the shadowing status of a point can be determined by first identifying the buffer box it falls into, and then only testing it against the mesh elements listed as also projecting into that buffer box. In other words, the buffer boxes serve to separate the elements into smaller groups in the field of view.

Consider an object represented by a mesh of planar triangles, with total number N. For plane wave illumination the incident direction must be specified and for point source illumination, the position of the point source. The objective is determine the shadowing status of a set of "control points" which are typically mesh edge midpoints and/or element centroids. The key part for the buffer-based approach is the construction of the buffer boxes. The procedure of the proposed method is as follows (with reference to Figure 1):

1) Pre-processing: Load the mesh file, then extract the nodes and triangle elements information from the mesh file; test all triangles' orientation with respect to the source view direction and identify the normal view part (the set of all triangles not at grazing view, as defined in [12]) and the grazing view part (the set of all triangles at grazing view, as defined in [12]). The recursive buffer construction and the shadowing testing is done completely separately for the normal view part and the grazing view part (i.e. these are effectively treated as separate objects, each with its own buffer). Figure 2 shows an example of a mesh separated into its normal view and grazing view parts.

2) Multi-level recursive buffer construction: For the normal view part, we have the *normal view buffer*; for the grazing view part, we have the *grazing view buffer*. At the final level flat buffer boxes are constructed for the grazing view part, but otherwise the procedure of the buffer construction for the normal view part and the grazing view part is the same. For each buffer box at a given level, check if it contains an inhomogeneous mesh or not. If it contains an inhomogeneous mesh, then treat the mesh in the buffer box as a new object and construct a new buffer for it. Repeat this procedure until there is no buffer box that contains an inhomogeneous mesh. For the normal view part, the buffer construction is then finished. For the grazing view part, there can still be large numbers of triangles that fall into the same buffer box at grazing incidence. Therefore, after inhomogeneous mesh checking and recursive buffer construction, for each buffer box of the grazing view part, a new fine flat buffer must be included to treat grazing incidence (see [12] for the flat buffer box construction to treat grazing incidence in a given buffer box). Some further details on these steps are as follows:

2.1) Choose the buffer plane: For plane wave illumination, choose the plane perpendicular to the incident direction as the buffer plane; for point source illumination, choose the unit sphere centred around the point source. For the normal view part and the grazing view part, the buffer planes are defined the same.

2.2) Project all triangles into the buffer plane: For the normal view part and the grazing view part, project each into its own buffer plane. The details of these projections are discussed later.

2.3) Find the bounding boxes: After the projection, keep track of the extreme values in both buffers.

2.4) Construct first level normal view buffer boxes and grazing view buffer boxes: The first level buffer construction method is the same for the normal view part and the grazing view part. At first use a buffer construction method which we call the **average size buffer**, using the average triangle's bounding box size as the buffer box size, to subdivide the bounding boxes into square buffer boxes of this dimension. If the number of non-empty buffer boxes is larger than the number of mesh elements, then we use another kind of buffer construction method which we call the **N buffer**. The construction of the average size buffer and N buffer will be explained further in Section 3.3.

2.5) Multi-level recursive buffer construction: Assume that the first level buffer boxes have been constructed. For the normal view part, only check if the mesh in each buffer box is inhomogeneous or not. If it is inhomogeneous, then treat the mesh elements which project into that buffer box, as a new object and build the new buffer for it. Afterwards, the recursive buffer construction for the normal view part is finished.

For the grazing view part, after the first-level buffer boxes have been defined, then for each buffer box, do inhomogeneous mesh checking. If a box is inhomogeneous then treat the elements projecting into it as a new object and build a new level buffer like the normal view case. At the leaf-level of this process (when inhomogeneity has been resolved), then if the number of elements projecting into a buffer box is large, test the elements for relative flatness (test for the extent to which they lie in a flat plane). After the relative flatness test, if the mesh in the buffer box is relatively flat, then build a new fine flat buffer box set with all elements in that buffer box, according to the procedure in [12]. If the mesh in the buffer box is not a relatively flat surface, firstly construct a 3×3 ("9-Buffer") subdivision in that buffer box (to resolve parts that lie in different planes, e.g. grazing incidence along the edge of a wedge). Then for each sub buffer box, construct a new fine flat buffer box set with all elements in that sub buffer box, according to the procedure in [12]. The multi-level, recursive buffer construction for the grazing view part is then finished.

3) Control points definition: The choice of control points is dependent on the specific shadowing rule or definition followed. For example, the shadow rule could be if the centroid of the mesh triangle is visible, then the whole triangle is visible; or if the midpoint of the RWG basis function's associated edge is visible, then the RWG is visible. For the results presented here, we choose the edge midpoints for shadowing status checking.

4) Shadowing judgement: For each control point in the control points set, project it into the normal view buffer and identify the buffer box to which it belongs. Check the point for shadowing against a subset of the triangles in that buffer box's list.

If the point is shadowed, then set the shadow flag for it to shadowed; if the point is not shadowed, then project it into the grazing view buffer and identify the buffer box to which it belongs. Check the point for shadowing against a subset of the triangles in that buffer box's list. If the point is shadowed in the grazing view buffer, then set the shadow flag for it to shadowed, otherwise, the control point is visible. The subset is defined as all triangles of which the depth is such that they could possibly shadow the point (i.e. time is not wasted on checking triangles that lie sufficiently further away from the source than the point under consideration).

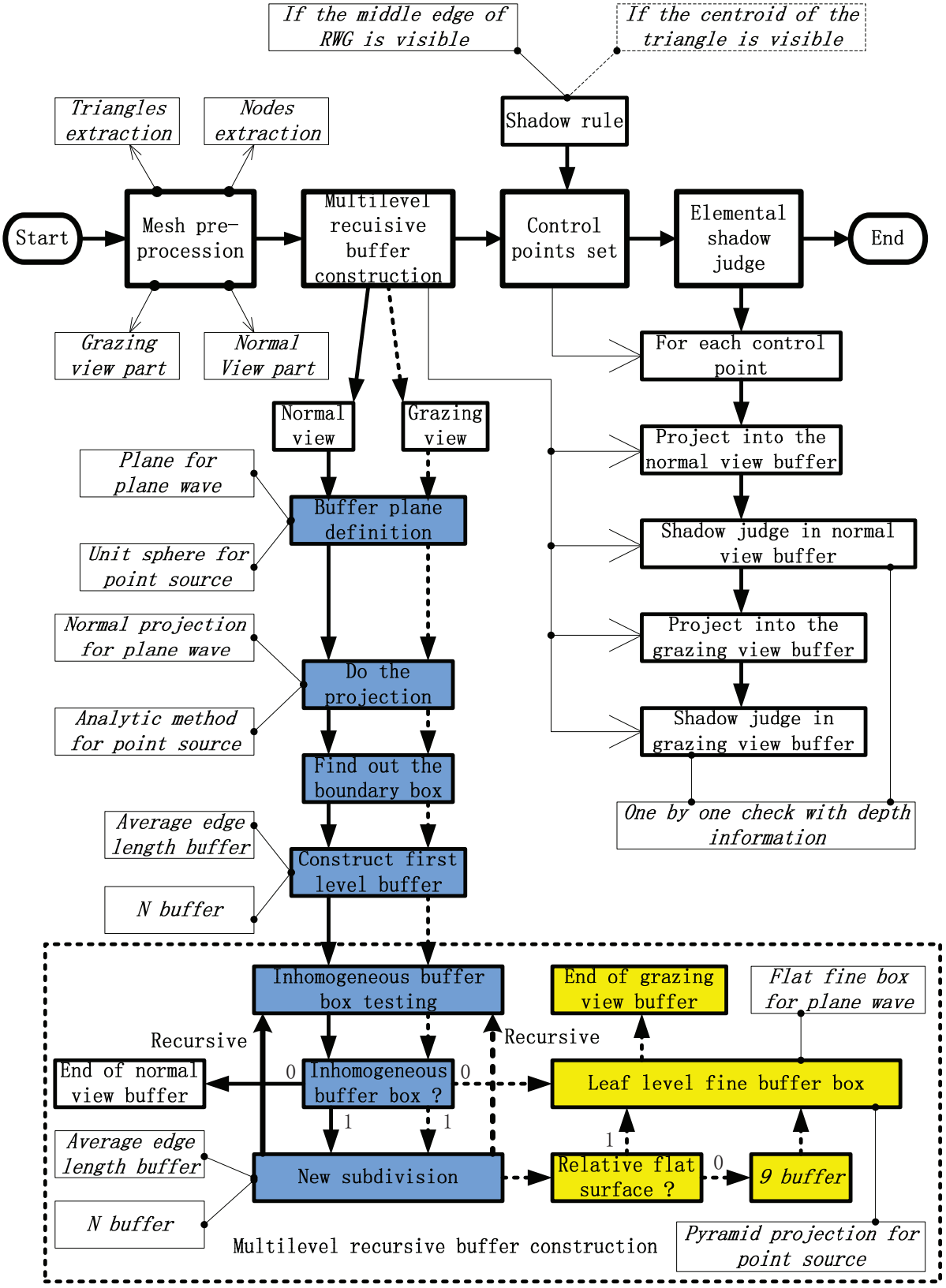

Figure 1: Flowchart describing the adaptive, multi-level, buffer-based shadowing algorithm. The blue boxes indicate that the procedure is the same for the normal view and grazing view parts. The yellow boxes indicate that the procedure is only applicable for the grazing view part.

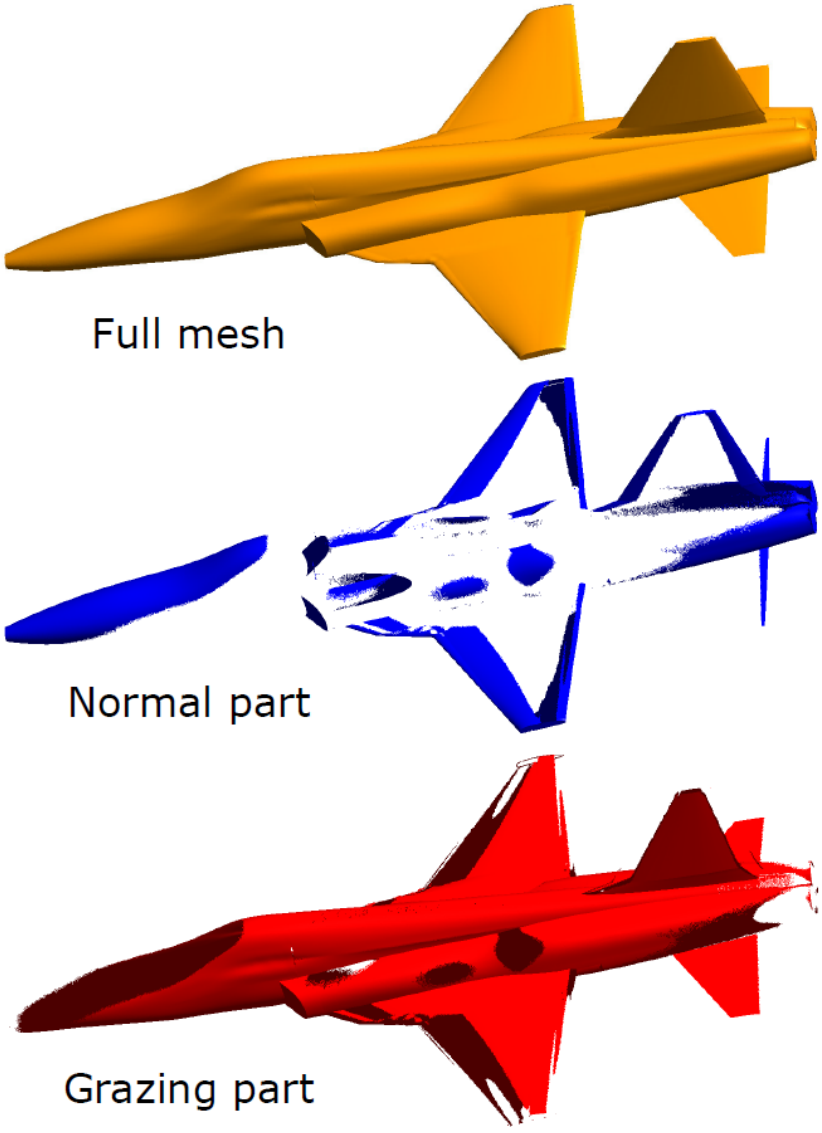

Figure 2: Example of a mesh representing an aircraft, which is divided into its normal view and grazing view parts, given head-on plane wave illumination.

3. Detail aspects of the multi-level, recursive buffer-based shadowing algorithm

3.1. Buffer plane definition

3.1.1. Plane wave illumination

If the object is illuminated by a plane wave with angles of incidence $(\theta_{\text{inc}}, \phi_{\text{inc}})$ and direction of incidence

$$\hat{\eta} = -\sin\theta_{\text{inc}}\cos\phi_{\text{inc}}\hat{x} - \sin\theta_{\text{inc}}\sin\phi_{\text{inc}}\hat{y} - \cos\theta_{\text{inc}}\hat{z} \tag{1}$$

then choose the plane which is perpendicular to $\hat{\eta}$ and which contains the origin of the mesh coordinate system $[(x, y, z) = (0, 0, 0)]$ as the buffer plane. The base vectors defining the (a, b) coordinate system on this plane are then defined as

$$\hat{a} = \sin\phi_{\text{inc}}\hat{x} - \cos\phi_{\text{inc}}\hat{y} \tag{2}$$

$$\hat{b} = -\cos\theta_{\text{inc}}\cos\phi_{\text{inc}}\hat{x} - \cos\theta_{\text{inc}}\sin\phi_{\text{inc}}\hat{y} + \sin\theta_{\text{inc}}\hat{z} \tag{3}$$

with $\hat{\eta}$, $\hat{a}$ and $\hat{b}$ orthogonal to each other $(\hat{a} \times \hat{b} = \hat{\eta})$.

3.1.2. Point source illumination

If the object is illuminated by a point source, i.e. a Hertzian dipole, then let the mesh be defined in a global Cartesian coordinate system (x, y, z) with origin at the location of the point source. Denote the coordinates of the spherical coordinate system with the same origin by (r, θ, ϕ), with the standard correspondence to the Cartesian coordinate values. The azimuth angle is calculated as

$$\phi = \mathrm{ArcTan}(x, y) \qquad \phi \in [0, 2\pi]. \tag{4}$$

The function 'ArcTan(x, y)' is the extended version of the standard 'arctan(y/x)' function, such that the result corresponds to the actual quadrant where (x, y) is located.

The buffer plane is defined in this spherical coordinate system as the unit sphere surface ($r = 1$). The buffer will thus be defined in this (θ, ϕ)-plane, which is orthogonal to the direction of incidence (as before). In this case the unit vector describing the direction of incidence is a function of position, as follows:

$$\hat{\zeta} = \sin\theta\cos\phi\hat{x} + \sin\theta\sin\phi\hat{y} + \cos\theta\hat{z}. \tag{5}$$

3.2. Determination of bounding boxes in the buffer planes

Project the normal (grazing) view part into the normal (grazing) view buffer and keep track of the extreme values in the normal (grazing) view buffer. This yields the normal (grazing) view part's bounding box. Also record various details of the mesh during this step.

3.2.1. Plane wave illumination

Loop over all normal (grazing) view part triangles and record their individual bounding boxes in the normal (grazing) buffer plane. Each triangle's depth information as well as orientation w.r.t. $\hat{\eta}$ are also calculated as follows:

$$d_n = \min(\vec{r}_i \cdot \hat{\eta}) \ \text{ where } i = 1, 2, 3 \qquad \{\text{depth}\} \tag{6}$$

$$\cos\alpha_n = \hat{n}_n \cdot \hat{\eta} \qquad \{\text{orientation}\} \tag{7}$$

where $\hat{n}_n$ denotes the unit normal vector to the n-th triangle and $\vec{r}_i$, $i = 1, 2, 3$ is the triangle's vertex position vectors. Also calculate the average projected element bounding box size ℓ_{ave}, as

$$\ell_{\text{ave}} = \frac{\sum_{n=1}^{N} \max\left(L_n^a, L_n^b\right)}{N} \tag{8}$$

where $L_n^a \times L_n^b$ is the bounding box of the n-th element after projection onto the normal (grazing) buffer plane.

Finally, the bounding box of the projection of the whole mesh in the normal (grazing) buffer plane is obtained from the elemental data as

$$a_{\min} \leqslant a \leqslant a_{\min} + L^a_{\text{mesh}} \tag{9}$$

$$b_{\min} \leqslant b \leqslant b_{\min} + L^b_{\text{mesh}} \tag{10}$$

with the dimensions of the bounding box thus being $L^a_{\text{mesh}} \times L^b_{\text{mesh}}$

The computational cost of all these tasks together scale as $O(N)$, with regards to both runtime and memory.

3.2.2. Point source illumination

This case is somewhat more complex than for the plan wave, due to the non-affine nature of the Cartesian-to-spherical coordinate transformation.

To obtain the bounding box of a triangle, a procedure to obtain the bounding box of an arbitrary straight line-segment in 3D space is required. Consider a line-segment with vertices located at $\vec{r}_0$ and $\vec{r}_1$. The segment can be represented by a parametric function:

$$\vec{r}(t) = \vec{r}_0 + (\vec{r}_1 - \vec{r}_0)t \begin{cases} x(t) = x_0 + (x_1 - x_0)t \\ y(t) = y_0 + (y_1 - y_0)t \\ z(t) = z_0 + (z_1 - z_0)t \end{cases} \tag{11}$$

where $t \in [0, 1]$. From (11) it follows that

$$\theta(t) = \cos^{-1}\left[\frac{z(t)}{\sqrt{x^2(t) + y^2(t) + z^2(t))}}\right] \tag{12}$$

$$\theta'(t) = \frac{[(x_1 z_0 - x_0 z_1)x(t) - (y_1 z_0 - y_0 z_1)y(t)]}{[x^2(t) + y^2(t) + z^2(t)]\sqrt{x^2(t) + y^2(t)}} \tag{13}$$

$$\phi(t) = \text{ArcTan}[x(t), y(t)] \tag{14}$$

$$\phi'(t) = \frac{y_1 x_0 - x_1 y_0}{x^2(t) + y^2(t)}. \tag{15}$$

The extreme values can now be obtained. Considering $\phi(t)$, it it clear from (15) that this is a monotonic function which will reach its extreme values at $t = 0$ and $t = 1$; Figure 3 shows example results. With regards to $\theta(t)$, the extreme values will occur at either of the endpoints ($t = 0$ and $t = 1$) or at the single stationary point, where $\theta'(t) = 0$. From (13) it follows that the stationary point location is at

$$t = \frac{[(x_0 z_1 - x_1 z_0)x_0 + (y_0 z_1 - y_1 z_0)y_0]}{[(x_1 z_0 - x_0 z_1)(x_1 - x_0) + (y_1 z_0 - y_0 z_1)(y_1 - y_0)]}. \tag{16}$$

Figure 4 shows segment projection example results.

A triangle has three segments. For each segment, use the analytical method to find the normal (grazing) buffer bounding box and record the extreme values, after finding all the extreme values, then determine the final bounding box of the triangle. This procedure is depicted in Fig 5.

Given the above procedure, there are actually three cases to be considered:

- **Triangles intersecting with the z-axis:** In this case the triangle will cover the whole ϕ-range of $[0, 2\pi]$. Let $\theta_{\min}$ and $\theta_{\max}$ be the extreme θ-values taken on along the three edges of the triangle. To find the θ-range, establish the sign of the z-coordinate of the intersection point. If it is positive, then the θ-range will be $[0, \theta_{\max}]$; if it is negative, then the θ-range will be $[\theta_{\min}, \pi]$.

- **Triangles crossing the half-plane $\phi = 0$:** In this case part of the triangle will lie around $\phi = 0$ in the normal (grazing) buffer plane and another part will lie around $\phi = 2\pi$. By temporarily rotating the triangle through 180° around the z-axis, a single bounding box for the triangle can be obtained from the extreme values of its edges. The ϕ-range can be cyclically shifted back by π, to obtain the two bounding boxes for the two parts of the actual triangle.

- **Normal triangles:** For all other triangles, their bounding boxes are obtained from the extreme values of the bounding boxes of their respective three edges.

For illustrative purposes, a mesh representing a sphere with the source point inside is considered in Figure 6. Examples of each of the three cases above are shown, as well as the projection of the whole mesh.

The triangles' depth and orientation information are calculated similarly as in (6) and (7), except that $\hat{\zeta}$ is used instead of $\hat{\eta}$. The average elemental buffer bounding box dimension Ψ_{ave}, is determined as

$$\Psi_{\text{ave}} = \frac{\sum_{n=1}^{N} \max\left(L_n^{\theta}, L_n^{\phi}\right)}{N} \tag{17}$$

with notations analogous to those in (8).

Finally, having established the bounding boxes of the individual elements, the global bounding box can readily be established as

$$\theta_{\min} \leqslant \theta \leqslant \theta_{\min} + L_{\text{mesh}}^{\theta} \tag{18}$$

$$\phi_{\min} \leqslant \phi \leqslant \phi_{\min} + L_{\text{mesh}}^{\phi}. \tag{19}$$

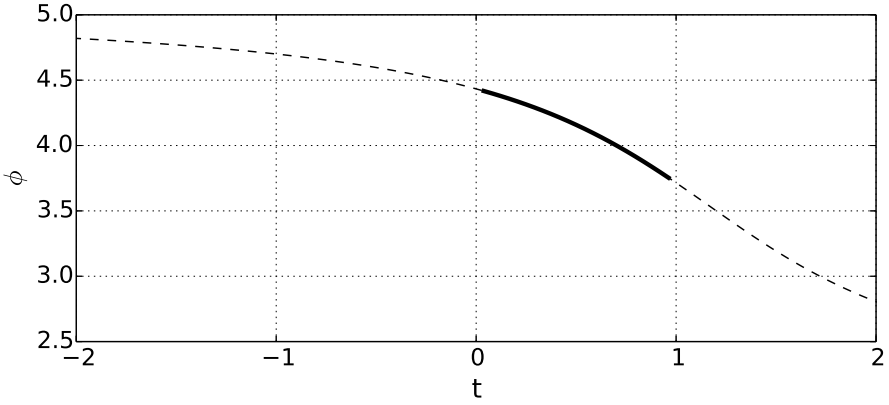

Figure 3: Finding the extreme values of ϕ for a projected segment (the straight-line extension of the segment is shown as a dotted line).

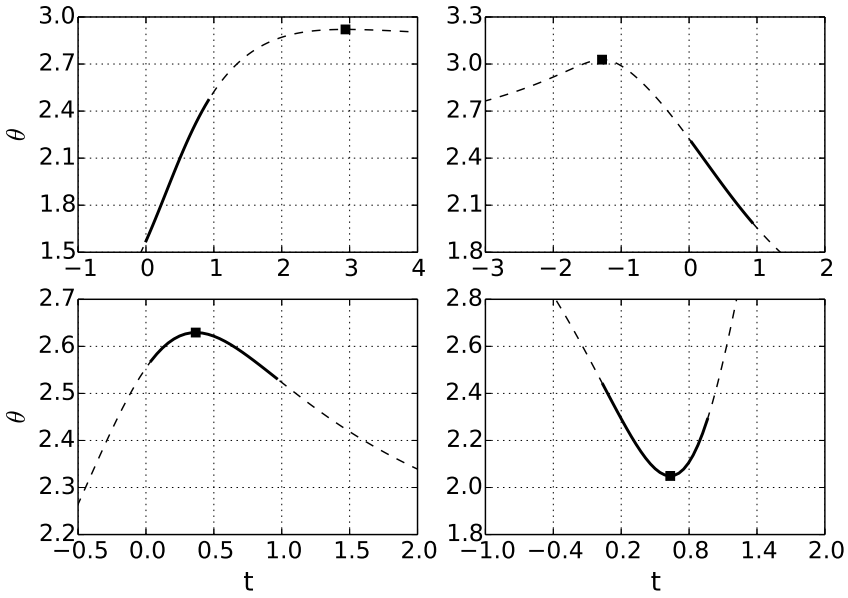

Figure 4: Finding the extreme values of θ for a projected segment (the straight-line extension of the segment is shown as a dotted line and the square marker indicates the stationary point). Top: examples of the stationary point external to the edge; bottom: examples of the stationary point internal to the edge.

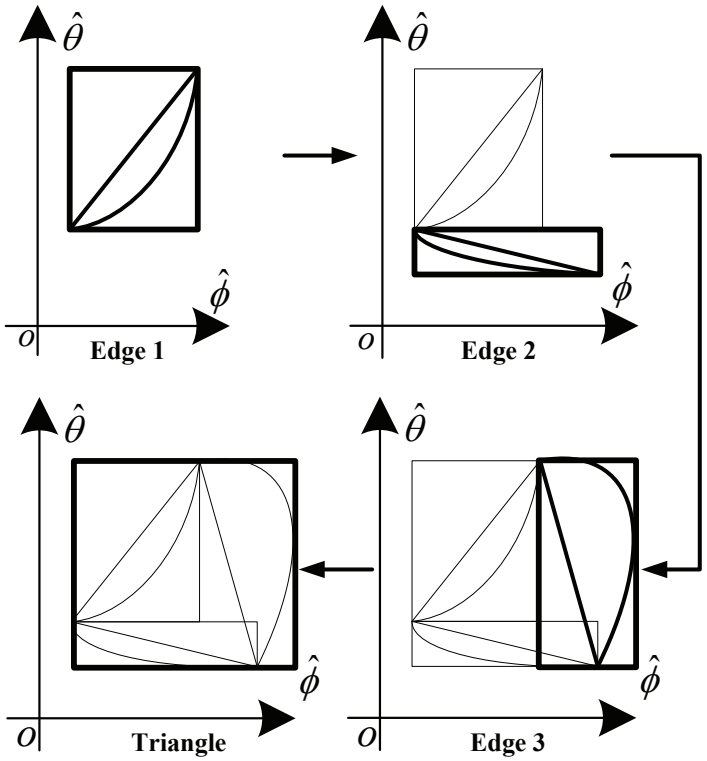

Figure 5: Analytical buffer bonding box determination for a normal triangle with point source illumination.

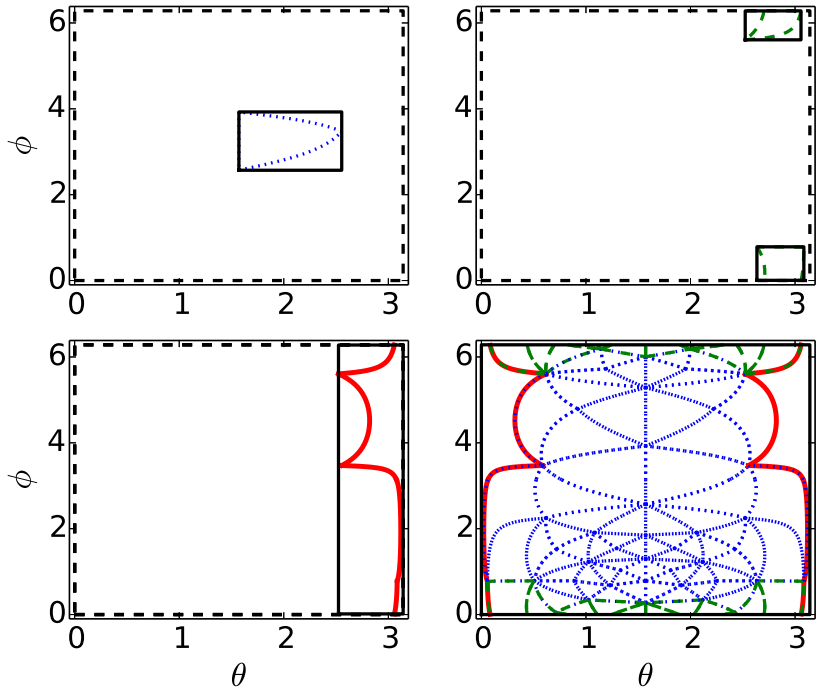

Figure 6: Examples of point source buffer bounding boxes. Clockwise from bottom-left: a triangle intersecting with the z-axis; the normal case; a triangle crossing the half-plane $\phi = 0$; projection of the complete mesh with triangle line-types indicating the three categories.

3.3. Buffer bounding box subdivision schemes

Two kinds of buffer bounding box subdivision schemes are used in the algorithm (or identically so, at lower levels in a recursive manner). The main difference between them is the buffer box subdivision size determination method.

After choosing the right type of subdivision scheme, each triangle's previously-recorded bounding box data is used to determine to which new, lower-level buffer box lists it should be added. The computational cost of all these tasks together scale as $O(N)$, with regards to both runtime and memory (where N here refers to the number of elements projecting into the bounding box to start off with).

The two subdivision schemes are now each described in more detail.

3.3.1. Average size buffer

The buffer bounding box is subdivided into smaller buffer boxes. The numbers of subdivisions in the two directions are obtained as follows:

$$N^a = \left\lceil \frac{L^a_{mesh}}{\beta l_{ave}} \right\rceil \quad N^b = \left\lceil \frac{L^b_{mesh}}{\beta l_{ave}} \right\rceil \qquad \text{For plane wave} \tag{20}$$

$$N^\theta = \left\lceil \frac{L^\theta_{mesh}}{\beta \Psi_{ave}} \right\rceil \quad N^\phi = \left\lceil \frac{L^\phi_{mesh}}{\beta \Psi_{ave}} \right\rceil \qquad \text{For point source} \tag{21}$$

where $\lceil \cdot \rceil$ refers to the ceiling function and with β a constant scaling factor. The total number of buffer boxes is thus equal to $N^a \times N^b$ ($N^\theta \times N^\phi$ for point source). All are identical and approximately square, with dimension βl_{ave} ($\beta \Psi_{ave}$ for point source). For

a homogeneous mesh, optimal performance is achieved with $\beta = 0.75$. If the mesh is not homogeneous, then typically the N buffer scheme will automatically be used instead (as described below), thus this value of β is a good choice.

3.3.2. N buffer

The N buffer is designed to yield a subdivision with the same or less non-empty, new lower-level buffer boxes than the number of elements in the original box. The procedure is quite straightforward. Here we use L^x_{mesh} to indicate the one axis dimension of the box to be subdivided and L^y_{mesh} as the other — for plane wave illumination, (x, y) will be (a, b) and for point source illumination, (x, y) will be (θ, ϕ). Let N_x denote the number of subdivision boxes along L^x_{mesh} and N_y the number along L^y_{mesh}, then these values can be solved from the following set of equations.

$$\begin{cases} N_x N_y &= N \\ \dfrac{N_x}{N_y} &= \dfrac{L^x_{mesh}}{L^y_{mesh}}. \end{cases} \tag{22}$$

If the average size buffer is used for an inhomogeneous mesh, then the total number of new buffer boxes can be very large, causing non-linear (expensive) runtime and storage scaling of the algorithm as a whole. The N buffer is used to avoid this problem. The subdivision procedure thus starts by calculating the number of new, lower-level boxes that will result from an average size buffer subdivision. If this number is larger than the number of elements in the box to start off with, then the N buffer approach is used instead.

3.4. Test for inhomogeneous meshing in a buffer box

Identify buffer boxes into which an excessive number of triangles are projecting (e.g. more than 100 — a pre-set value). Then test the mesh in such a buffer box for inhomogeneity. This test is quite simple: for each triangle in the buffer box, test if its bounding box falls completely inside the buffer box; if so, then add this triangle to a list. After all triangles in the buffer box have been processed, then count the number of triangles in the list. If the total number is more then a pre-set value, e.g. 20, then the buffer box is regarded as containing an inhomogeneous mesh, otherwise, the buffer box is regarded as containing a normal mesh.

3.5. Test for "relative flatness" at leaf-level, for the grazing part buffer

The "relative flatness" test referred to before, entails calculating the average normal vector of all triangles projecting into a buffer box. Then, the standard deviation of the dot-products between this average normal and the individual normals is calculated. If it is below a threshold, the surface formed by the grazing view triangles in that box, is regarded as relatively flat.

3.6. Final preparation for shadowing judgement and the judgement procedure

After all of the buffer boxes in both buffers (normal part and grazing part) have been established recursively, a list of elements projecting into each buffer box is on record. Before starting the shadowing judgement procedure, first sort every buffer box list according to the depth values of the elements. The buffers are then ready to be used for fast shadowing judgement of the control points.

For each control point, project it into the relevant buffer (normal part of grazing part, as described before) and find the buffer box to which it belongs. To determine the point's shadowing status, only those triangles listed in that specific buffer box which could possibly be in front of the given point, are considered. Specifically, suppose the n-th control point projects into a buffer box with the set of M triangles $\{m(1),\ m(2), ...,\ m(M)\}$ listed. The triangles to consider for shadowing testing are determined by the following criterion:

$$\text{If } d_{m(i)} \leqslant d_n \text{ then test the } m(i)\text{-th triangle} \qquad i \in \{1, ..., M\} \tag{23}$$

where d_n denotes the depth of the control point.

These selected triangles are each tested by determining if the projection of the n-th point lies inside the projection of the triangle onto the buffer plane as well as to determine if the n-th point lies beyond the extended plane of the triangle, or in front of it. Importantly, these triangles are checked in order of depth, from smallest to largest. As soon as shadowing is detected the status of the n-th point is 'shadowed' and the checking is terminated.

The multi-level, recursive buffer-based shadowing algorithm ensures than the number of elements listed in any given buffer box is independent of the total number of elements in the mesh. It follows that the cost of checking a given control point's shadowing status is $\mathcal{O}(1)$. Thus, if the number of control points is of $\mathcal{O}(N)$ (as it typically is), then the cost of the actual shadowing checking scales as $\mathcal{O}(N)$, with regards to both runtime and memory. The computational cost of the whole scheme thus scales as $\mathcal{O}(N)$.

4. Numerical results

The performance of the algorithm is assessed by considering challenging test cases and comparing results from three schemes/solvers:

1. The multi-level, recursive buffer-based shadowing algorithm.
2. A single-level, average size buffer.
3. The PO solver in FEKO (commercial software, [13]).

4.1. Plane wave illumination

Consider the mesh of a faceted model shown in Figure 7. The mesh is severely inhomogeneous, as described in the figure, in terms of a mesh-size parameter h. This mesh is illuminated at 1° grazing incidence — Figure 8 shows the decomposition of the mesh into two parts. Figure 9 shows the time-scaling results, obtained by varying the mesh size parameter h. Clearly, the present method yields perfectly linear time scaling, while the other two do not. The runtime benefits are significant, e.g. at about 10^5 mesh elements, the multi-level, recursive algorithm is a factor of 1000 faster than FEKO. Typically, PO could be used for much larger meshes, where the savings would be even more dramatic. It should however be kept in mind that this example is quite extreme, but that also serves to underscore the extreme robustness of the new method.

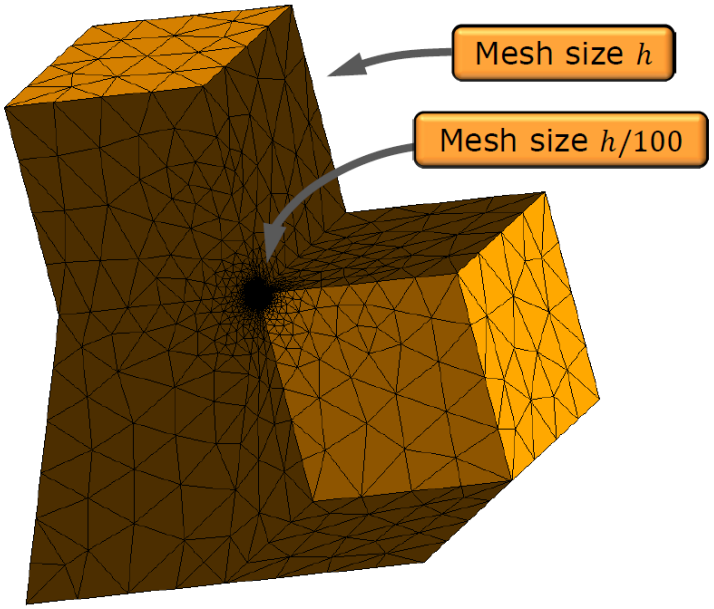

Figure 7: Inhomogeneously meshed, faceted model.

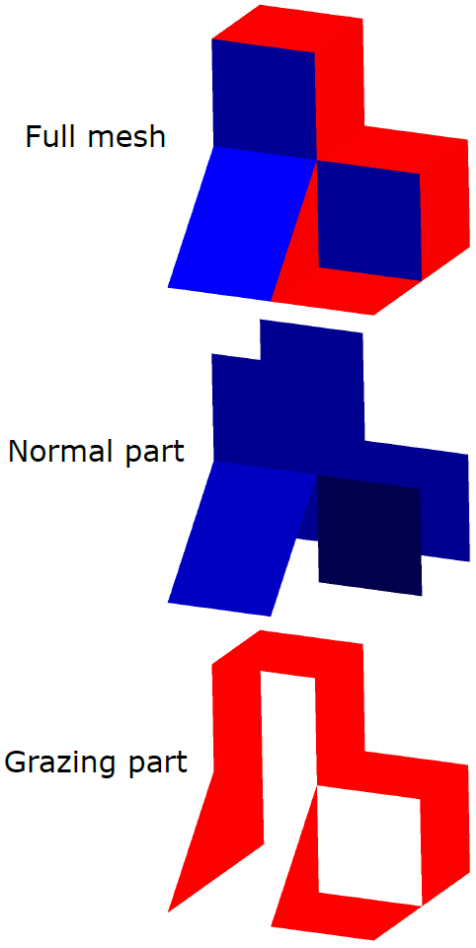

Figure 8: Normal view and grazing view parts for the faceted model under plane wave illumination.

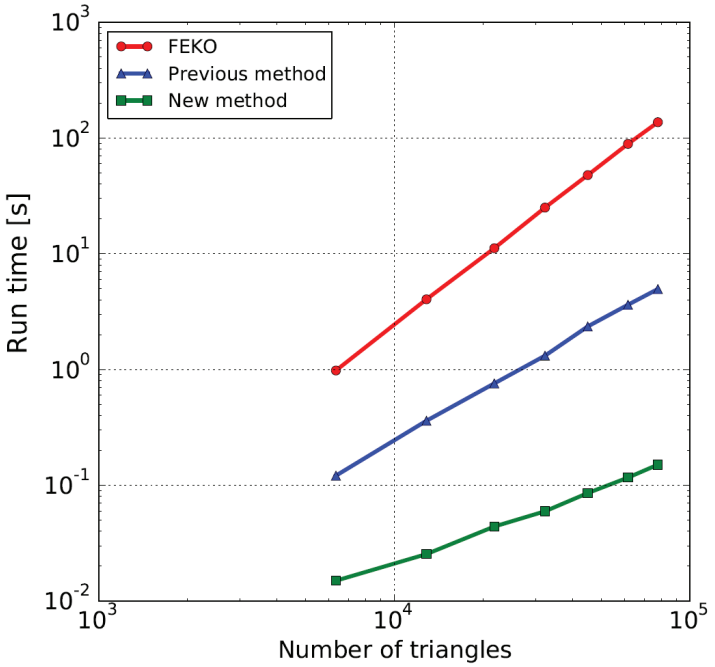

Figure 9: Shadowing determination runtime results for the inhomogeneously meshed, faceted model.

4.1.1. Point source illumination

A point source is located at a distance z above a flat surface with dimensions as shown in Figure 10. The surface is homogeneously meshed with 308, 330 triangle elements. The shadowing determination runtime is considered as a function of the distance z. As the dipole nears the surface, so will the extremity of the grazing incidence increase; also, as it nears the surface, so will the ratio between the distances to the nearest and farthest elements increase and with it, the level of mesh inhomogeneity after projection into the $\theta\phi$-buffer plane. Given the fact that PO is typically applied to large and smooth structures, it follows that this problem will be quite commonly encountered which makes this a very relevant test. Figure 11 shows the runtime results. The recursive method runtime is virtually independent of the distance to the surface, while the other two results exhibit a dramatic decrease in efficiency as the source nears the surface. This result demonstrates the recursive buffer method's ability to deal effectively with highly inhomogeneous meshes as well as point source grazing incidence.

Next, consider a meshed object with severe inhomogeneity. The mesh is shown in Figure 12 — it is a model of three spheres with radii 1 m, 0.25 m and 0.125 m. The point source is located at 1 mm above the biggest sphere's surface — Figure 13 shows the decomposition of the mesh into two parts. Figure 14 shows the time-scaling results, obtained by varying the mesh size. Again, the recursive method yields perfectly linear time scaling and in much less time than the other two methods.

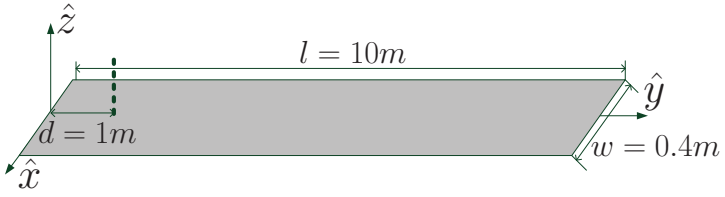

Figure 10: Flat strip geometry with the point source locations indicated by a dotted line.

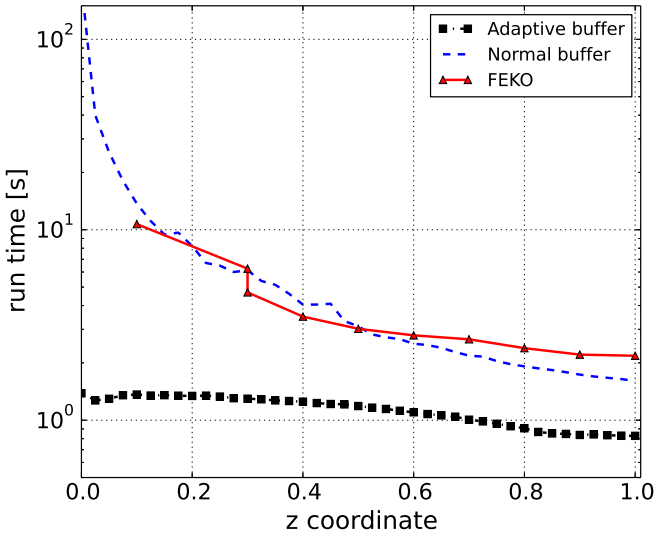

Figure 11: Shadowing runtime on a log scale, for the setup in Figure 10.

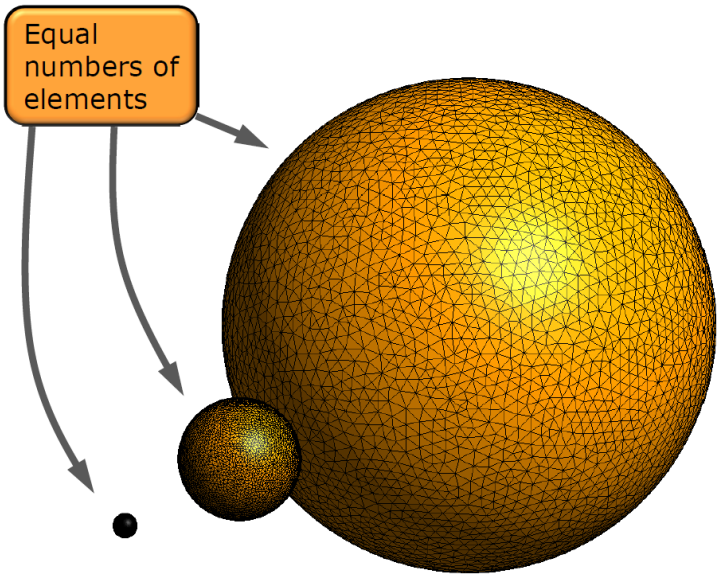

Figure 12: Inhomogeneously meshed, spheres model.

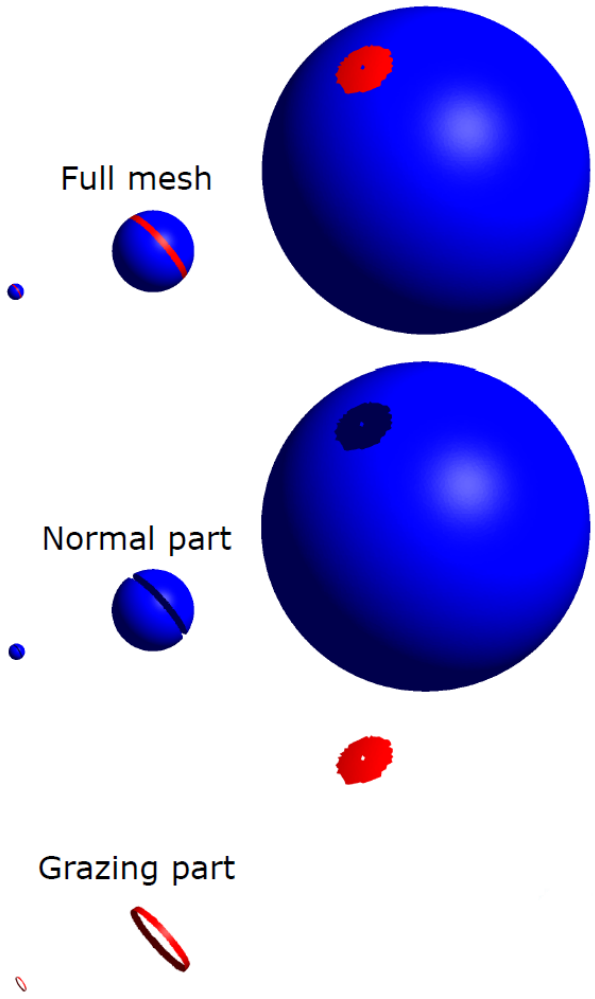

Figure 13: Normal view and grazing view parts for the spheres model under point source illumination.

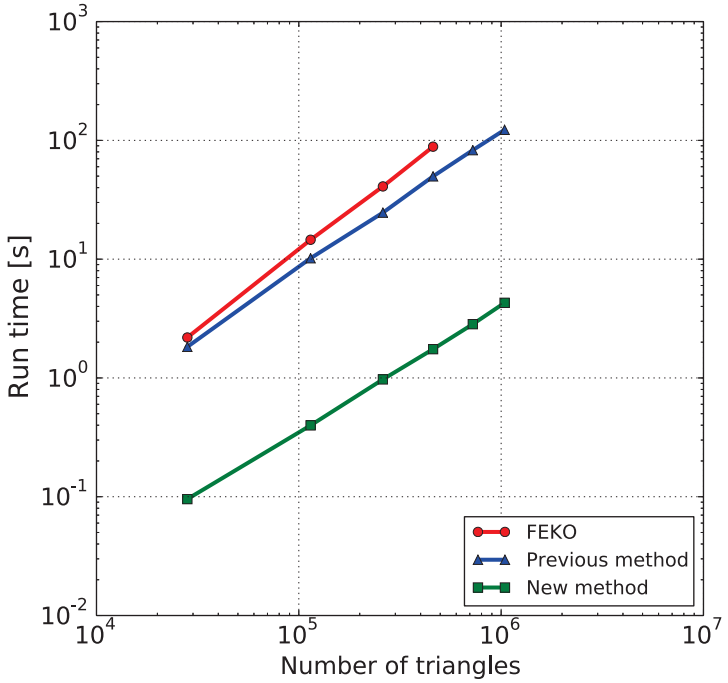

Figure 14: Shadowing determination runtime results for the inhomogeneously meshed, spheres model.

5. Conclusion

Shadowing determination for PO-based scattering analysis can be time consuming for electrically large, meshed objects. Although many publications on PO-based analysis schemes can be found in the literature, the practical aspects of shadowing determination, which forms a crucial part of any PO-based analysis scheme, has rarely been considered. In this paper, efficient shadowing determination algorithms have been presented for both plane wave and point source illumination. The schemes are based upon a recursive buffer concept and special attention is paid to optimizing performance for extremely inhomogeneous meshes and grazing incidence. The algorithm exhibits $\boldsymbol{O}(N)$ computational complexity in all cases. It is exceedingly robust. The scheme has been shown to out-perform the present version of an established commercial PO solver. The presented shadowing determination methods could be incorporated into any mesh-based PO code and are suitable for parallelization.

Acknowledgement

This work was funded by Altair Development S.A. (Pty) Ltd, developers of the EM simulation software suite FEKO.

References

[1] J. S. Asvestas, "The physical optics method in electromagnetic scattering," *J. Math. Phys.*, vol. 21, no. 2, pp. 290–299, 1980.

[2] D. Bouche, F. Molinet, and R. Mittra, *Asymptotic methods in electromagnetics*. Springer Science & Business Media, 2012.

[3] J. Pérez and M. F. Cátedra, "Application of physical optics to the RCS computation of bodies modeled with NURBS surfaces," *IEEE Trans. Antennas Propagat.*, vol. 42, no. 10, pp. 1404–1411, 1994.

[4] S. Sefi, "Ray tracing tools for high frequency electromagnetics simulations," Master's thesis, KTH Stockholm, 2003.

[5] F.-T. Zha, S.-X. Gong, Y.-X. Xu, Y. Guan, and W. Jiang, "Fast shadowing technique for electrically large targets using z-buffer," *Journal of Electromagnetic Waves and Applications*, vol. 23, no. 2-3, pp. 341–349, 2009.

[6] J. Alvarez, I. Gómez-Revuelto, J. M. Alonso, L. E. Garcia-Castillo, and M. Salazar-Palma, "Fully coupled multi-hybrid finite element method–method of moments–physical optics method for scattering and radiation problems," *Electromagnetics*, vol. 30, no. 1-2, pp. 3–22, 2010.

[7] A. Thomet, G. Kubické, C. Bourlier, and P. Pouliguen, "Improvement of iterative physical optics using the physical optics shadow radiation," *Progress In Electromagnetics Research M*, vol. 38, pp. 1–13, 2014.

[8] E. A. Haines and D. P. Greenberg, "The light buffer: A shadow-testing accelerator," *IEEE Computer Graphics and Applications*, pp. 6–16, September 1986.

[9] J. M. Rius, M. Ferrando, and L. Jofre, "GRECO: Graphical electromagnetic computing for RCS prediction in real time," *IEEE Antennas and Propagation Magazine*, vol. 35, no. 2, pp. 7–17, 1993.

[10] F. Saez de Adana, O. Gutiérrez, I. González, M. F. Cátedra, and L. Lozano, *Practical Applications of Asymptotic Techniques in Electromagnetics*. Boston: Artech House, 2011.

[11] D. P. Xiang and M. M. Botha, "Aspects of efficient shadowing calculation for physical optics analysis of meshed objects," in *2014 International Conference on Electromagnetics in Advanced Applications (ICEAA2014)*. IEEE, 2014, pp. 492–495.

[12] ——, "Efficient shadowing determination at grazing incidence, for mesh-based physical optics scattering analysis," Submitted for publication.

[13] Altair Engineering Inc., *FEKO User's Manual Suite 7.0*, Altair Development S.A. (Pty) Ltd., August 2014.

Appendix C

Journal paper — fast MRPO [52]

D. P. Xiang and M. M. Botha, "**MLFMM-based, fast multiple-reflection physical optics for large-scale electromagnetic scattering analysis,**" August 2016, submitted for publication.

MLFMM-based, fast multiple-reflection physical optics for large-scale electromagnetic scattering analysis

Dao P. Xiang[a], Matthys M. Botha[a,*]

[a]*Department of Electrical and Electronic Engineering, Stellenbosch University, Private Bag X1, Matieland 7602, Stellenbosch, South Africa*

Abstract

The asymptotic, physical optics (PO) approximation is applicable to electromagnetic scattering analysis of electrically large, conducting objects, which is important for various applications, such as radar cross-section (RCS) calculations. It relates the incident magnetic field to the induced surface current at points on a scatterer's surface with line-of-sight visibility to the source. Here, the focus is on mesh-based PO, using a triangle element mesh with standard Raviart-Thomas/Rao-Wilton-Glisson basis functions to represent the surface current density. The multiple-reflection PO (MRPO) method involves applying the PO approximation to the field radiated by the present current solution towards the scatterer itself, to account for successive internal reflections. The visibility status between every pair of basis functions is required, taking into account all geometry. In a conventional implementation, internal reflected field calculation and internal shadowing determination runtimes both scale as O(N^2). N denotes the number of mesh elements. In this paper an accelerated version of the mesh-based MRPO method is presented: fast MRPO (FMRPO). The multi-level, fast multipole method (MLFMM) is used to accelerate internal reflected field calculation. The key aspect to achieving acceleration for general geometries, is to incorporate internal shadowing into the MLFMM interaction tree. This requires an alteration to the inter-group interaction criterion of the MLFMM, as well as efficient evaluation of inter-group shadowing status flags, to preserve the beneficial cost-scaling property of the MLFMM. Algorithmic parameters are introduced, which control the accuracy of internal shadowing determination. The FMRPO runtime scales as quasi-O(N(log(N))), depending on the specific geometry. Numerical results are presented, demonstrating accuracy and efficiency for general scattering objects. There is no fundamental limit to the electrical size of the geometries that can be solved with FMRPO.

Keywords: Computational electromagnetics, magnetic field integral equation (MFIE), shadow judgement, iterative physical optics (IPO), recursive solution, multi bounce

*Corresponding author
Email address: mmbotha@sun.ac.za (Matthys M. Botha)

1. Introduction

The analysis of electromagnetic scattering by electrically large, conducting objects has received much attention in the literature. It is important for various applications, such as radar cross-section (RCS) calculations, as well as analysis of reflector antennas, antenna illumination of large structures, etc. Electrically small scatterers can be treated efficiently with the physically rigorous, method of moments (MoM) [1, 2], while electrically larger structures are amenable to solution with accelerated MoM formulations, relying on matrix compression through factorization. The most well-known and widely-used of these, is the multi-level, fast multipole method (MLFMM) [3]. The MLFMM relies on iteratively solving the system matrix equation, thus preconditioning is required and convergence can be a problem. As electrical size grows, so does the applicability of asymptotic methods, which rely on limiting assumptions to characterize local field behaviour. The asymptotic, physical optics (PO) approximation relates the incident magnetic field to the induced surface current at points on a scatterer's surface with line-of-sight visibility to the source [4, 5, 6]. When using the PO approximation to model multiple reflections with rigorous treatment of internal shadowing, which is denoted the multiple-reflection PO (MRPO) method in this paper, it has some distinct advantages in the asymptotic analysis context, as discussed below. However, MRPO is hampered by significant runtime bottlenecks. In this paper an accelerated version of the mesh-based MRPO method is presented, which is denoted as fast MRPO (FMRPO), which overcomes the computational bottlenecks associated with the conventional version. The acceleration leverages the MLFMM concept.

Asymptotic methods have long been used for scattering analysis. These methods fall into two main categories: (i) ray-based methods, such as geometrical optics (GO) and the uniform theory of diffraction (UTD) [7, 6], and shooting-and-bouncing-rays (SBR) [8]; and (ii) current-based methods employing the PO approximation. The first category can be subdivided into ray-tracing (GO, UTD) and ray-launching (SBR) methods. Ray-tracing methods work by identifying geometry features and applying canonical solutions locally, to model reflections and diffractions along valid ray paths from the source to the observation point.

SBR techniques are based on launching ray tubes and tracking their specular reflections [8]. Equivalent sources are placed where rays interact with the structure, or at the points where they leave an enclosing surface. Various refinements and extensions to SBR have been published over the years, cf. [9, 10, 11]. SBR only requires that the geometry representation be an accurate representation of the true geometry. Thus a very course mesh or a NURBS-based CAD model may often suffice. Generally, the number of rays must be proportional to the scatterer's surface area, as measured in square wavelengths [12, 13]. Adaptive ray-launching has been proposed as a way to reduce the number of required rays [14].

The PO approximation continues to find widespread applications in scattering analysis [15, 16, 17, 18]. It is valid for structures consisting of electrically large surfaces of which the radius of curvature is substantially larger than the wavelength [5, 4]. In the MRPO, the PO approximation with rigorous shadowing is applied to the field due to the present current solution itself, to calculate successive internal reflections to the scatterer [19]. In the MRPO it is therefore necessary to establish the visibility status between every pair of source and observation points on the scatterer's surface. MRPO is thus similar to SBR in some respects, but with the crucial difference that successive reflections are based on full integration over all sources, rather than only tracking of ray tube

reflections. Therefore, higher accuracy can be expected from PO-based reflections than from SBR-based reflections, but at significantly higher computational cost [13, 11, 16]. Since the surface current is effectively solved all over the structure with PO, its numerical representation is an important aspect in any PO-based method. Two types of surface current representations are often used in PO methods: a NURBS-based, CAD model representation [20, 15, 16], or a mesh of triangle elements with size proportional to the wavelength, upon which standard MoM basis functions are used (e.g. [21, 22, 23]). The number of basis function coefficients will be proportional to the scatterer's surface area, as measured in square wavelengths (similar to the number of rays in the SBR method). Working with a CAD model has the advantage that a large mesh does not need to be generated or stored. However, resolving shadow boundaries accurately can become a challenge and furthermore, the wavelength-scale details in the current representation must still be resolved. A mesh-based representation allows for completely general current variations and shadow boundaries can be accurately represented with ease. Here the focus is on mesh-based PO.

Apart from MRPO which rigorously holds to the PO approximation with regards to shadowing, there is also the iterative PO (IPO) method, which is like the MRPO, but with a sweeping, simplifying assumption on shadowing determination [24, 25]. Geometry in between any given source basis function and an observation point is effectively ignored in the IPO. (Note that the designation IPO was also used in [19], but here that formulation is referred to as MRPO, distinguishing it from the work in [24, 25]).) This means that an IPO iteration cannot be interpreted as a physical reflection. Rather, the IPO can be understood as a Picard-type iterative solution (cf. [26]) of the magnetic field integral equation (MFIE), with partial inclusion of shadowing properties, to accelerate convergence for PO-suitable scatterers. The benefits of IPO above the rigorous MRPO is that dramatically less computational effort for shadowing determination is required and that shadow boundaries tend to be smooth for the IPO, though still non-physical [25]. The drawbacks of IPO are (i) an iterative process of which the convergence is not guaranteed, and (ii) while MRPO cycles have a clear physical interpretation, IPO cycles do not. The focus here is on the MRPO, rather than IPO.

A bottleneck that is common to both MRPO and IPO, is the cost of evaluating internal reflected fields. These fields are evaluated by integrating over all visible sources. Doing this conventionally, the runtime cost scales as $\mathcal{O}({N_\mathrm{T}}^2)$, with N_T denoting the number of mesh elements. Such integrals can be accelerated with the MLFMM or similar fast methods for evaluating integral equations at a large number of observation points. In [24, 25] the fast far field approximation (FaFFA) is used for this purpose, bringing down the field evaluation cost to $\mathcal{O}({N_\mathrm{T}}^{3/2})$. In [27, 28, 29] the MLFMM is used, which brings down the cost to $\mathcal{O}(N_\mathrm{T} \log N_\mathrm{T})$. This same cost scaling is achieved using the multilevel non-uniform grid algorithm, in [30]. The second bottleneck relates to internal shadowing determination. In the accelerated MRPO work of [28, 29], this bottleneck is not dealt with, since only cases are treated where all internal shadowing can be incorporated a priori (e.g. full visibility). In the accelerated IPO results of [24, 25], test cases with internal shadowing are shown, but the incorporation of shadowing into the fast field evaluation scheme is not discussed, nor the computational complexity of the shadowing determination. In [27] it is noted that shadowing is incorporated into the MLFMM-accelerated IPO method, via the MLFMM translation operator. However, this is done based on average element normal vectors as an indication of group orientation and moreover, no mention is made of partial visibility. Apparently the MLFMM interaction

tree is left unchanged. In [30] shadowing is incorporated into the accelerated IPO via the use of two different kernels and iterative shadowing corrections to the current. The procedure for determining the shadowing information incorporated into the two kernels is not discussed. It follows that a comprehensively accelerated MRPO formulation has not been presented to date. Even for accelerated versions of the IPO, a clear and detailed explanation of how the IPO's reduced shadowing condition is incorporated into the accelerated integrals and how it affects the time-scaling, is not available in the literature.

This paper starts by presenting the conventional MRPO method on the continuous level, as well as in discretized form, in Section 2. The discretization scheme is chosen to be a conforming mesh of flat triangle elements, with edge-associated, Raviart-Thomas, mixed first-order basis functions, also known as Rao-Wilton-Glisson (RWG) basis functions [31, 1, 2]. This is a very standard, well-known and widely-adopted discretization scheme. Exploring the use of higher-order basis functions is beyond the scope of the present work. Specific attention is paid to the MRPO formulation for open surfaces, where modelling of currents on both sides independently, is required — this detailed documentation of the MRPO method is one of the paper's contributions. Section 3 presents the MLFMM-accelerated MRPO method, denoted by FMRPO. This is the main contribution of the paper. To use the MLFMM algorithm for internal field calculations, shadowing effects must be incorporated into the factorized version of the field evaluation matrix, without compromising speed and accuracy. This is done by introducing inter-group shadowing status flags which are used to alter the standard MLFMM interaction tree. Evaluating these flags efficiently is an important aspect of the FMRPO, such that the beneficial cost-scaling property of the MLFMM is preserved. Algorithmic parameters are introduced, through which the accuracy of shadowing determination can be controlled. Computational cost scaling is discussed in detail. Section 4 presents a range of numerical results, chosen to evaluate the accuracy and efficiency of the FMRPO. Some results are included to demonstrate the accuracy of the MRPO itself, given that it can now be applied for the first time, to complex, electrically large scatterers at reasonable computational cost.

2. Conventional MRPO method

A positive frequency convention of $e^{j\omega t}$ ($j = \sqrt{-1}$) is adopted, with all time-harmonic electromagnetic quantities expressed throughout as phasors; $\omega > 0$ denotes the angular frequency.

2.1. Mesh-based, single-reflection PO formulation

Consider a three-dimensional (3D), perfect electrically conducting (PEC) object with volume Ω and closed boundary surface $\Gamma = \partial\Omega$ with outward-pointing unit normal vector $\hat{n}$, in free space. The well-known PO approximation for the induced surface current density due to a given incident magnetic field $\boldsymbol{H}^{\text{inc}}$ upon such an object, is as follows [5, 4, 6]:

$$\boldsymbol{J}^{\text{PO}}(\boldsymbol{r}) = \begin{cases} 2\hat{n} \times \boldsymbol{H}^{\text{inc}}(\boldsymbol{r}) & \text{Visible to the source} \\ 0 & \text{Shadowed} \end{cases} \tag{1}$$

where visibility of a point $\boldsymbol{r} \in \Gamma$ is defined as line-of-sight from the source, without any obstructions from other parts of Γ. In the case of a PEC half-space the PO approximation (1) becomes exact, which follows from image theory. The PO approximation generally becomes increasingly accurate as the object and its local radius of curvature grows in electrical size, as already observed in the introduction. The PO approximation can also be regarded as a first-order approximation of the MFIE, where interactions between currents have been discarded, except for the assumption that the field radiated by the induced currents on the illuminated part of Γ, cancels out the incident field upon the shadowed part. Equation (1) can be rewritten more succinctly in terms of a continuous shadowing function $\delta_{\boldsymbol{r}}^{\text{inc}}$, which is equal to unity for points with line-of-sight visibility to the source and zero otherwise:

$$\boldsymbol{J}^{\text{PO}}(\boldsymbol{r}) = 2\delta_{\boldsymbol{r}}^{\text{inc}}\hat{n} \times \boldsymbol{H}^{\text{inc}}(\boldsymbol{r}). \tag{2}$$

The current density is discretized with RWG basis functions on a homogeneous, conforming mesh of flat triangle elements [31, 1, 2]. The union of all elements represents Γ. A basis function is associated with each edge in the mesh; the support of each basis function is the union of the two triangle elements sharing its associated edge, as shown in Figure 1. With N_{E} unique (shared) edges in the mesh, the discretized representation of the current is

$$\boldsymbol{J} = \sum_{n=1}^{N_{\text{E}}} I_n \boldsymbol{f}_n \tag{3}$$

where $\boldsymbol{f}_n$ is the RWG basis function associated with the n-th edge and I_n is its coefficient. Now define a field projection operator for the coefficient at the n-th edge, as

$$\begin{aligned} \mathcal{I}_n(\boldsymbol{H}) &\equiv \frac{2\left(\hat{n}(\boldsymbol{r}_n) \times \hat{\ell}_n\right) \cdot \left[\hat{n}(\boldsymbol{r}_n) \times \boldsymbol{H}(\boldsymbol{r}_n)\right]}{\left(\hat{n}(\boldsymbol{r}_n) \times \hat{\ell}_n\right) \cdot \boldsymbol{f}_n(\boldsymbol{r}_n)} \\ &= 2\hat{\ell}_n \cdot \boldsymbol{H}(\boldsymbol{r}_n) \end{aligned} \tag{4}$$

with $\boldsymbol{r}_n$ and $\hat{\ell}_n$ denoting the midpoint of the n-th edge and its right-directed tangential unit vector, respectively, as shown in Figure 1. The denominator was dropped in (4), because it represents the normal component of the RWG basis function to its associated

edge, which is equal to unity by definition [31]. Next define the incident field shadowing coefficient:

$$\delta_n^{\text{inc}} = \begin{cases} 1 & \text{For } \boldsymbol{r}_n \text{ visible to the source} \\ 0 & \text{For } \boldsymbol{r}_n \text{ shadowed.} \end{cases} \tag{5}$$

It follows that the discretized current solution can be obtained according to (2) as

$$\boldsymbol{J}_{(1)}^{\text{PO}} = \sum_{n=1}^{N_{\text{E}}} \delta_n^{\text{inc}} \mathcal{I}_n(\boldsymbol{H}^{\text{inc}}) \boldsymbol{f}_n. \tag{6}$$

This is known as the mesh-based, single-reflection PO (SRPO) method. The fact that only the n-th basis function has a component perpendicular to the n-th edge, has been exploited for the projection of the incident field onto the discretized current representation, in (6). The SRPO solution only accounts for a single reflection off the scatterer, hence the "(1)" subscript used in (6).

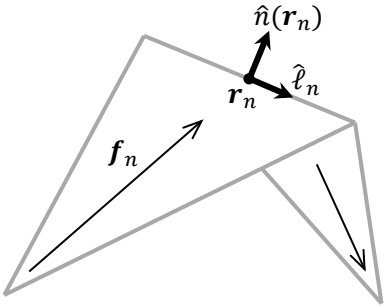

Figure 1: RWG basis function domain for the n-th edge, showing the outward-pointing normal vector at the edge midpoint $\hat{n}(\boldsymbol{r}_n)$, and the right-directed edge vector $\hat{\ell}_n$, such that $(\hat{n}(\boldsymbol{r}_n) \times \hat{\ell}_n) \cdot \boldsymbol{f}_n(\boldsymbol{r}_n) = 1$.

2.2. Mesh-based, multiple-reflection PO formulation

Considering the PO approximation on the continuous level (2), it is apparent that one could apply it successively. The induced current due to the first reflection, becomes a source for a secondary reflection which takes internal shadowing into account, and so forth. This leads to a recursive formula which is a generalization of (2) for the current after K reflections. To express this formally, first define the magnetic field integral operator as

$$\mathcal{H}(\boldsymbol{J})(\boldsymbol{r}) \equiv \int_{\text{supp}(\boldsymbol{J})} \nabla G_0(\boldsymbol{r}, \boldsymbol{r}') \times \boldsymbol{J}(\boldsymbol{r}')\, dS' \tag{7}$$

which yields the magnetic field at the observation point $\boldsymbol{r}$, as radiated by the surface current distribution $\boldsymbol{J}$, of which the domain of support is denoted by $\text{supp}(\boldsymbol{J})$ in (7) [2]. Above, the free space scalar Green function is defined as

$$G_0(\boldsymbol{r}, \boldsymbol{r}') = \frac{e^{-jk_0|\boldsymbol{r}-\boldsymbol{r}'|}}{4\pi|\boldsymbol{r}-\boldsymbol{r}'|} \quad \text{with} \quad k_0 = \frac{2\pi}{\lambda_0} \quad \{\lambda_0 \text{ is the wavelength}\}. \tag{8}$$

The recursive formula yielding the current after K reflections, is as follows [19]:

$$\boldsymbol{J}_{(K)}^{\text{PO}}(\boldsymbol{r}) = \boldsymbol{J}_{(1)}^{\text{PO}}(\boldsymbol{r}) + 2\hat{n} \times \mathcal{H}\left(\delta_{\boldsymbol{r}}^{\boldsymbol{r}'} \boldsymbol{J}_{(K-1)}^{\text{PO}}(\boldsymbol{r}')\right)(\boldsymbol{r}) \quad \{\boldsymbol{r} \in \Gamma\} \tag{9}$$

where $\delta_{\boldsymbol{r}}^{\boldsymbol{r}'}$ is the continuous shadowing function, which is equal to unity for two points with line-of-sight visibility. It is zero if there is an obstruction, or if the points lie on

the same flat PEC plane, or if they are co-incident. This is the multiple-reflection PO approximation, which will intuitively be more accurate than the standard PO approximation (2) when the scattering object's shape supports internal reflections. Clearly (9) reduces to (2) for $K = 1$.

Given the RWG-based current representation (3) and projection operator (4), the mesh-based MRPO method can be obtained from (9). Define the inter-edge shadowing coefficient as

$$\delta_n^m = \begin{cases} 1 & \text{For } \boldsymbol{r}_n \text{ visible from } \boldsymbol{r}_m \\ 0 & \text{For } \boldsymbol{r}_n \text{ shadowed from } \boldsymbol{r}_m, \text{ or } n = m. \end{cases} \tag{10}$$

Furthermore, define the following notation for the RWG-based solution current after K reflections:

$$\boldsymbol{J}_{(K)}^{\mathrm{PO}} = \sum_{n=1}^{N_{\mathrm{E}}} I_{n(K)} \boldsymbol{f}_n. \tag{11}$$

The recursive formula for the discretized current after K reflections now follows as

$$\boldsymbol{J}_{(K)}^{\mathrm{PO}} = \boldsymbol{J}_{(1)}^{\mathrm{PO}} + \sum_{n=1}^{N_{\mathrm{E}}} \mathcal{I}_n \left(\sum_{m=1}^{N_{\mathrm{E}}} \delta_n^m I_{m(K-1)} \boldsymbol{\mathcal{H}}(\boldsymbol{f}_m) \right) \boldsymbol{f}_n \tag{12}$$

where $\boldsymbol{J}_{(1)}^{\mathrm{PO}}$ in the above expression is from (6). Henceforth, $\boldsymbol{J}_{(K)}^{\mathrm{PO}}$ will refer to the discretized current solution after K reflections (not the continuous version).

It is convenient to express the MRPO recursion relation (12) in linear algebra format. Let $\{I_{(K)}\}$ denote the column vector of basis function coefficients for the current after K reflections, then

$$\{I_{(K)}\} = \{I_{(1)}\} + [C]\{I_{(K-1)}\} \tag{13}$$

with the entries of the $N_{\mathrm{E}} \times N_{\mathrm{E}}$ matrix $[C]$ following from (12), (7) and (4) as

$$\begin{aligned} C_{nm} &= \delta_n^m \mathcal{I}_n \left(\boldsymbol{\mathcal{H}}(\boldsymbol{f}_m) \right) \\ &= 2\delta_n^m \hat{\ell}_n \cdot \boldsymbol{\mathcal{H}}(\boldsymbol{f}_m)(\boldsymbol{r}_n) \\ &= 2\delta_n^m \hat{\ell}_n \cdot \int_{\mathrm{supp}(\boldsymbol{f}_m)} \nabla G_0(\boldsymbol{r}_n, \boldsymbol{r}') \times \boldsymbol{f}_m(\boldsymbol{r}')\, dS' \\ &= 2\delta_n^m \int_{\mathrm{supp}(\boldsymbol{f}_n)} \boldsymbol{s}_n(\boldsymbol{r}) \cdot \left[\int_{\mathrm{supp}(\boldsymbol{f}_m)} \nabla G_0(\boldsymbol{r}, \boldsymbol{r}') \times \boldsymbol{f}_m(\boldsymbol{r}')\, dS' \right] dS \end{aligned} \tag{14}$$

where n refers to the row and m to the column. In the last instance, the expression was rewritten as a double integral with a testing function, which will be useful later-on. The testing function relating to the n-th basis function is defined in terms of a 3D Dirac delta function, as

$$\boldsymbol{s}_n(\boldsymbol{r}) = \delta(\boldsymbol{r} - \boldsymbol{r}_n)\hat{\ell}_n. \tag{15}$$

2.3. Open surfaces

Thus far, a solid PEC body with closed boundary surface Γ has been considered. Often in scattering analysis, it is of interest to analyse a scatterer which is defined as an open PEC surface in 3D and meshed as such. This case can be cast into the format of (13) after noting the following:

- View the open PEC surface as a volume representing an infinitely thin sheet. In such a case the above theory dictates that current must be independently modelled on both sides, with associated outward-pointing normal vectors of opposite directions.
- Associate two independent basis functions with each internal edge of the surface, one on each side of the surface.
- No basis functions are associated with the open edges of the surface (unshared mesh edges), in order to adhere to the law of charge conservation.

To distinguish between the two sides of a surface, it is convenient to refer to the "positive" ('p') and "negative" ('n') sides. The MRPO matrix formulation (13) can now be rewritten as follows:

$$\begin{Bmatrix} I^{\mathrm{n}}_{(K)} \\ I^{\mathrm{p}}_{(K)} \end{Bmatrix} = \begin{Bmatrix} I^{\mathrm{n}}_{(1)} \\ I^{\mathrm{p}}_{(1)} \end{Bmatrix} + \begin{bmatrix} C^{\mathrm{nn}} & C^{\mathrm{np}} \\ C^{\mathrm{pn}} & C^{\mathrm{pp}} \end{bmatrix} \begin{Bmatrix} I^{\mathrm{n}}_{(K-1)} \\ I^{\mathrm{p}}_{(K-1)} \end{Bmatrix} \tag{16}$$

where the entries of each sub-matrix are defined according to (14). E.g. in the case of $[C^{\mathrm{pn}}]$, testing functions on the positive side are used, together with source basis functions on the negative side. Clearly, the shadowing coefficient would be zero for a testing function and a source basis function associated with the same mesh edge, but on opposite sides of the surface.

If the scatterer is described by a single, closed surface, of which the outside is labelled as the positive side, then all negative side currents can be set to zero, in which case (16) simplifies back to (13). In general, a scattering object can contain both open and closed parts, as well as junctions where three or more surfaces meet. For open surface parts, positive side normals must be aligned to all point away from the surface on the same side. At junctions, currents are modelled on all single-surface sides independently. Also, as part of mesh pre-processing closed parts must be identified such that internal currents can be discarded from the outset, to avoid unnecessary computational effort.

2.4. Computational cost

The computational cost will be defined in terms of the number of mesh elements (denoted by N_{T}). Clearly, $N_{\mathrm{T}} \propto N_{\mathrm{E}}$. The two main runtime costs for the MRPO, is (i) determining the inter-element shadowing coefficient values (10) and (ii) evaluating the successive, internally reflected fields, i.e. the matrix-vector product in (13). The cost of determining the shadowing status of all edge midpoints from a single observation point $\boldsymbol{r}_n$ [i.e. $\delta^1_n, ..., \delta^{N_{\mathrm{E}}}_n$ in the case of (13)] is of the order $O(N_{\mathrm{T}}) \sim O({N_{\mathrm{T}}}^2)$, depending on the sophistication of the shadowing algorithm and the particular mesh properties (cf. [22, 32]). Therefore the total shadowing determination cost for all observation points, scales at best as $O({N_{\mathrm{T}}}^2)$. The cost of the internal field calculation for a single reflection scales as $O({N_{\mathrm{T}}}^2)$, since $[C]$ is a fully populated matrix for general geometries. Thus, the total runtime of the conventional MRPO scales as $O({N_{\mathrm{T}}}^2) \sim O({N_{\mathrm{T}}}^3)$. As N_{T} increases, this quickly becomes prohibitively expensive. Since the MRPO is most applicable to electrically large scatterers, it has thus not found widespread applications to date.

Finally, there is also the cost of calculating the initial, single-reflection solution $\boldsymbol{J}^{\mathrm{PO}}_{(1)}$. With the latest incident-field shadowing determination schemes, this can be accomplished in $O(N_{\mathrm{T}})$ time [32], hence its contribution to the overall MRPO runtime is marginal.

3. Fast MRPO method (FMRPO)

To accelerate the MRPO method, the two costly aspects identified in Section 2.4 must be addressed. Consider the internal field calculations. This amounts to a matrix-vector product, with the matrix taking the form of a standard MFIE-based, MoM matrix using collocation testing, but with the diagonal entries set to zero and with the incorporation of the inter-element shadowing coefficient into the integrand. As noted in the introduction, the MLFMM is a well-known and highly successful method to accelerate MoM matrix-vector products, such as resulting from the MFIE for PEC objects in free space, through factorization of the matrix. However, it cannot be directly applied to (13), due to the presence of the shadowing coefficient in (14). In this section, the incorporation of the MLFMM into (13) (and (16)) through use of inter-group shadowing status flags, is first presented. Subsequently, a method of efficiently determining the inter-group shadowing status flags is described, followed by a discussion on the computational cost of the complete, accelerated method.

3.1. MLFMM-based internal field calculation

In the FMM, space is partitioned with cubic boxes of side-length D. All basis functions with their edge centre-points falling into a certain box, are collectively called a group. Each group has a centre which corresponds to the centroid of its defining box. Let $\boldsymbol{r}_P$ and $\boldsymbol{r}_Q$ be the centres of the groups to which $\boldsymbol{f}_n$ and $\boldsymbol{f}_m$ belong to, respectively; with $\boldsymbol{r}_{PQ} = \boldsymbol{r}_P - \boldsymbol{r}_Q = r_{PQ}\hat{r}_{PQ}$. Since the entries of matrix $[C]$ has been cast in the form of an MFIE-based reaction integral, FMM theory can be used to rewrite (14) as follows [3, 2]:

$$C_{nm} = \oint \boldsymbol{V}_{nP}(\hat{k}) \cdot \left[2\Delta_P^Q \, \tilde{\alpha}_{PQ}(\hat{k}) \right] \boldsymbol{V}_{Qm}(\hat{k}) \, d^2\hat{k} \qquad \{r_{PQ} \geqslant 2D\} \tag{17}$$

with

$$\boldsymbol{V}_{nP}(\hat{k}) = \int_{\mathrm{supp}(\boldsymbol{f}_n)} e^{-jk_0\hat{k}\cdot(\boldsymbol{r}-\boldsymbol{r}_P)} \left[\boldsymbol{s}_n(\boldsymbol{r}) \times \hat{k} \right] dS \quad \{\text{Disaggregation}\} \tag{18}$$

$$\boldsymbol{V}_{Qm}(\hat{k}) = \int_{\mathrm{supp}(\boldsymbol{f}_m)} e^{-jk_0\hat{k}\cdot(\boldsymbol{r}_Q-\boldsymbol{r}')} \boldsymbol{f}_m(\boldsymbol{r}') \, dS' \quad \{\text{Aggregation}\} \tag{19}$$

$$\tilde{\alpha}_{PQ}(\hat{k}) = \left(\frac{k_0}{4\pi} \right)^2 \sum_{l=0}^{L} (-j)^l (2l+1) h_l^{(2)}(k_0 r_{PQ}) P_l(\hat{k} \cdot \hat{r}_{PQ}) \quad \{\text{Translation}\} \tag{20}$$

$$\Delta_P^Q = \begin{cases} 1 & \text{For group } P \text{ fully visible to group } Q \\ 0 & \text{For group } P \text{ not fully visible to group } Q \end{cases} \tag{21}$$

where Δ_P^Q is the inter-group shadowing coefficient; $h_l^{(2)}(\cdot)$ is a spherical Hankel function of the second kind and $P_l(\cdot)$ is a Legendre polynomial. Due to the interaction criterion in (17), the representation is only valid for non-neighbour groups (i.e. groups of which the defining boxes do not touch). The practical details of choosing an appropriate number of poles L to include in the translation function $\tilde{\alpha}_{PQ}(\hat{k})$ and choosing an appropriate spherical quadrature rule for integrating over the unit sphere in (17) is well documented in e.g. [3] and will not be repeated here.

In the multi-level version of the FMM, space is subdivided according to a hierarchical, octree scheme. At the leaf-level, the box size is set to $D = \lambda_0/4$. This is a standard choice when using RWG basis functions [3], in which case the average mesh size is typically

recommended to be in the range $\lambda_0/16$ to $\lambda_0/6$ [33]. One level up, the box size is set to $D = \lambda_0/2$ such that the union of eight leaf-level boxes constitutes a single box on the second level. This is repeated up to the top level. The box-size at the top level is the maximum possible, such that non-neighbouring interactions (far interactions) can still take place. Clearly, the larger the structure, the more the number of levels will be. The MLFMM interaction tree is build by starting at the top level and working down to the leaf level, i.e. interactions are calculated on the highest possible level, as allowed by the interaction criterion. Neglecting shadowing for the moment, this means that all non-neighbours will interact on the top level. Top-level neighbour groups are subsequently considered in terms of their constituent groups at one level down. Among these, all valid interactions (according to the interaction criterion at that level) are again treated at that level, while the rest is handled down-level in exactly the same manner. This continues down to leaf-level. Finally, interactions between leaf-level neighbours are treated conventionally, using (14) directly.

To incorporate shadowing into the MLFMM procedure, the interaction criterion must be modified. Define a shadowing status flag between groups P and Q on a given level, as follows:

$$\oslash_P^Q = \begin{cases} \text{'Fully visible'} & \text{All members of } P \text{ can see all members of } Q; \\ \text{'Partially visible'} & \text{Some members of } P \text{ can see some/all members of } Q, \text{ or vice-a-versa;} \\ \text{'Fully shadowed'} & \text{No member of } P \text{ can see any members of } Q. \end{cases} \tag{22}$$

The shadowing status flag is the fundamental indicator. From it follows the value of the inter-group shadowing coefficient and the nature of the interaction between the two groups, according to this modified interaction criterion:

Let D_g denote the box size on level g.

IF ($r_{PQ} \geqslant 2D_g$ **and** $\oslash_P^Q =$ 'Fully visible') THEN
    Treat the interaction on level g with $\Delta_P^Q = 1$;

ELSE IF ($r_{PQ} \geqslant 2D_g$ **and** $\oslash_P^Q =$ 'Fully shadowed') THEN
    Treat the interaction on level g with $\Delta_P^Q = 0$;

ELSE IF ($r_{PQ} < 2D_g$ **or** $\oslash_P^Q =$ 'Partially visible') THEN
    Set $\Delta_P^Q = 0$ and repeat this test for all interactions between the two sets of level $(g-1)$ child-groups;

END IF. (23)

For $\Delta_P^Q = 0$ on leaf-level, the interaction is always regarded as zero. Thus, together with this altered criterion, shadowing is taken into account via the translation function as $\Delta_P^Q \, \tilde{\alpha}_{PQ}(\hat{k})$. If the two groups are fully visible to each other, translation is invoked. If there is partial visibility, the interaction is treated down-level in order that the partiality may be resolved. In the fully-shadowed case, no translation or further down-level checking is required.

The MLFMM interaction tree based on (23) will clearly incorporate some down-level interactions, which would have been treated at a higher level, had shadowing not

played a part. This happens at shadow boundaries where partial inter-group visibility exists. The extent of deviation from the conventional, optimal MLFMM interaction tree will thus depend on the geometry. For PO-suitable geometries, it is expected that this deviation will not have a significant impact upon efficiency. This point will be revisited later.

Getting back to the recursive MRPO expression (13): The matrix $[\boldsymbol{C}]$ is split up into a sparse near-interaction matrix relating to neighbouring groups on leaf-level, and the remaining far-interaction part; the latter is represented in factorized format via the MLFMM (aggregation, translation-with-shadowing and disaggregation factors). Equation (13) can thus be rewritten as

$$\{\boldsymbol{I}_{(K)}\} = \{\boldsymbol{I}_{(1)}\} + \left([\boldsymbol{C}_{\text{near}}] + [\boldsymbol{C}_{\text{far}}]\right)\{\boldsymbol{I}_{(K-1)}\}. \tag{24}$$

In the most general case of surfaces with currents modelled independently on both sides (16), the MLFMM-based representation becomes

$$\begin{Bmatrix} \boldsymbol{I}^{\text{n}}_{(K)} \\ \boldsymbol{I}^{\text{p}}_{(K)} \end{Bmatrix} = \begin{Bmatrix} \boldsymbol{I}^{\text{n}}_{(1)} \\ \boldsymbol{I}^{\text{p}}_{(1)} \end{Bmatrix} + \left(\begin{bmatrix} \boldsymbol{C}^{\text{nn}}_{\text{near}} & \boldsymbol{C}^{\text{np}}_{\text{near}} \\ \boldsymbol{C}^{\text{pn}}_{\text{near}} & \boldsymbol{C}^{\text{pp}}_{\text{near}} \end{bmatrix} + \begin{bmatrix} \boldsymbol{C}^{\text{nn}}_{\text{far}} & \boldsymbol{C}^{\text{np}}_{\text{far}} \\ \boldsymbol{C}^{\text{pn}}_{\text{far}} & \boldsymbol{C}^{\text{pp}}_{\text{far}} \end{bmatrix} \right) \begin{Bmatrix} \boldsymbol{I}^{\text{n}}_{(K-1)} \\ \boldsymbol{I}^{\text{p}}_{(K-1)} \end{Bmatrix}. \tag{25}$$

In each MLFMM box there will be two independent groups of basis functions: those on the positive sides and those on the negative sides (plural, since a group may contain disconnected geometry parts). Therefore, on a given level there will be four shadowing status flags relating to boxes $\boldsymbol{P}$ and $\boldsymbol{Q}$: $\oslash^{Q,\text{n}}_{P,\text{n}}$, $\oslash^{Q,\text{p}}_{P,\text{n}}$, $\oslash^{Q,\text{n}}_{P,\text{p}}$ and $\oslash^{Q,\text{p}}_{P,\text{p}}$. In (25) the MLFMM interaction tree and matrix factorization is thus constructed *independently* for each sub-matrix ('nn', 'np', 'pn' and 'pp'), according to the procedure described above, since each sub-matrix relates to the interaction of different sets of currents, each with its own shadowing data.

3.2. Procedure for determining the inter-group shadowing data

This section presents an efficient algorithm to determine the shadowing status flag $\oslash^{Q}_{P}$, for two groups $\boldsymbol{P}$ and $\boldsymbol{Q}$ on any given MLFMM level. This is for the case of currents on the outside of solid object(s) (i.e. formulation (24)), with outward pointing normals denoted as $\hat{\boldsymbol{n}}_P$ and $\hat{\boldsymbol{n}}_Q$ in the two groups. For the general, open-surface formulation (25), the algorithm is exactly the same, except to consider each of the four possible combinations $\{-\hat{\boldsymbol{n}}_P, -\hat{\boldsymbol{n}}_Q\}$, $\{-\hat{\boldsymbol{n}}_P, \hat{\boldsymbol{n}}_Q\}$, $\{\hat{\boldsymbol{n}}_P, -\hat{\boldsymbol{n}}_Q\}$ and $\{\hat{\boldsymbol{n}}_P, \hat{\boldsymbol{n}}_Q\}$ in turn, to yield the four results $\oslash^{Q,\text{n}}_{P,\text{n}}$, $\oslash^{Q,\text{p}}_{P,\text{n}}$, $\oslash^{Q,\text{n}}_{P,\text{p}}$ and $\oslash^{Q,\text{p}}_{P,\text{p}}$ required in that case.

Subsections 3.2.1, 3.2.2, 3.2.3 and 3.2.4 describe auxiliary data structures and methods which are required in the algorithm. Subsection 3.2.5 describes a single-ray, inter-group shadowing test. The latter test is the basis for the final algorithm, which is described in Subsection 3.2.6.

3.2.1. Mesh pre-processing

For each group on every level, calculate the average geometric location and bounding box of the set of edge-midpoints associated with the RWG basis functions belonging to the group. Define the following notation:

$$\boldsymbol{r}_{\overline{P}} \quad \{\text{Average midpoint location of basis function edges in group } \boldsymbol{P}\}. \tag{26}$$

For each group on every level, compile a list of all mesh elements (triangles) which collectively form the support of the basis functions belonging to the group. Furthermore,

determine the number of simple, physical surfaces formed by these mesh elements. The latter can be achieved efficiently by using mesh connectivity data to "grow" surface(s) among this set of elements, which practically amounts to choosing a starting triangle, then searching for its known neighbours in the group list, then neighbours' neighbours and so forth. The process is restarted until all elements in the group are accounted for as part of one or more surfaces. When a junction is encountered, it is recorded that the group is not constituted by a set of simple surfaces.

3.2.2. 3D buffer construction

A spatial index of element locations will be required for fast determination of elements located in certain regions. This spatial index is referred to as the *3D buffer*. It is based on subdividing the problem domain into a uniform grid of conformal cubes: the 3D buffer boxes. For each buffer box, a list is created of all mesh elements intersecting with it or touching it. In practice, this is achieved to satisfactory accuracy by considering 15 equally spaced sampling points on each element. The element number is added to all of the buffer box lists, corresponding to the buffer boxes within which any of these points fall. Figure 2 visualizes this process.

Denote the side-length of the 3D buffer boxes by D_{3D}. This is a free parameter. Smaller values give finer spatial resolution which is useful to reduce elemental shadowing checks (as will be seen later-on), but it also results in more boxes to be processed when considering a fixed volume of interest and it implies larger storage requirements (since a given element will be listed in more boxes). Setting D_{3D} roughly equal to the average mesh size was found to be an optimal choice. As will be seen in the next section, it is also convenient from an implementation point-of-view that the leaf-level MLFMM box size is a multiple of D_{3D}, with coincident boundaries (see Section 3.1 for mesh size and MLFMM box size details). Therefore, the 3D buffer box size is chosen to be $D_{3D} = \lambda_0/8$ — half the size of the MLFMM leaf-level boxes.

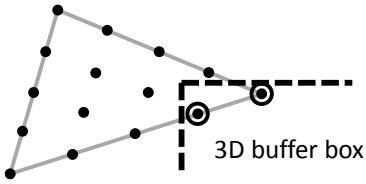

Figure 2: Method of detecting intersection between a triangle and a 3D buffer box.

3.2.3. Procedure to find non-empty 3D buffer boxes between two groups

Start by making a list of all non-empty MLFMM boxes on the same level as groups P and Q (level g, with box dimension D_g), which fall within the bounding box around these two groups. Next, reduce this list by excluding those boxes that cold not possibly intersect with the line-of-sight space between the two groups under consideration. This is done using a criterion based on calculating the shortest distance between the line connecting the average centroids of the two groups, and the centroid of each non-empty MLFMM box, as follows:

$$\begin{array}{l}\text{IF } \left(\left\| [\boldsymbol{r}_{\text{group}} - \boldsymbol{r}_{\overline{P}}] - ([\boldsymbol{r}_{\text{group}} - \boldsymbol{r}_{\overline{P}}] \cdot \hat{r}_{\overline{P}\,\overline{Q}})\hat{r}_{\overline{P}\,\overline{Q}} \right\| \leqslant \sqrt{3} D_g \right) \text{ THEN} \\ \quad \text{Include this MLFMM box in the reduced list;} \\ \text{END IF}\end{array} \tag{27}$$

where $\boldsymbol{r}_{\text{group}}$ denotes the centroid of the non-empty MLFMM box under consideration.

Now project the two bounding boxes of the edge-midpoints (see Section 3.2.1) in groups P and Q, onto the three global, Cartesian coordinate planes (xy, yz and zx). Also project the centroids of non-empty, 3D buffer boxes belonging to the above-identified list of MLFMM boxes. These projections are extremely fast, since all locations are known from the outset in the global Cartesian coordinate system. In each of the projection planes, flag the 3D buffer boxes which could possibly touch or intersect with the projected bounding tube of groups P and G. If a 3D buffer box is flagged in all three projections, then it is regarded as being in between the two groups — Figure 3 illustrates some aspects of this procedure. Figure 4 shows practical examples of inter-group geometry identification.

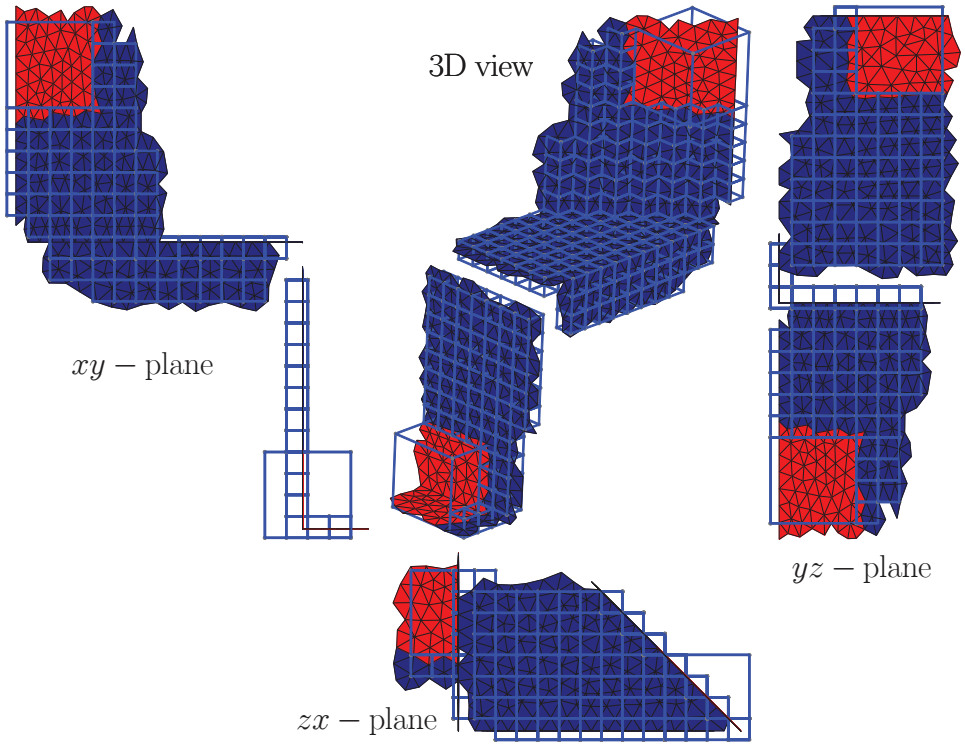

Figure 3: Identification of non-empty 3D buffer boxes between two groups. The bounding boxes around the associated edge-midpoints in each group, are shown, as well as all mesh elements. The non-empty 3D buffer boxes in between are shown, which are identified through projections onto the three global coordinate planes, as also shown.

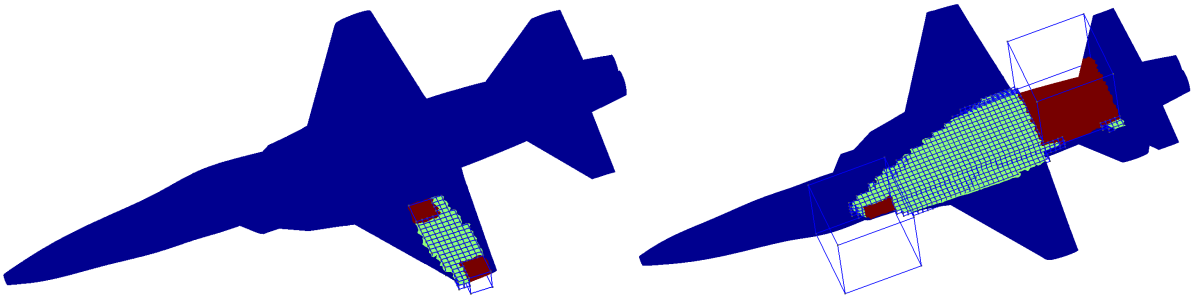

Figure 4: Practical examples of inter-group geometry identification, for an aircraft model. Left: at a low MLFMM level. Right: at a high MLFMM level.

3.2.4. Procedure to find the obstruction status of an inter-group ray

It will be necessary to direct a ray from $\boldsymbol{r}_{\overline{P}}$ to $\boldsymbol{r}_{\overline{Q}}$ and test if it intersects with any triangle from the rest of the geometry (i.e. elements not associated with groups $\boldsymbol{P}$ and $\boldsymbol{Q}$). This is done efficiently by identifying the minimum set of non-empty 3D buffer boxes which are possibly intersecting with or touching the ray path; then test the ray against all triangles in those box-lists.

To find this minimum set, first use the procedure from Section 3.2.3 to identify all inter-group, non-empty 3D buffer boxes. Figure 5 shows an example to illustrate this set. The shortest distance between the inter-group ray and the centroid of each non-empty box is calculated. If this distance is found to be such that the box could possibly intersect with or touch the ray, then it is added to the minimum set for elemental testing. This criterion can be quantified as

$$\begin{array}{l}\text{IF } \left(\left\| [\boldsymbol{r}_{3\mathrm{D}} - \boldsymbol{r}_{\overline{P}}] - ([\boldsymbol{r}_{3\mathrm{D}} - \boldsymbol{r}_{\overline{P}}] \cdot \hat{r}_{\overline{P}\,\overline{Q}})\hat{r}_{\overline{P}\,\overline{Q}} \right\| \leqslant \frac{\sqrt{3}}{2} D_{3\mathrm{D}} \right) \text{ THEN} \\ \qquad \text{Include this 3D buffer box in the minumum set;} \\ \text{END IF}\end{array} \tag{28}$$

where $\boldsymbol{r}_{3\mathrm{D}}$ denotes the 3D buffer box centroid; an example of this testing distance is shown in Figure 5.

Next, the ray is tested against the identified set of triangles. As soon as an intersection is detected, the test is terminated and the status is known as obstructed. If no intersection is detected, the status is open. The intersection test between a ray and a triangle is illustrated in Figure 6. A local Cartesian coordinate system is created with the n-axis along the ray path. The triangle is projected onto the uv-plane and if it encircles the origin, then intersecting takes place.

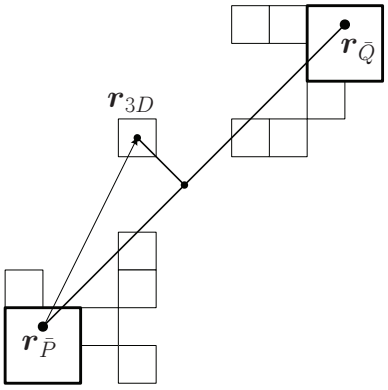

Figure 5: Testing to see if a 3D buffer box could possibly intersect with an inter-group ray. All non-empty, inter-group 3D buffer boxes are shown.

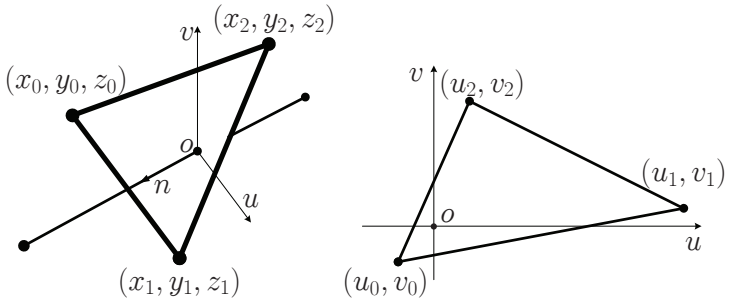

Figure 6: Intersection test for a ray with a triangle. Local coordinate n points along the ray path. After projection of the triangle into the uv-plane, testing whether the origin is inside that projection is very fast. Calculate $a_0 = u_0v_1 - u_1v_0$, $a_1 = u_1v_2 - u_2v_1$ and $a_2 = u_2v_0 - u_0v_2$. If a_0, a_1 and a_2 all have the same sign, then the ray intersects with the triangle.

3.2.5. The single-ray, inter-group shadowing status flag test

This test estimates the shadowing status flag $\oslash_P^Q$. It is approximate in nature, meaning that incorrect assessments can occur. Hence, the result with this test will be denoted by $\widetilde{\oslash}_P^Q$. Determining the actual shadowing status flags and error-control, will be discussed in Section 3.2.6.

Figure 7 shows a flowchart describing the procedure. Start by testing if the currents in the two groups face each other (orientation check). If they are only partially facing each other, the status can either be 'Fully shadowed' or 'Partially visible', a choice which is determined by approximation, through the obstruction status of the single inter-group ray, as described in Section 3.2.4. If the groups do fully face each other, then the single-ray result is used to determine full shadowing. If they are facing each other and the single ray is unobstructed, then for each group, test for self-shadowing. If no self-shadowing is found at this point, then the result is 'Fully visible', otherwise it is 'Partially visible'. Further details on the orientation and self-shadowing checks are provided below.

Orientation check. As shown in Figure 1, an outward-pointing (i.e. away from the PEC volume) normal vector is associated with each basis function. The orientation check involves forming the dot-product of $\hat{r}_{\overline{P}\,\overline{Q}}$ with all of the basis function normal vectors in each group. Figure 8 describes this test. The result can be that all of the functions in group P are facing towards all of the functions in group Q, which is a pre-requisite for the 'Fully visible' status. It can also be that some but not all, face toward each other, in which case the status can at most be 'Partially visible'. In case one of the groups face completely away from the other, the status is immediately known as 'Fully shadowed'.

Self-shadowing check. This check is only conducted when it is already known that the two groups face each other completely. If a group also consists of a single, simple surface, then no self-shadowing is possible for that group. If a group consists of multiple simple surfaces, then further testing is required, as these surfaces may obscure each other within the group. Figure 9 illustrates such scenarios. To test for self-shadowing within a group, project all of the elements associated with that group onto a plane perpendicular to the direction $\hat{r}_{\overline{P}\,\overline{Q}}$. Then project all of the group's basis function edge-midpoints onto the same plane. If any of these points project into the interior or onto the edge of any triangle other than the two which form the support of the associated basis function, then self-shadowing does occur for that group and thus it will only be partially visible. It is important to do this test with optimal efficiency. This is achieved by using the field-of-view buffer algorithm discussed in [34], which ensures that the cost is directly

proportional to the number of elements in the group. Figure 10 shows projection plane examples with and without self-shadowing.

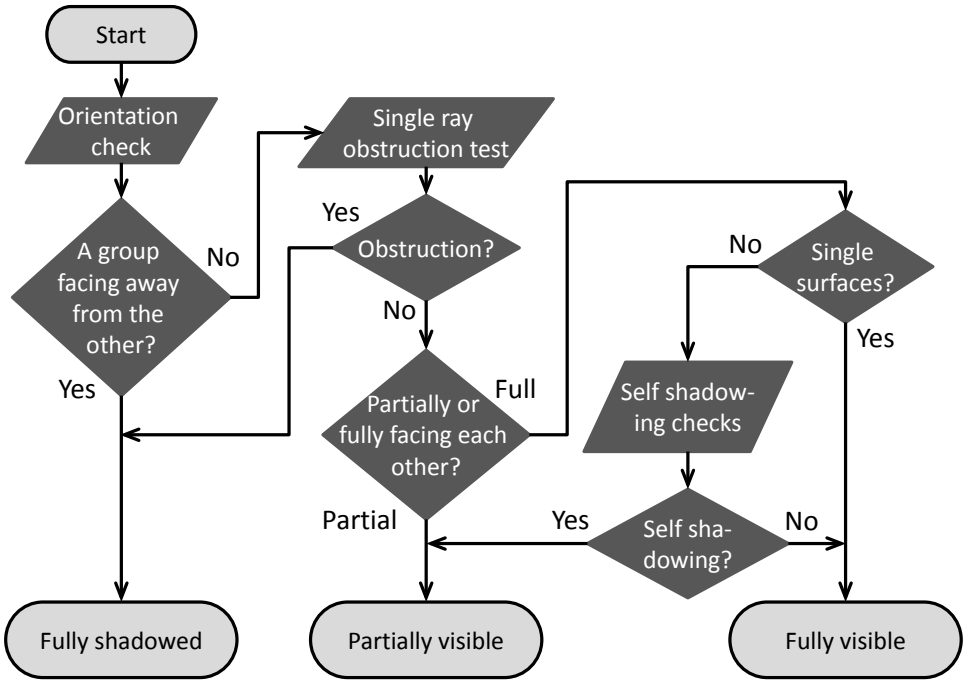

Figure 7: Flowchart describing the single-ray, inter-group shadowing status test, which yields the approximate shadowing status flag $\tilde{\oslash}_P^Q$.

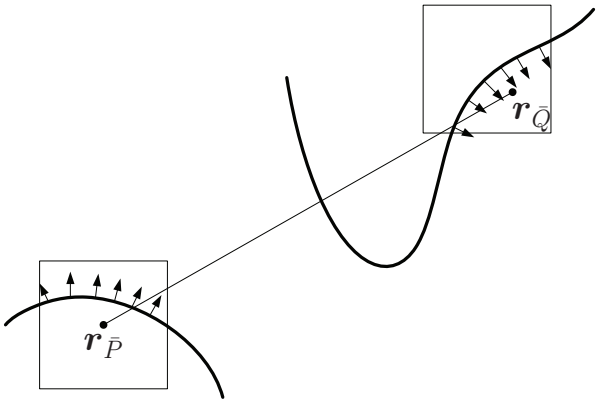

Figure 8: Orientation checking.

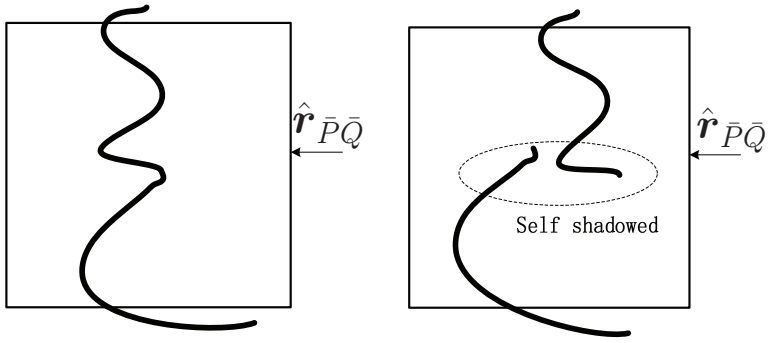

Figure 9: Self shadowing internal to a group. Left: for a simple surface facing the other group, no self shadowing is possible. Right: for multiple simple surfaces all facing the other group, self shadowing is possible.

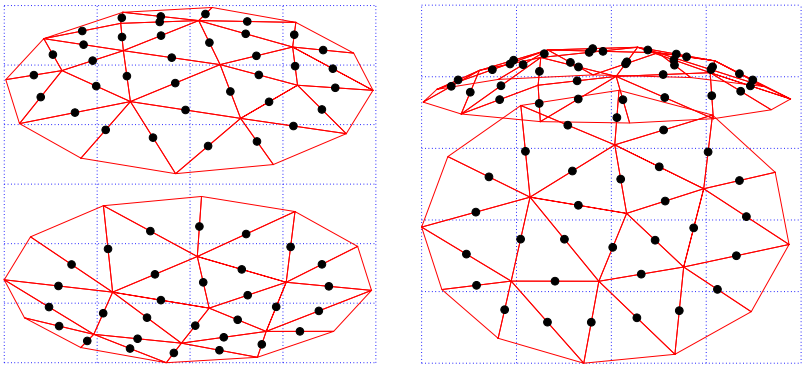

Figure 10: Buffer plane projection for self-shadowing testing within a group with multiple simple surfaces. Left: no self shadowing in the group. Right: self shadowing occurring due to overlapping surfaces.

3.2.6. Final procedure for determining all shadowing status flags

Rigorously evaluating the inter-group shadowing status flags $\oslash_P^Q$ by determining the shadowing status of all rays between each basis function edge-midpoint in group $\boldsymbol{P}$ and each one in group $\boldsymbol{Q}$, would be prohibitively expensive. Hence the approximate, single-ray, inter-group shadowing status flag test from Section 3.2.5 was devised. The final procedure for determining all shadowing status flags makes use of multiple evaluations of this approximate test, such that shadowing determination errors are controlled, while avoiding unnecessary work, given the fundamentally approximate nature of the PO approximation itself. It involves three key parameters:

$$g_{\text{depth}} \quad \{\text{Depth of down-level shadowing status flag evaluation}\} \tag{29}$$

$$\boldsymbol{D}_{\text{single}} \quad \{\text{Maximum MLFMM box size for single-ray testing}\} \tag{30}$$

$$\boldsymbol{D}_{\text{binary}} \quad \{\text{Maximum MLFMM box size for ignoring partial visibility}\}. \tag{31}$$

where MLFMM box sizes $\boldsymbol{D}_{\text{single}}$ and $\boldsymbol{D}_{\text{binary}}$ correspond to levels g_{single} and g_{binary}, respectively.

Through the parameter g_{depth}, the accuracy of the status determination is controlled. To determine $\oslash_P^Q$ on level g, the shadowing status flags between all sub-groups of group $\boldsymbol{P}$ and all sub-groups of group $\boldsymbol{Q}$, both at level $(g - g_{\text{depth}})$ are first determined according to the single-ray, inter-group shadowing status flag test. Let the two sets of sub-groups

on level $(g - g_{\text{depth}})$ be denoted by $\{P(1), ..., P(p)\}$ and $\{Q(1), ..., Q(q)\}$. The testing then yields the following set of flags:

$$\bigcup_{\alpha=1}^{p} \left\{ \bigcup_{\beta=1}^{q} \left\{ \widetilde{\oslash}_{P(\alpha)}^{Q(\beta)} \right\} \right\}. \tag{32}$$

If all of these indicate 'Fully visible', then $\oslash_P^Q$ = 'Fully visible'. If all of these indicate 'Fully shadowed', then $\oslash_P^Q$ = 'Fully shadowed'. Otherwise, $\oslash_P^Q$ = 'Partially visible'. Figure 11 illustrates this concept. To accelerate the implementation, all non-empty 3D buffer boxes between groups P and Q should be determined first and all other geometry excluded from further consideration for the ray tests. Clearly, the larger g_{depth}, the more accurate the status flag will be. In the limit, the testing is done at leaf-level, which is practically equivalent to individual basis function-based evaluation. Of course, the larger g_{depth} is, the more expensive the test becomes.

Through the parameter D_{single}, the effort put into shadowing determination at lower levels is reduced. This is done, because the inter-group ray-paths being tested in (32) become increasingly similar at lower levels, as the groups' defining box-sizes become smaller and smaller. Thus, for all levels $g \leqslant g_{\text{single}}$, down-level testing is not performed. Rather, only a single-ray shadowing status test is done, as follows:

$$\oslash_P^Q = \widetilde{\oslash}_P^Q \quad \{D_g \leqslant D_{\text{single}}\}. \tag{33}$$

This implies that the number of levels down, at which shadowing is checked in (32), must be adjusted to be $\min(g_{\text{depth}}, g - g_{\text{single}})$ for $g > g_{\text{single}}$.

Through the parameter D_{binary}, partial visibility and consequent down-level interaction is not considered at lower levels, by forcing binary status flag values in the following way:

$$\begin{array}{lcll} \widetilde{\oslash}_P^Q = \text{'Fully visible'} & \rightarrow & \oslash_P^Q = \text{'Fully visible'} & \\ \widetilde{\oslash}_P^Q = \text{'Partially visible'} & \rightarrow & \oslash_P^Q = \text{'Fully shadowed'} & \{D_g \leqslant D_{\text{binary}}\}. \\ \widetilde{\oslash}_P^Q = \text{'Fully shadowed'} & \rightarrow & \oslash_P^Q = \text{'Fully shadowed'} & \end{array} \tag{34}$$

Clearly, the box-size parameters will cause some shadow boundary shift errors of around $\lesssim D_{\text{single}}/2$ and $\leqslant D_{\text{binary}}$ in cast shadows and at corners. When the geometry is much larger than this, these errors can be assumed negligible, especially in light of the approximate nature of the PO approximation itself.

Through these parameters, accuracy of shadowing determination is fully controllable and in the results section, the effect of these parameters upon accuracy is experimentally investigated. The following values are recommended for PO-suitable geometries in general:

$$g_{\text{depth}} = 1 \tag{35}$$

$$D_{\text{single}} = \lambda_0 \tag{36}$$

$$D_{\text{binary}} = \lambda_0. \tag{37}$$

The choice of $D_{\text{single}} = D_{\text{binary}} = \lambda_0$ strikes a good balance between accuracy and runtime efficiency for geometries at the lower end of PO-applicable electrical sizes. Of course, this may be changed by the analyst depending on specialized conditions and

acceptable levels of approximation. For electrically very large scatterers, the values of D_{single} and D_{binary} can be increased.

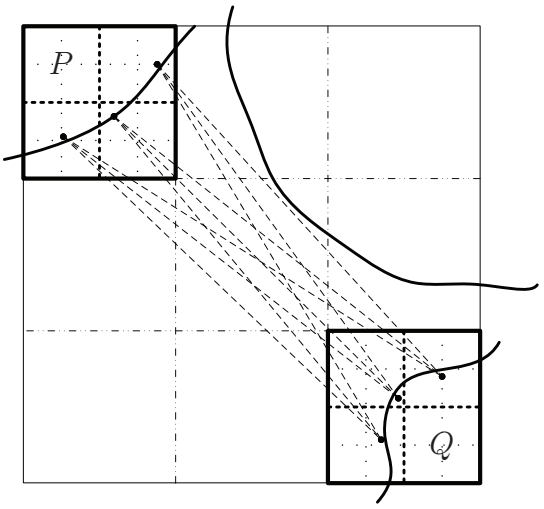

Figure 11: Illustration of the shadowing status checking procedure for determining $\oslash_P^Q$. In this example visualization, single-ray, inter-group, approximate shadowing status checks are done at one level down, i.e. $g_{\text{depth}} = 1$.

3.3. Computational cost of the FMRPO

Assume at first that the MLFMM interaction tree remains unchanged when incorporating shadowing information. This will be the case when the shadowing status flags always take on the values of 'Fully visible' or 'Fully shadowed'. As far as the computational cost of the MLFMM then goes (setting up factors, aggregation, translation and disaggregation), the cost will be $\mathcal{O}(N_{\text{T}} \log N_{\text{T}})$ for homogeneous meshes [3]. The cost related to shadowing determination must be added to this, which is of critical interest.

Start by noting that the number of MLFMM levels is $\mathcal{O}(\log N_{\text{T}})$. Since groups only interact with local (though non-neighbour) other groups on a given level, it follows that the number of inter-group interactions on a given level, is directly proportional to the number of groups on that level. Of course, only non-empty groups are dealt with. At the top level, the number of groups are $\mathcal{O}(1)$ and the number of mesh elements (as well as non-empty 3D buffer boxes) between two groups is $\mathcal{O}(N_{\text{T}})$. The cost of determining the number of non-empty 3D buffer boxes between two groups is clearly proportional to the total number, thus at the top level this cost will be $\mathcal{O}(N_{\text{T}})$. Since the number of rays to test for obstruction is fixed in the inter-group shadowing status flag determination method, it follows that its cost will be proportional to the number of non-empty 3D buffer boxes in between the groups, which is $\mathcal{O}(N_{\text{T}})$. The shadowing determination cost at the top level is thus $\mathcal{O}(N_{\text{T}})$. At the leaf level, the number of groups is $\mathcal{O}(N_{\text{T}})$, as well as the number of inter-group interactions. The cost of finding the non-empty 3D buffer boxes between two groups is now $\mathcal{O}(1)$, as the groups are close together. It follows that the cost of a single ray obstruction test is $\mathcal{O}(1)$ and thus, shadowing status determination on leaf-level is the same as on the top level, namely $\mathcal{O}(N_{\text{T}})$. This cost scales the same for all levels and thus the total shadowing status determination cost for the whole interaction tree will be $\mathcal{O}(N_{\text{T}} \log N_{\text{T}})$, which means that this is also the scaling of the method as a whole. Storage requirement scales the same. For future practical interest, the cost of finding non-empty 3D buffer boxes along ray paths at higher levels could be reduced by employing a comprehensive bounding volume hierarchy (BVH) strategy [35], which fits

well into the MLFMM octree setting. However, this will not change the overall scaling of the FMRPO, as the cost of setting up the data structures is already $\mathcal{O}(N_\mathrm{T} \log N_\mathrm{T})$.

Clearly, for practical geometries the MLFMM interaction tree will be altered via the modified criterion (23). The extent will depend upon the geometry. For large, smooth geometries with localized fine details, the departure from the original tree will not be extensive, whereas for the extreme case of geometrically random structures, the algorithm might well end up treating most interactions on leaf-level, or close to it. In the latter case the efficiency will deteriorate to the point that conventional MRPO would be preferable. However, since PO itself is not suitable for the latter type of geometries, it follows that for actual PO-suitable geometries the departure can be expected to not be significant and the time-scaling of the algorithm can be regarded as quasi-$\mathcal{O}(N_\mathrm{T} \log N_\mathrm{T})$. This is investigated for general geometries in the results section. The computer memory requirement scales the same.

Regarding the near-interaction matrix in (24) (or (25)): the cost of setting up, storing and multiplying with this matrix is $\mathcal{O}(N_\mathrm{T})$. Importantly, the near-interaction shadowing coefficients are calculated together for each near-interaction leaf-level pair of groups, by first identifying the mesh elements in between the groups and then only considering these, using conventional, SRPO-like shadowing testing.

4. Numerical results

Firstly, results are presented to verify the equivalence of the accelerated method and the conventional version. This is followed by results to investigate the effect of the algorithmic parameters g_{depth}, D_{single} and D_{binary} upon accuracy. Finally, the main results of the paper are presented, namely the runtime as a function of N_{T}, as well as some scattering and induced surface current results for electrically large geometries. Figure 12 shows the four test geometries, which include two practical scattering shapes (the ship and aircraft). Unless stated otherwise, the mesh-size is set at $\lambda_0/10$ throughout. Plane wave excitations are used throughout, at specified incident angles. All results were generated on a modest desktop computer with 16 GB memory.

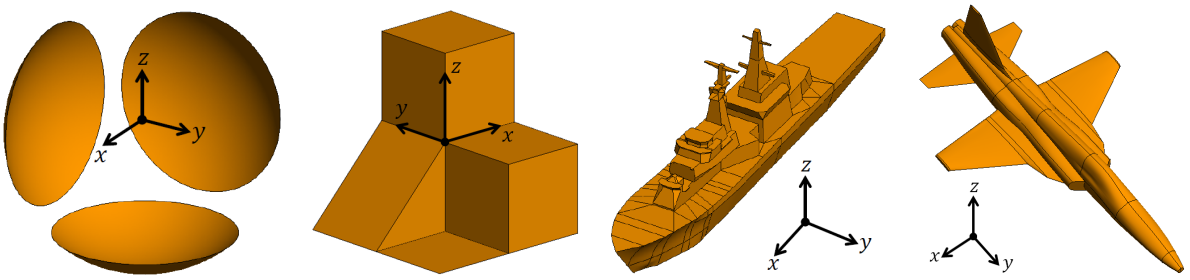

Figure 12: Models used in the results section, together with their global coordinate systems. From left to right: spherical trihedral, flat faceted surface, ship and aircraft.

4.1. Accuracy of the FMRPO

For all results in this section, the algorithmic parameters are set to their most accurate values, namely $g_{\text{depth}} = 1$ and $D_{\text{single}} = D_{\text{binary}} = \lambda_0/4$ (leaf-level). The depth is not set to a larger value, as it will shortly be shown that $g_{\text{depth}} = 1$ yields very accurate results.

First consider the spherical trihedral. This geometry is formed as the resulting surface after subtracting a cube from a sphere, such that three identical reflectors are obtained. When illuminated into the corner, it supports three significant reflections. In this structure all edges are visible to each other, thus the MLFMM interaction tree will be unchanged, with the shadowing status flag value in (23) always being 'Fully visible' — thus the shadowing determination algorithm plays no part in this case. Figure 13 compares the conventional MRPO with the accelerated version. This result shows that the MLFMM is indeed very suitable for internal field calculation in the MRPO, with a negligibly small difference in the results at a level typical of the MLFMM relative to conventional integration.

Next, consider two geometries which support significant internal shadowing. In such cases it can be expected that the group-based shadowing treatment will introduce a difference relative to the conventional MRPO, where shadowing is determined rigorously for every edge-pair. Figure 14 shows the results. It can be seen that errors only surface in low scattered field directions. It should be kept in mind that the electrical sizes of these test cases are quite small, due to the prohibitive cost of solving the conventional MRPO for electrically large geometries. Clearly, the relative error introduced by group-based shadowing with fixed algorithmic parameter values, will diminish as electrical size grows. Therefore, this can be viewed as "worst case scenario" results.

Collectively, the results in this section show that the accelerated formulation is indeed a true equivalent of the conventional MRPO.

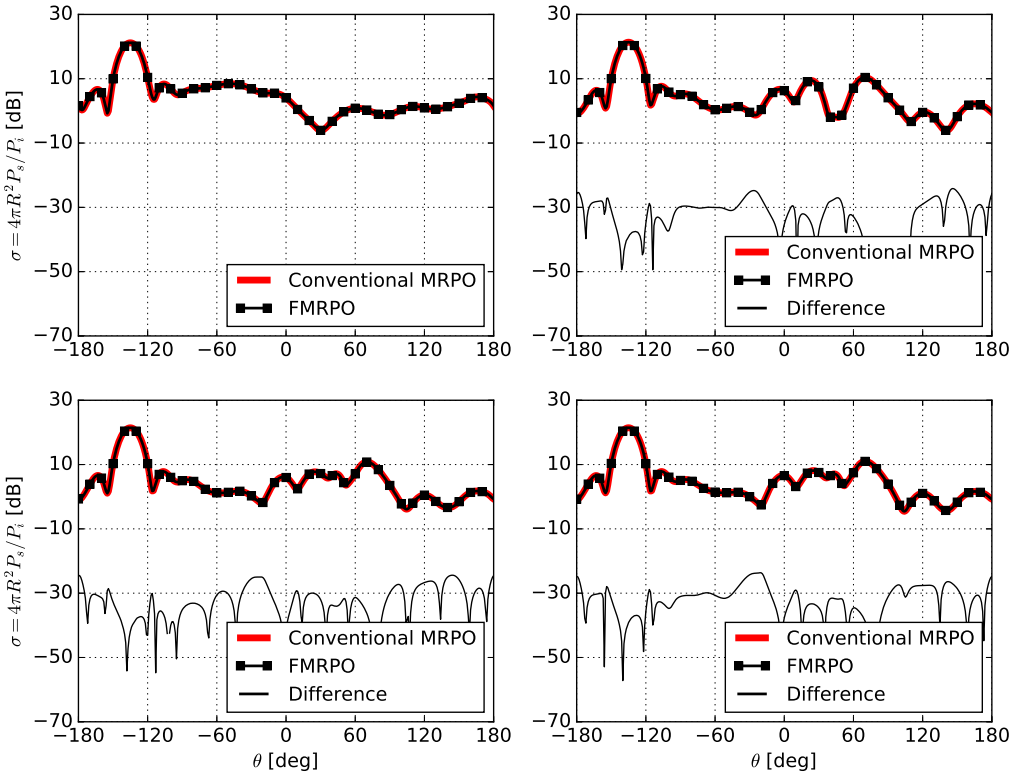

Figure 13: Bistatic RCS of the spherical trihedral at $\phi = 45°$, with $(\theta^{\text{inc}}, \phi^{\text{inc}}) = (45°, 45°)$ and aperture electrical size $5.5\lambda_0$. Comparison between conventional and accelerated MRPO formulations, for reflections from $K = 1$ to $K = 4$ (1 and 2 at the top, 3 and 4 at the bottom).

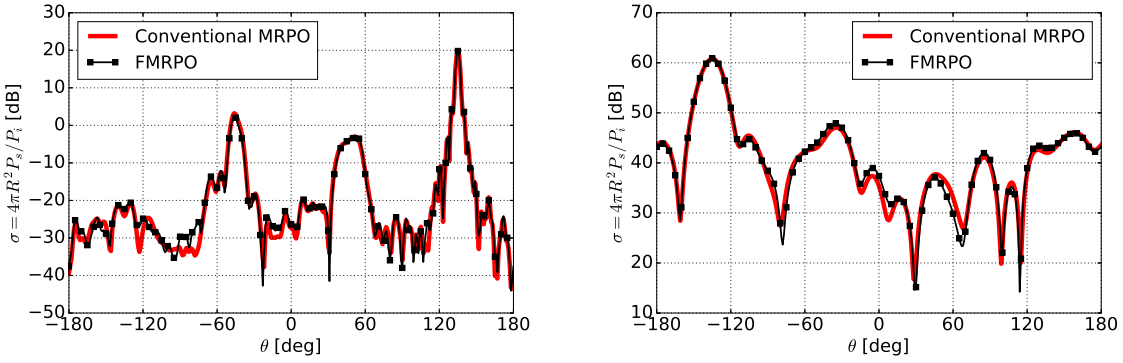

Figure 14: Comparison between conventional and accelerated MRPO formulations, of bistatic RCS for $K = 3$. Left: faceted surface at $\phi = 45°$, with $(\theta^{\text{inc}}, \phi^{\text{inc}}) = (45°, 225°)$ at electrical size $12\lambda_0$. Right: ship at $\phi = 90°$, with $(\theta^{\text{inc}}, \phi^{\text{inc}}) = (45°, 90°)$ and electrical size $18\lambda_0$.

4.2. Investigation of the algorithmic parameters g_{depth}, $\boldsymbol{D}_{\text{single}}$ *and* $\boldsymbol{D}_{\text{binary}}$

To investigate g_{depth}, set $\boldsymbol{D}_{\text{single}} = \boldsymbol{D}_{\text{binary}} = \lambda_0/4$ (leaf-level, for maximum accuracy). Figure 15 shows the results. The two complex realistic geometries were specifically chosen, since $g_{\text{depth}} = 0$ can yield error-free determination for simple test objects. Clearly, $g_{\text{depth}} = 1$ is a practically suitable choice, yielding very accurate results. For larger values, computational cost increases significantly, without adding any further value.

To investigate D_{single}, set $g_{\text{depth}} = 1$ (error-free for this model) and $D_{\text{binary}} = \lambda_0/4$ (leaf-level, for maximum accuracy). For this investigation the faceted surface is used, with $\lambda_0/8$ meshing. The electrical size (bounding box dimension) is set at $20\lambda_0$, thus individual facets are $10\lambda_0$ in size, with a number of sharp edges which will cause an influence when varying D_{single} — thus a reasonable, but not large, PO-suitable problem. Figure 16 shows the results. The accuracy deteriorates as D_{single} is increased.

To investigate D_{binary}, set $g_{\text{depth}} = 1$ and $D_{\text{single}} = \lambda_0/4$ (leaf-level, for maximum accuracy). The test setup is the same as for D_{single}. Figure 17 shows the results. Again, the accuracy deteriorates as the parameter value is increased.

Given the D_{single} and D_{binary} results, together with the facts that (i) relative error contributions due to these fixed parameters will diminish and rapidly become insignificant, as the electrical size of the geometry grows (which is exactly when PO is most applicable), and (ii) that these parameter values influence computational cost (though not the scaling properties), it is recommended to set these values to a dimension much smaller than the electrical size of the object being analyzed, but not necessarily at leaf-level. See the discussion at the end of Section 3.2.6.

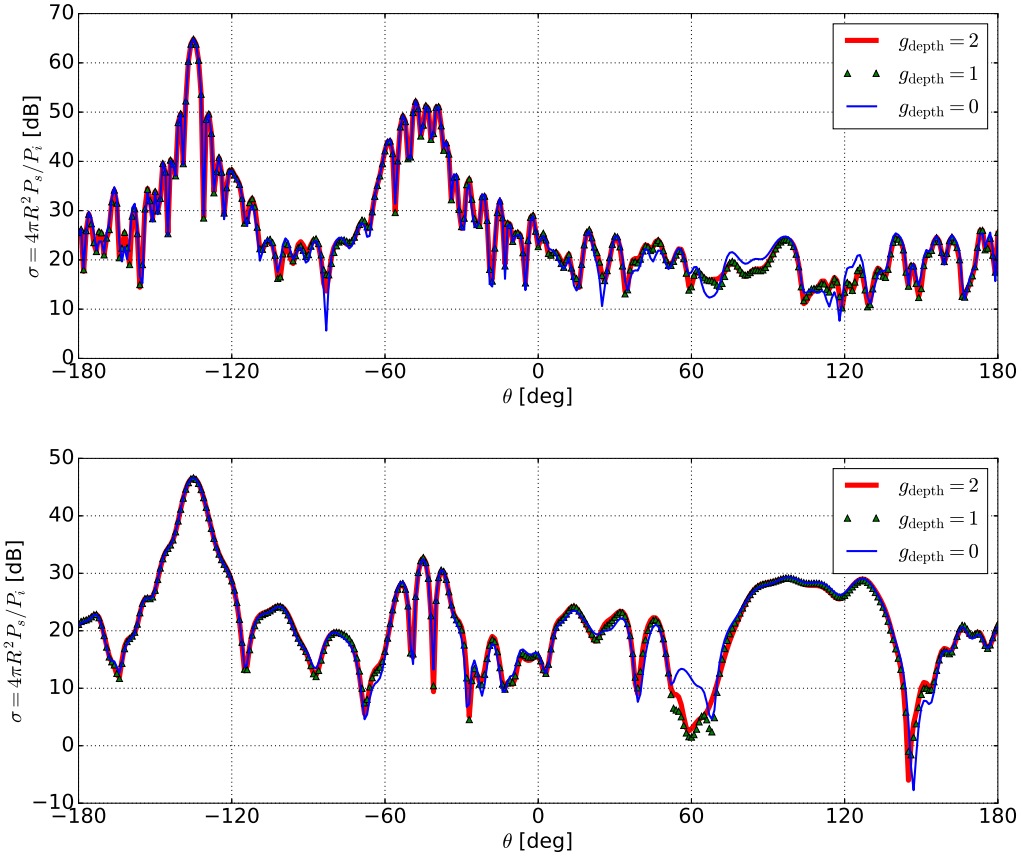

Figure 15: Investigation of g_{depth}, with $D_{\text{single}} = D_{\text{binary}} = \lambda_0/4$ (leaf-level). Bistatic RCS is shown for $K = 3$. Top: ship at $\phi = 90°$, with $(\theta^{\text{inc}}, \phi^{\text{inc}}) = (45°, 90°)$ and electrical size $32\lambda_0$. Bottom: aircraft at $\phi = 0°$, with $(\theta^{\text{inc}}, \phi^{\text{inc}}) = (45°, 0°)$ at electrical size $24\lambda_0$.

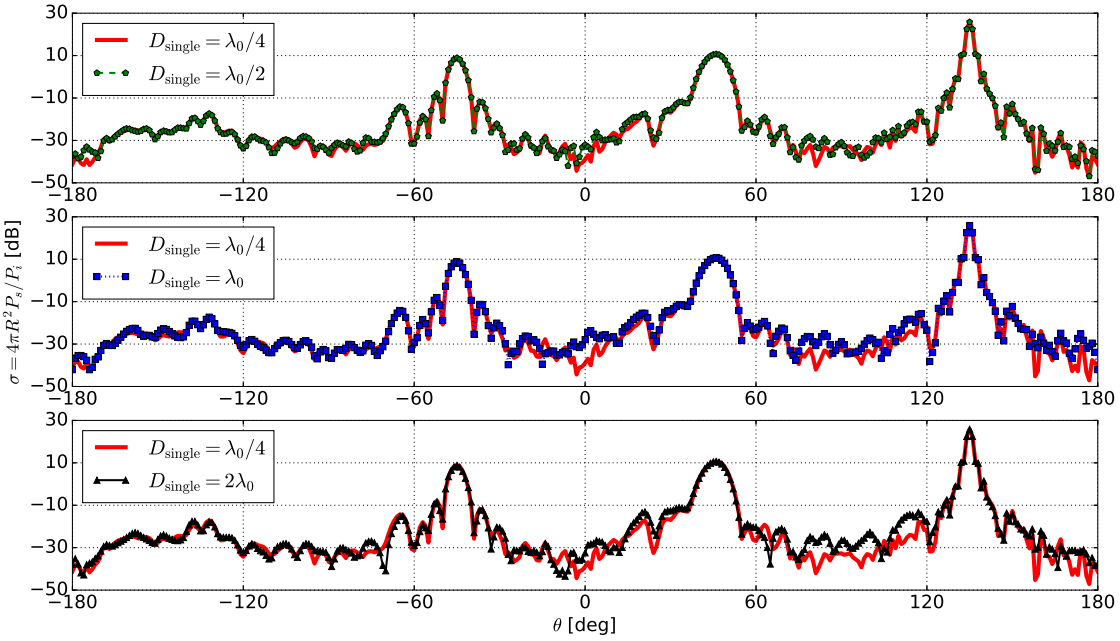

Figure 16: Investigation of D_{single}, with $g_{\text{depth}} = 1$ and $D_{\text{binary}} = \lambda_0/4$ (leaf-level). Bistatic RCS of the faceted surface is shown for $K = 3$ at $\phi = 45°$, with $(\theta^{\text{inc}}, \phi^{\text{inc}}) = (45°, 225°)$ and electrical size $20\lambda_0$.

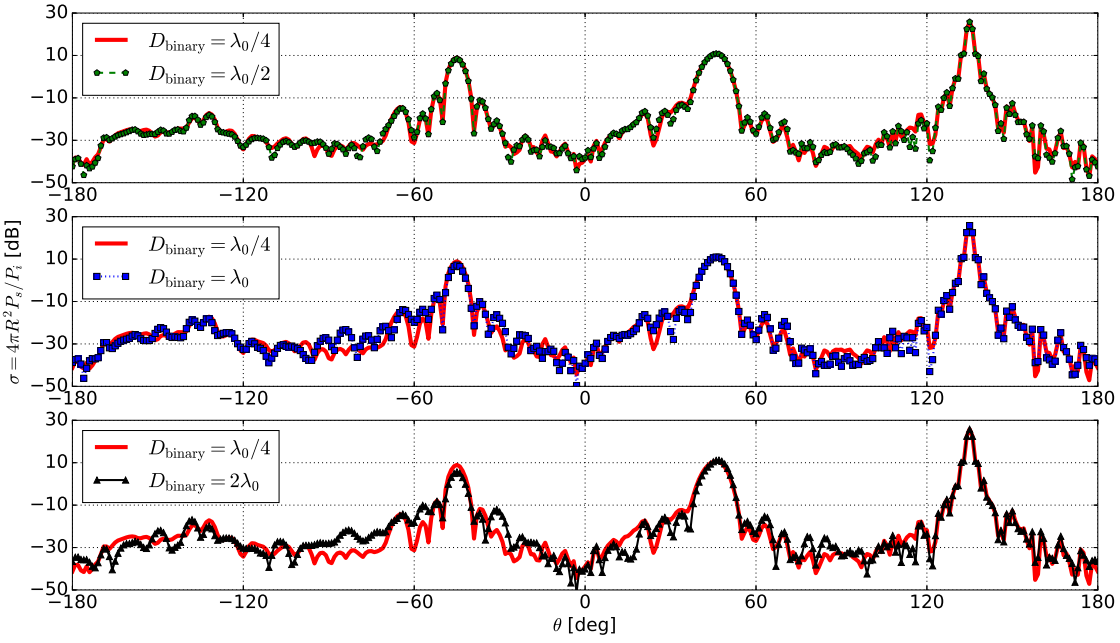

Figure 17: Investigation of D_{binary}, with $g_{\text{depth}} = 1$ and $D_{\text{single}} = \lambda_0/4$ (leaf-level). Bistatic RCS of the faceted surface is shown for $K = 3$ at $\phi = 45°$, with $(\theta^{\text{inc}}, \phi^{\text{inc}}) = (45°, 225°)$ and electrical size $20\lambda_0$.

4.3. Performance of the accelerated MPRO formulation

For all results in this section, the algorithmic shadowing parameters are set to the recommended values in (35), (36) and (37), i.e. $g_{\text{depth}} = 1$ and $D_{\text{single}} = D_{\text{binary}} = \lambda_0$. Figure 18 shows the main result of this paper, namely a comparison between the conventional and accelerated MRPO formulations, with regards to runtime as a function of N_{T}. These results were obtained by varying the excitation frequency and re-meshing

appropriately. Firstly, note that the conventional MRPO scales as $\mathcal{O}({N_\mathrm{T}}^2)$ in all cases. Considering the accelerated result for the spherical trihedral: it scales exactly as the MLFMM itself. This makes complete sense, as its interaction tree is exactly the same as it would be for the standard MLFMM. Considering the FMRPO results for the ship and aircraft, two aspects are apparent: (i) the time-scaling complexity in both cases is slightly higher than for the spherical trihedral and (ii) the scaling constant for the runtime is lower than for the spherical trihedral. The first aspect can be understood as a manifestation of the quasi-$\mathcal{O}(N_\mathrm{T} \log N_\mathrm{T})$ scaling property, due to internal shadowing which causes sub-optimal, down-level interactions to be incorporated into the MLFMM interaction tree. The second aspect can be understood by noting that no translation is calculated between fully shadowed groups. Thus, for the range of mesh sizes considered here, less translations are in fact calculated for the ship and aircraft, than for the spherical trihedral, at equal numbers of mesh elements.

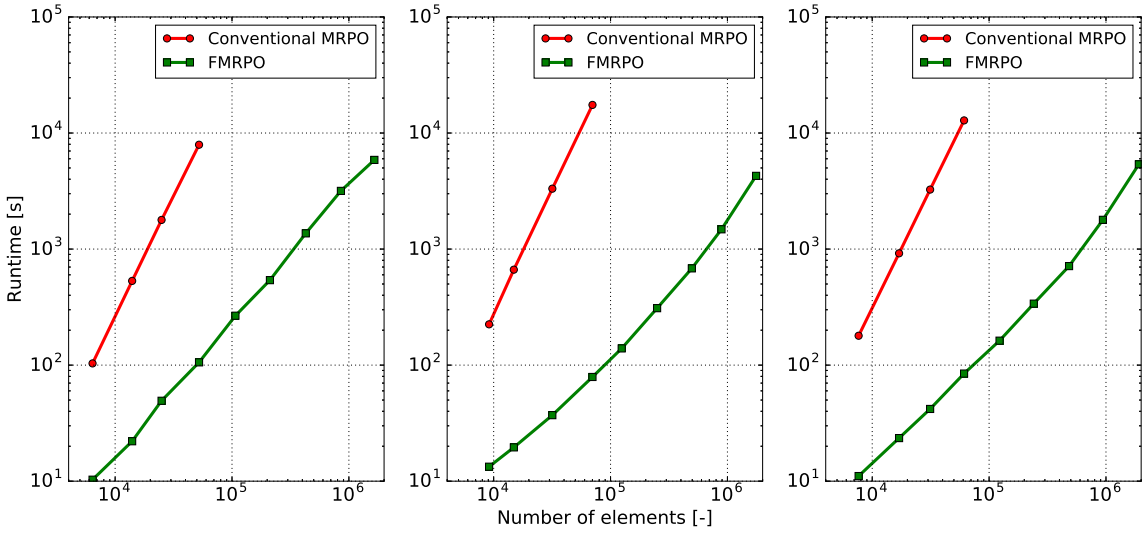

Figure 18: Runtime vs. number of mesh elements, for $K = 3$ and N_T up to almost 2×10^6. Left: spherical trihedral. Middle: ship. Right: aircraft.

Next, some practical results for electrically large scatterers are presented. Consider the spherical trihedral at $38.5\lambda_0$ aperture size. Figure 19 shows two scattered-field pattern cuts after including up to three reflections, compared to the MLFMM solution on the same mesh. Figure 20 shows the corresponding current distributions. The MRPO yields excellent results for this geometry which consists solely of electrically large, smooth surfaces. Lastly, consider the ship at $100\lambda_0$ electrical length. Figure 21 shows two scattered-field pattern cuts after including up to three reflections, compared to the MLFMM solution on the same mesh. Figure 22 shows the corresponding current distributions. In this case the main peaks are resolved well, and the dramatic positive effect that inclusion of higher-order reflections has, is evident. The correspondence with the full integral equation solution is not as good as for the spherical trihedral, because the ship has many sub-features of smaller electrical size, as well as many edges and corners where diffraction phenomena take place which are not accounted for in the standard MRPO.

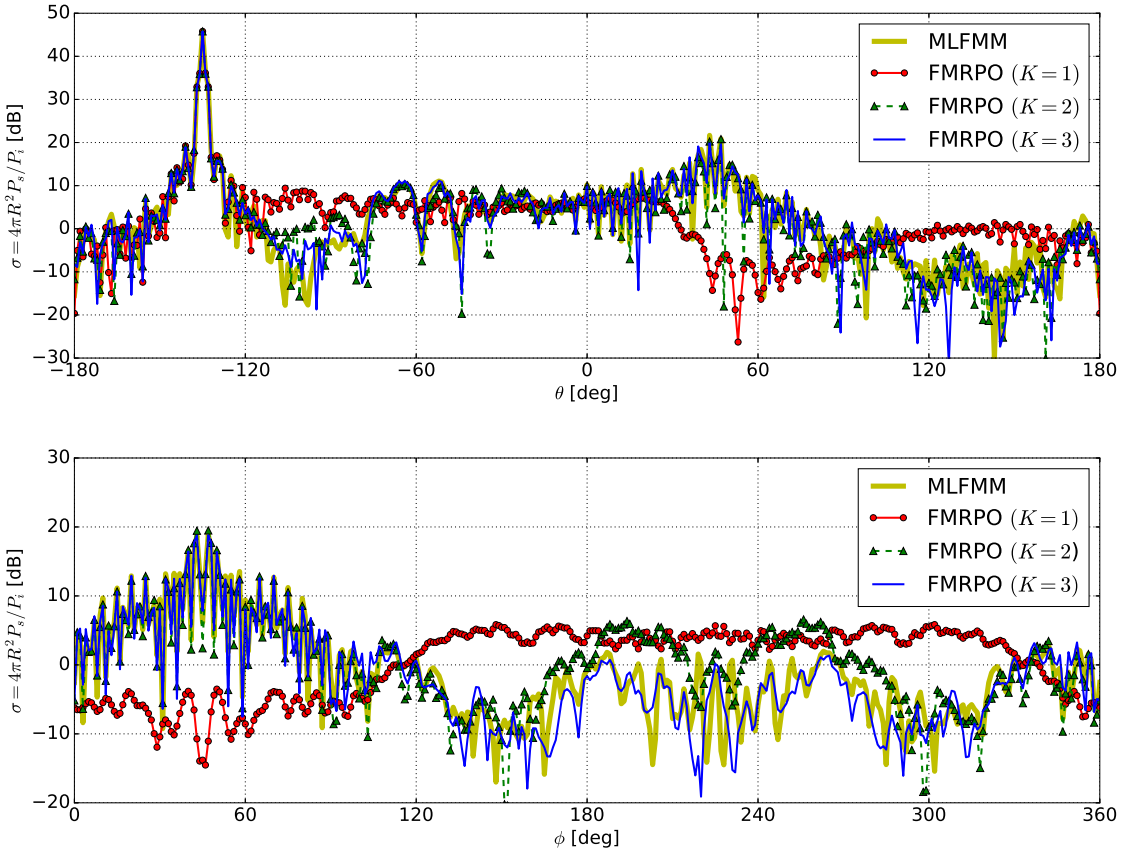

Figure 19: Bistatic RCS of the spherical trihedral with $(\theta^{\text{inc}}, \phi^{\text{inc}}) = (45°, 45°)$, at electrical size $38.5\lambda_0$ ($N_{\text{T}} = 593,104$). Comparison between results with $K = 1$ to $K = 3$ and the MLFMM solution. Top: pattern cut at $\phi = 45°$. Bottom: pattern cut at $\theta = 45°$.

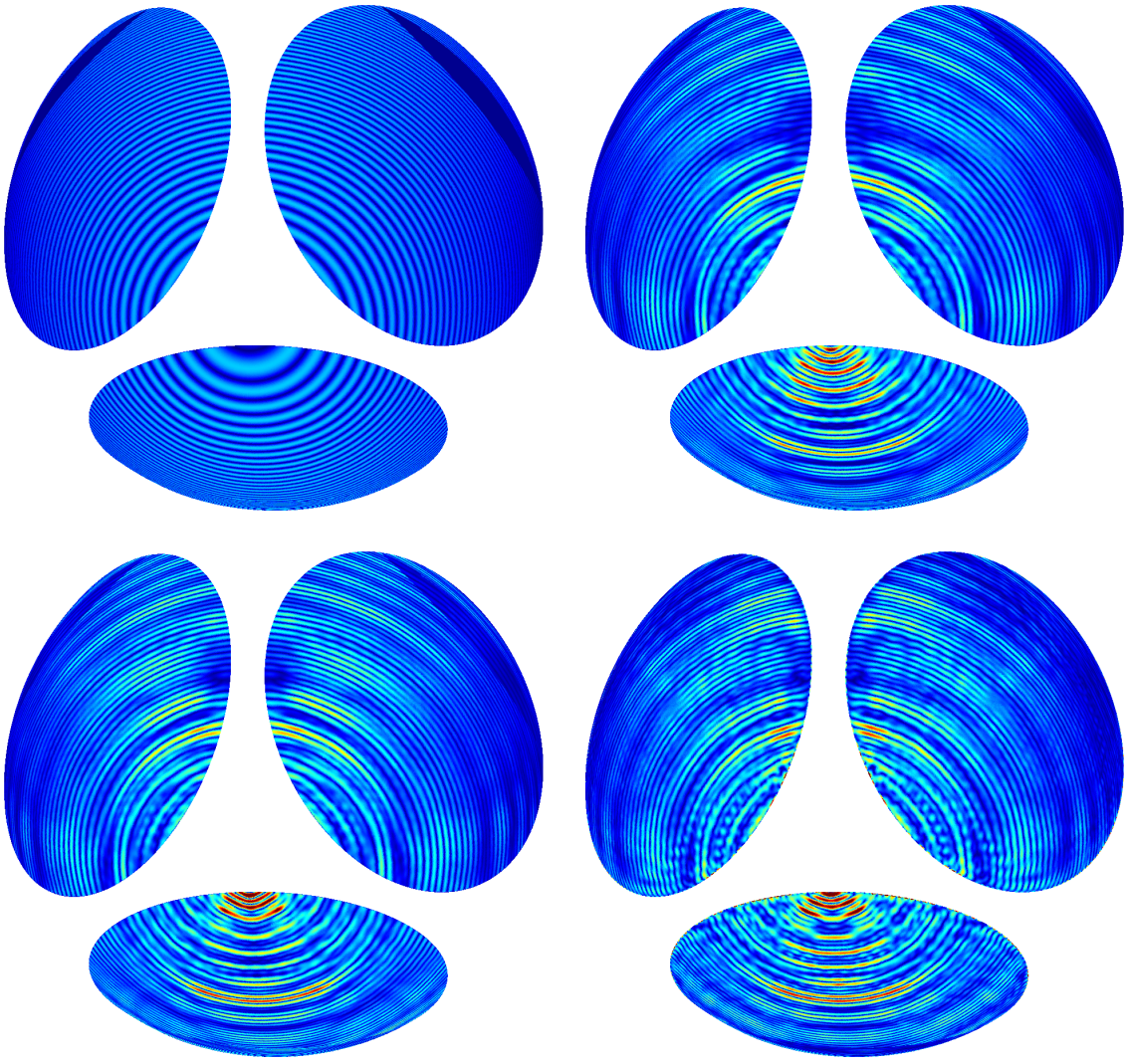

Figure 20: Induced surface currents on the spherical trihedral with $(\theta^{\text{inc}}, \phi^{\text{inc}}) = (45^\circ, 45^\circ)$, at electrical size $38.5\lambda_0$ ($N_{\text{T}} = 593,104$). Top: $K = 1$ and $K = 2$. Bottom: $K = 3$ and MLFMM solution.

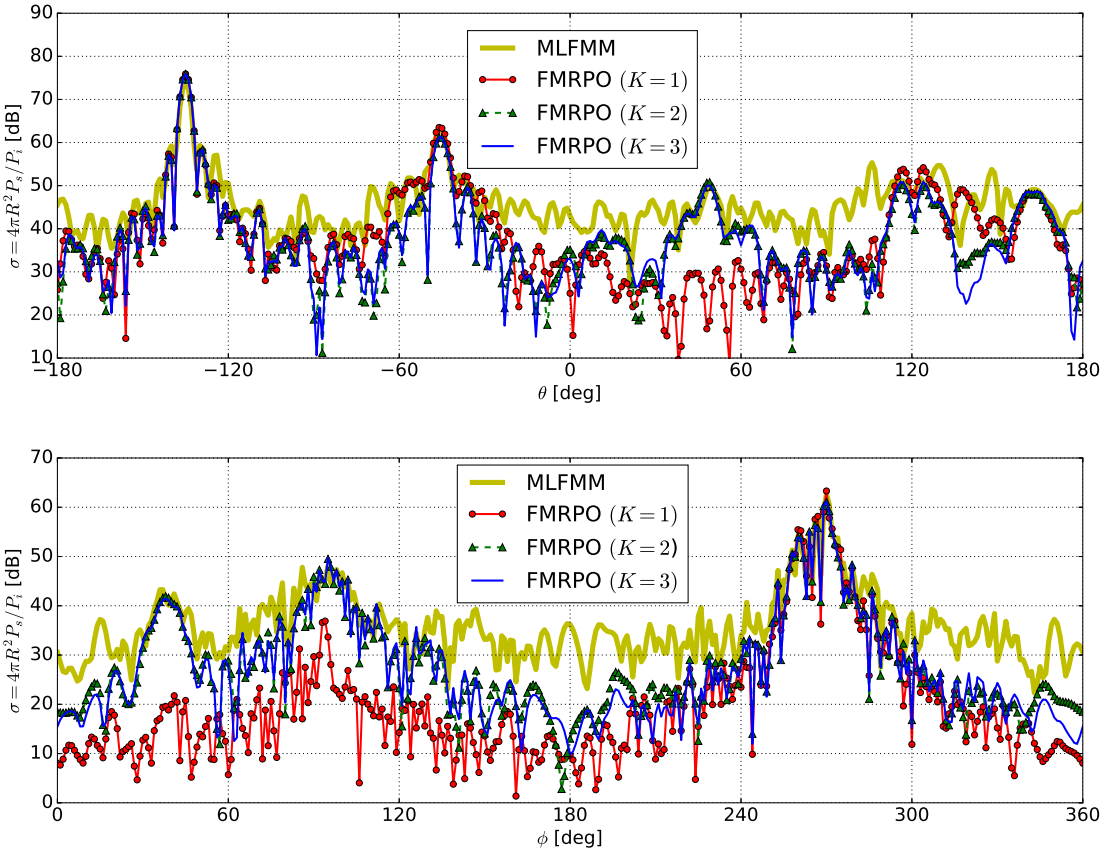

Figure 21: Bistatic RCS of the ship with $(\theta^{\text{inc}}, \phi^{\text{inc}}) = (45°, 90°)$, at electrical size $100\lambda_0$ ($N_{\text{T}} = 1,441,330$). Comparison between results with $K = 1$ to $K = 3$ and the MLFMM solution. Top: pattern cut at $\phi = 90°$. Bottom: pattern cut at $\theta = 45°$.

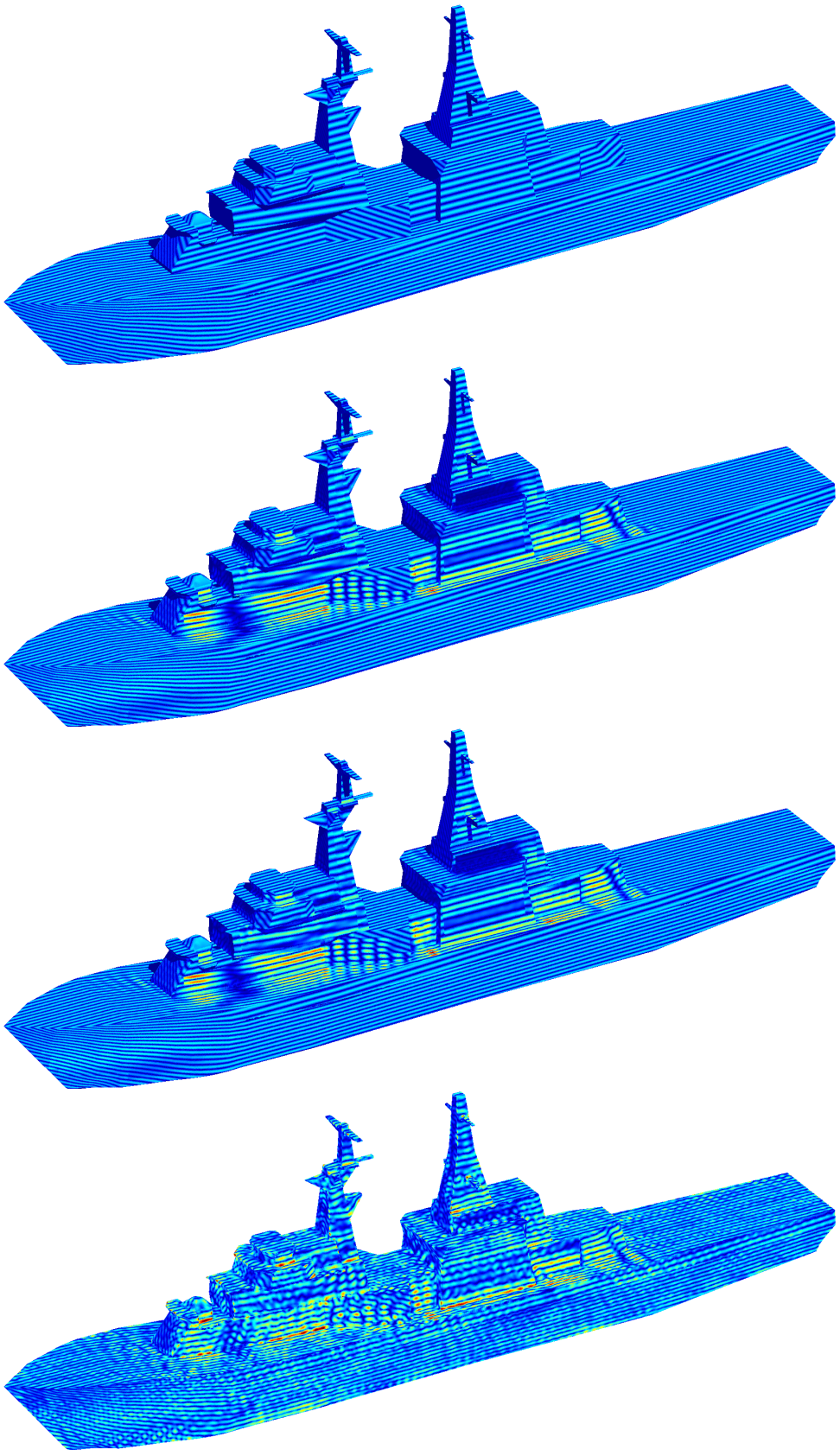

Figure 22: Induced surface currents on the ship with $(\theta^{\text{inc}}, \phi^{\text{inc}}) = (45^\circ, 90^\circ)$, at electrical size $100\lambda_0$ ($N_{\text{T}} = 1,441,330$). From top to bottom: $K = 1$, $K = 2$, $K = 3$ and MLFMM solution.

5. Conclusion

A comprehensively accelerated version of the mesh-based MRPO method (which rigorously takes internal shadowing into account), denoted FMRPO, is presented for the first time, for scattering analysis of electrically large objects. A standard representation is used for the surface current, namely RWG basis functions on a mesh of triangle elements. The MLFMM is used to accelerated internal reflection field calculations in the FMRPO. The key aspect to achieving acceleration for general geometries, is to incorporate internal shadowing into the MLFMM interaction tree. This requires an alteration to the inter-group interaction criterion of the MLFMM, as well as efficient evaluation of inter-group shadowing status flags. The runtime of the FMRPO is theoretically and practically shown, to scale as quasi-$\mathcal{O}(N_\mathrm{T} \log N_\mathrm{T})$, depending on the specific geometry.

Results are presented to assess the impact of algorithmic parameters upon the FMRPO's accuracy. Furthermore, results are presented for practical geometries with larger electrical sizes than have ever before been considered with the MRPO, but which can now for the first time be solved in realistically fast runtimes.

Given that a path to accelerated MRPO has now been established, various future developments could be considered, e.g. further small refinements to the efficient inter-group geometry identification (as discussed in Section 3.3), edge-corrections to account for diffraction effects, higher-order basis functions and parallelization.

MRPO has the notable benefit that it does not rely on any convergence process of which the number of iterations is uncertain; rather, a specified number of physical reflections are incorporated. With the FMRPO, there is no fundamental limit to the electrical size of the geometries that can be solved. E.g. the FMRPO is thus ideally suited to mono-static RCS calculations, since the factorized version of matrix $[\boldsymbol{C}_\mathrm{far}]$ (see (24) and (25)) needs only be established once, after which $K-1$ matrix-vector products are required for each direction of incidence.

The work presented in this paper could be useful to developers of electromagnetic scattering analysis tools for electrically large objects.

6. Acknowledgement

The authors gratefully acknowledge the open source project *Puma-EM* [36] (`https://sourceforge.net/projects/puma-em/`), which formed the basis of the MLFMM-related implementations.

This work was funded by Altair Development S.A. (Pty) Ltd, developers of the EM simulation software suite FEKO.

References

[1] A. F. Peterson, S. L. Ray, and R. Mittra, *Computational methods for electromagnetics*. Oxford & New York: Oxford University Press and IEEE Press, 1998.

[2] J.-M. Jin, *Theory and Computation of Electromagnetic Fields*. New York: John Wiley and Sons, 2010.

[3] W. C. Chew, E. Michielssen, J. M. Song, and J. M. Jin, *Fast and efficient algorithms in computational electromagnetics*. Artech House, Inc., 2001.

[4] N. Bojarski, "A survey of the physical optics inverse scattering identity," *IEEE Trans. Antennas Propag.*, vol. 30, no. 5, pp. 980–989, 1982.

[5] J. S. Asvestas, "The physical optics method in electromagnetic scattering," *J. Math. Phys.*, vol. 21, no. 2, pp. 290–299, 1980.

[6] W. L. Stutzman and G. A. Thiele, *Antenna Theory and Design*, 2nd ed. New York: John Wiley and Sons, 1998.

[7] R. G. Kouyoumjian and P. H. Pathak, "A uniform geometrical theory of diffraction for an edge in a perfectly conducting surface," *Proc. IEEE*, vol. 62, no. 11, pp. 1448–1461, 1974.

[8] H. Ling, R.-C. Chou, and S.-W. Lee, "Shooting and bouncing rays: Calculating the RCS of an arbitrarily shaped cavity," *IEEE Trans. Antennas Propagat.*, vol. 37, no. 2, pp. 194–205, 1989.

[9] Y. B. Tao, H. Lin, and H. J. Bao, "KD-tree based fast ray tracing for RCS prediction," *Progress In Electromagnetics Research*, vol. 81, pp. 329–341, 2008.

[10] B.-C. Kim, K.-K. Park, and H.-T. Kim, "Efficient RCS prediction method using angular division algorithm," *Journal of Electromagnetic Waves and Applications*, vol. 23, no. 1, pp. 65–74, 2009.

[11] F. Cátedra, L. Lozano, I. González, E. García, and M. Jesús Algar, "Efficient techniques for accelerating the ray-tracing for computing the multiple bounce scattering of complex bodies modeled by flat facets," *Applied Computational Electromagnetics Society Journal*, vol. 25, no. 5, pp. 395–409, 2010.

[12] S. Suk, T.-I. Seo, H.-S. Park, and H.-T. Kim, "Multiresolution grid algorithm in the SBR and its application to the RCS calculation," *Microw. Opt. Technol. Lett.*, vol. 29, no. 6, pp. 394–397, 2001.

[13] F. Weinmann, "Ray tracing with PO/PTD for RCS modeling of large complex objects," *IEEE Trans. Antennas Propagat.*, vol. 54, no. 6, pp. 1797–1806, 2006.

[14] J.-K. Bang, B.-C. Kim, S.-H. Suk, K.-S. Jin, and H.-T. Kim, "Time consumption reduction of ray tracing for RCS prediction using efficient grid division and space division algorithms," *Journal of Electromagnetic Waves and Applications*, vol. 21, no. 6, pp. 829–840, 2007.

[15] M. Domingo, F. Rivas, J. Pérez, R. P. Torres, and M. F. Cátedra, "Computation of the RCS of complex bodies modeled using NURBS surfaces," *IEEE Antennas and Propagation Magazine*, vol. 37, no. 6, pp. 36–47, 1995.

[16] F. Saez de Adana, O. Gutiérrez, I. González, M. F. Cátedra, and L. Lozano, *Practical Applications of Asymptotic Techniques in Electromagnetics*. Boston: Artech House, 2011.

[17] C. Corbel, C. Bourlier, N. Pinel, and J. Chauveau, "Rough surface RCS measurements and simulations using the physical optics approximation," *IEEE Trans. Antennas Propagat.*, vol. 61, no. 10, pp. 5155–5165, 2013.

[18] B. Persson and M. Norsell, "On modeling RCS of aircraft for flight simulation," *IEEE Antennas and Propagation Magazine*, vol. 56, no. 4, pp. 34–43, 2014.

[19] F. Obelleiro-Basteiro, J. L. Rodriguez, and R. J. Burkholder, "An iterative physical optics approach for analyzing the electromagnetic scattering by large open-ended cavities," *IEEE Trans. Antennas Propagat.*, vol. 43, no. 4, pp. 356–361, 1995.

[20] J. Pérez and M. F. Cátedra, "Application of physical optics to the RCS computation of bodies modeled with NURBS surfaces," *IEEE Trans. Antennas Propagat.*, vol. 42, no. 10, pp. 1404–1411, 1994.

[21] U. Jakobus and F. M. Landstorfer, "Improved PO-MM hybrid formulation for scattering from three-dimensional perfectly conducting bodies of arbitrary shape," *IEEE Trans. Antennas Propagat.*, vol. 43, no. 2, pp. 162–169, 1995.

[22] F.-T. Zha, S.-X. Gong, Y.-X. Xu, Y. Guan, and W. Jiang, "Fast shadowing technique for electrically large targets using z-buffer," *Journal of Electromagnetic Waves and Applications*, vol. 23, no. 2-3, pp. 341–349, 2009.

[23] J. Alvarez, I. Gómez-Revuelto, J. M. Alonso, L. E. Garcia-Castillo, and M. Salazar-Palma, "Fully coupled multi-hybrid finite element method–method of moments–physical optics method for scattering and radiation problems," *Electromagnetics*, vol. 30, no. 1-2, pp. 3–22, 2010.

[24] R. J. Burkholder, "A fast and rapidly convergent iterative physical optics algorithm for computing

the RCS of open-ended cavities," *Applied Computational Electromagnetics Society Journal*, vol. 16, no. 1, pp. 53–60, 2001.

[25] R. J. Burkholder, C. Tokgöz, C. J. Reddy, and W. O. Coburn, "Iterative physical optics for radar scattering predictions," *Applied Computational Electromagnetics Society Journal*, vol. 24, no. 2, pp. 241–258, 2009.

[26] K. E. Atkinson, *The Numerical Solution of Integral Equations of the Second Kind*. Cambridge, UK: Cambridge University Press, 1997.

[27] E. Rashidi-Ranjbar and M. Dehmollaian, "Target above random rough surface scattering using a parallelized IPO accelerated by MLFMM," *IEEE Geoscience and Remote Sensing Letters*, vol. 12, no. 7, pp. 1481–1485, 2015.

[28] D. P. Xiang and M. M. Botha, "Acceleration of multiple reflection physical optics scattering analysis with the MLFMM," in *10th European Conference on Antennas and Propagation (EuCAP)*. IEEE, 2016, pp. 1–3.

[29] M. Akbaş, L. Alatan, and O. Ergül, "Accuracy and efficiency improvements in iterative hybridization of the method of moments (MoM) and physical optics (PO)," in *10th European Conference on Antennas and Propagation (EuCAP)*. IEEE, 2016, pp. 1–5.

[30] I. Gershenzon, A. Boag, and Y. Brick, "Fast iterative physical optics with shadowing," in *IEEE Antennas and Propagation Soc. Int. Symp*, vol. 3, 2016, pp. 1363–1364, puerto Rico.

[31] S. M. Rao, D. R. Wilton, and A. W. Glisson, "Electromagnetic scattering by surfaces of arbitrary shape," *IEEE Trans. Antennas Propagat.*, vol. 30, no. 3, pp. 409–418, May 1982.

[32] D. P. Xiang and M. M. Botha, "Further progress with fast and reliable shadowing determination for mesh-based PO analysis," in *International Conference on Electromagnetics in Advanced Applications (ICEAA '15)*, Sept 2015, pp. 958–961, Torino, Italy.

[33] Altair Hyperworks Version 14.0, "FEKO User Manual," December 2015, http://www.feko.info.

[34] D. P. Xiang and M. M. Botha, "Aspects of efficient shadowing calculation for physical optics analysis of meshed objects," in *International Conference on Electromagnetics in Advanced Applications (ICEAA '14)*, Aug 2014, pp. 492–495, Aruba, Dutch Antilles.

[35] I. Wald, S. Boulos, and P. Shirley, "Ray tracing deformable scenes using dynamic bounding volume hierarchies," *ACM Transactions on Graphics (TOG)*, vol. 26, no. 1, p. 6, 2007.

[36] I. Van den Bosch, M. Acheroy, and J.-P. Marcel, "Design, implementation, and optimization of a highly efficient multilevel fast multipole algorithm," in *Computational Electromagnetics Workshop (CEM 2007)*. IEEE, 2007, pp. 1–6.

Appendix D

Conference paper — fast shadowing [46]

D. P. Xiang and M. M. Botha, **"Aspects of efficient shadowing calculation for physical optics analysis of meshed objects,"** in *16th International Conference on Electromagnetics in Advanced Applications (ICEAA2014)*, Aruba, Dutch Antilles, August 2014, 4 pages.

Aspects of efficient shadowing calculation for physical optics analysis of meshed objects

Dao P. Xiang[1], Matthys M. Botha[2]
[1]Dept of Electrical and Electronic Engineering, Stellenbosch University, South Africa
[2]Dept of Electrical and Electronic Engineering, Stellenbosch University, South Africa
E-mail: mmbotha@sun.ac.za

Abstract

This paper gives an overview of an efficient shadowing judgment algorithm for use in physical optics (PO) based electromagnetic scattering analysis. The geometry of the scatterer is represented by a mesh of triangle elements (N) and the currents by RWG basis functions. A direct approach to shadowing judgment will yield O(N^2) time scaling, which will be very time consuming. The proposed algorithm makes use of a buffer which splits up the field of view of the illuminating source and yields O(N) time scaling. Careful attention has been paid to the optimization of various algorithmic aspects. Numerical results are presented to demonstrate the efficiency and accuracy of the proposed algorithm.

I. INTRODUCTION

The physical optics (PO) approximation is commonly used for scattering analysis of electrically large, conducting objects [1]; with the geometry being represented by a mesh of triangle elements and the currents by RWG basis functions (see e.g. [2]). To make use of the PO approximation the shadowing information of each triangle in the mesh with respect to the illumination of interest (typically a plane wave or a point source [Hertzian dipole]), is required.

Establishing shadowing information involves determining for each element whether it is visible to the source, or not. This task can be very time-consuming when following the direct approach of considering each element in relation to all other elements in turn. A more sophisticated approach is required. A well-known solution is to make use of a buffer which splits up the field of view of the source. Implementations of this idea are either pixel-based (employing the graphics processor), or follow a software buffer approach.

The pixel-based approach is the hardware z-buffer shadowing technique used in 3-D graphics [3], [4]. The graphics processor is employed to determine which part of the object has the smallest z-axis coordinate value at each pixel. This then yields the shadowing information at pixel-level resolution, of the object. The software buffer approach uses the z-buffer concept, but is not restricted in resolution and does not need to make use of a graphics processor [5]. It was found that in order to realize the full potential of the software buffer approach, careful attention must be paid to various algorithmic aspects.

This paper gives an overview of an efficient shadowing judgment algorithm which is based on the software buffer approach. This is followed by results to demonstrate the performance of the algorithm.

II. PROPOSED ALGORITHM

Consider the PO-based analysis of an electrically large PEC object illuminated by a plane wave. The surface currents are approximated with RWG basis functions on a mesh of triangle elements. In this section the proposed shadowing judgment algorithm will be discussed. The algorithm is based on constructing a buffer data structure for the whole mesh and then using the buffer to efficiently judge the shadowing of each triangle.

A. Construction of the buffer

Start by choosing the buffer plane as a perpendicular plane to the direction of incidence and project the whole mesh into this plane. After this projection, the bounding box in the buffer plane for the entire structure can be found. Let L_x and L_y denote the dimensions of the object's bounding box in the buffer plane, as shown in Figure 1.

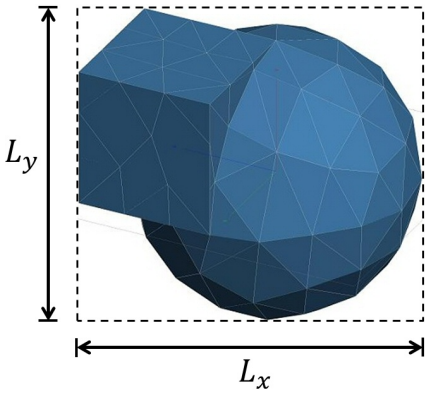

Fig. 1. Buffer plane bounding box.

Next, the buffer is subdivided into boxes (analogous to pixels in the z-buffer algorithm). The buffer box size must be determined in order to achieve an $O(N)$ algorithm (where N is the number of triangle elements in the mesh). The buffer box size is thus set to the average edge length of the mesh l_{ave}. The number of subdivisions N_x in the x-direction and N_y in the y-direction can be calculated as

$$N_x = \left\lceil \frac{L_x}{l_{\text{ave}}} \right\rceil; \quad N_y = \left\lceil \frac{L_y}{l_{\text{ave}}} \right\rceil$$

where $\lceil \cdot \rceil$ refers to the ceiling function. The total number of buffer boxes is thus $N_{\text{box}} = N_x \times N_y$.

After the subdivision, the projection onto the buffer plane of each triangle is considered in turn. All of the buffer boxes intersecting with the projection of each triangle is found and the triangle's information is recorder in those buffer boxes. After concluding this step, the buffer construction is finished.

B. One-by-one checking with depth information

The buffer can now be used to determine the shadowing status of the centroid of each triangle (which is considered to be the shadowing status of the triangle itself). For each triangle project its centroid into the buffer and find the buffer box to which it belongs. To determine the triangle's visibility, it only needs to be compared with the set of triangles listed in that specific buffer box. A one-by-one checking procedure with depth information is followed. This involves checking the current triangle against each of the triangles listed in the buffer box which are also closer to the source, thus making use of the depth information. As soon as shadowing is detected, checking is terminated. If the current triangle is not shadowed by any triangles in front of it, the current triangle will be visible. Using the depth information, triangles behind the current triangle are not unnecessarily considered. Using the depth information saves almost 70% of shadowing judgment time, as compared to not using it.

However, the checking as described above may cause mistakes, because a triangle could in fact be shadowed by another one with slightly larger depth. In order to guarantee error

free shadowing judgment, the current triangle should be checked against all those triangles up to a distance δ behind it, in the buffer box. The value of δ is determined as follows:

$$\delta = \max_{\substack{i\in\{1,\cdots,N\}\\ j\in\{1,2,3\}}} |\vec{r}_{ij} - \vec{r}_{ic}|$$

where $\vec{r}_{ij}$ is the vertices of the i-th triangle and $\vec{r}_{ic}$ is its centroid.

After including this δ, the shadowing judgment algorithm is guaranteed to be error free.

C. Shadowing judgment for grazing view

If the object contains large plane surfaces and the incident plane wave is at grazing incidence, many triangles on that plane will be projected into a single buffer box in the proposed shadowing judgment algorithm. This will be inefficient. Thus a special procedure is followed for the grazing view case. Buffer boxes containing grazing view triangles are appropriately subdivided such that the new buffer boxes do not contain excessive numbers of triangles. After adding the new buffer boxes the shadowing judgment procedure continues as described above.

III. NUMERICAL RESULTS

The performance of the proposed algorithm will now be investigated by comparing it with the commercial PO solver in FEKO [6]. All of these simulations were run on the same platform.

A. Plane wave shadowing judgment efficiency

Start by considering the two objects shown in Figure 2. One is a simple cube and the other is a more complex model. The overall dimensions of the complex model are the same as that of the cube, but it is subdivided into eight small cubes and some of the smaller cube faces have been removed or distorted.

The shadowing judgment run-times for these two objects, when uniformly meshed with roughly the same number of elements, is compared in Table I. It can be observed that the performance of the proposed algorithm is practically unaffected by the differences in geometry.

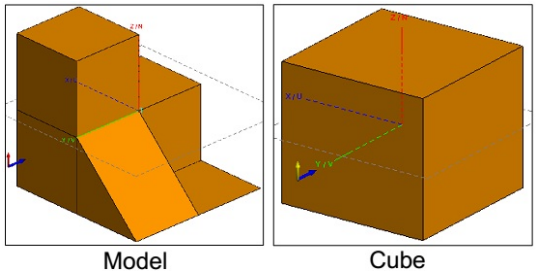

Fig. 2. Objects used for shadowing comparision.

Object		Run-time [s]	
Name	# elements	FEKO	Proposed
Model	198, 130	3.791	0.540
Cube	182, 612	4.321	0.460

TABLE I
COMPARISON OF SHADOWING JUDGMENT RUN-TIMES FOR PLANE WAVE ILLUMINATION OF THE TWO OBJECTS SHOWN IN FIGURE 2.

Now consider run-time scaling. The uniform mesh size of the complex model is varied and the shadowing judgment run-time is recorded for each mesh. The results are shown in

Figure 3. From the results it is clear that the proposed algorithm scales as $O(N)$ and that it is almost nine times faster than FEKO.

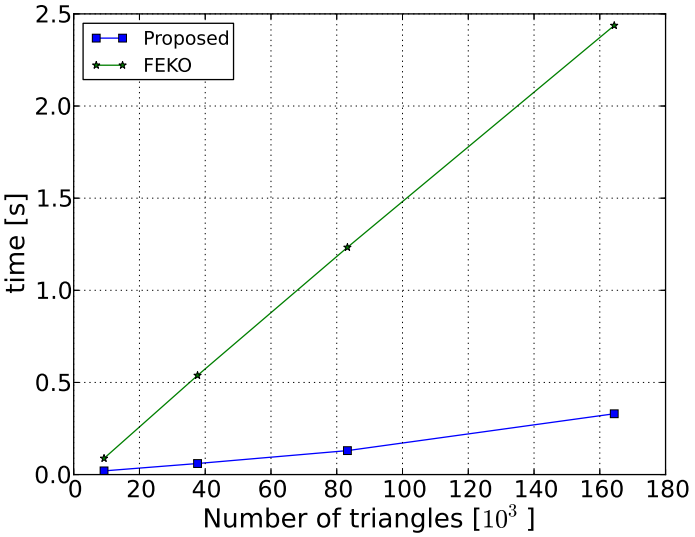

Fig. 3. Plane wave shadowing judgment run-time scaling.

B. Accuracy evaluation

The accuracy of the proposed algorithm will now be verified. For this evaluation a model of an Airbus A380 aircraft with fine geometric details is used, as shown in Figure 4. The model consists of 773, 974 triangle elements. The scattered far field is calculated at 300MHz.

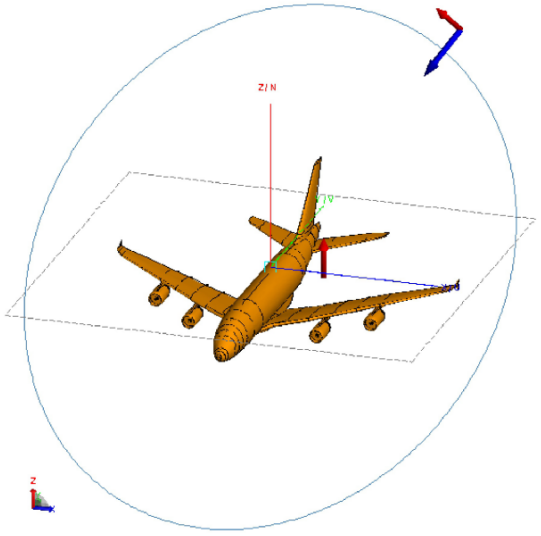

Fig. 4. Airbus A380 model, showing the direction of the incident plane wave (blue arrow) and the point source location and orientation (single red arrow).

1) Plane wave illumination: For plane wave illumination, the incident direction is set to $\theta_{\text{inc}} = 45°$ and $\phi_{\text{inc}} = 45°$. The far field is calculated along the circular arc defined by $\phi = 45°$ and θ from 0° to 360°. These details are shown in Figure 4. The shadowing judgment result is shown in Figure 5. The shadowing judgment time with the proposed algorithm was 2.49 seconds and for FEKO it was 21.38 seconds. The scattered far field results are compared

in Figure 6. It can be seen in Figure 6 that the results obtained with the two codes agree very well, which confirms the accuracy of the proposed algorithm. Small discrepancies are due to different current projection procedures being used at edges.

Fig. 5. Shadowing judgment result for plane wave illumination. Red = illuminated; blue = shadowed.

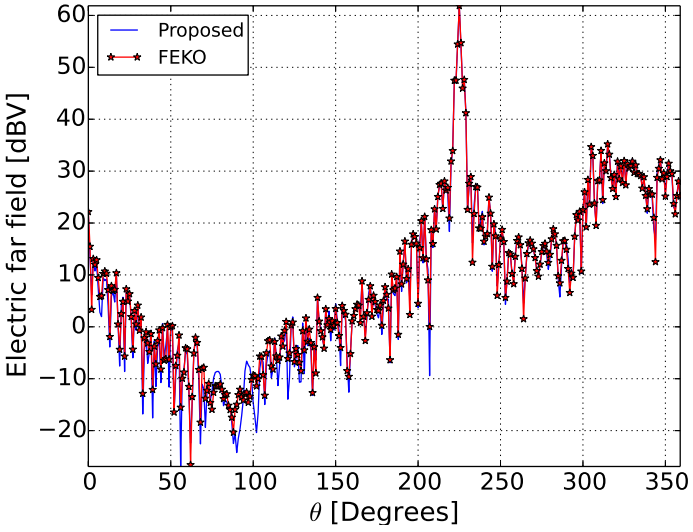

Fig. 6. Scattered far field result for plane wave illumination.

2) Point source illumination: The proposed shadowing judgment algorithm for plane wave illumination can also be formulated for point source illumination. The following results are included, though the details of the formulation are beyond the scope of the present paper.

Consider an electric dipole as the illuminating source. The dipole is located at $(x, y, z) = (10\text{m}, 10\text{m}, 0\text{m})$ and is oriented along the positive z-direction, as shown in Figure 4. The far field is calculated along the same circular arc as before. The shadowing judgment result is shown in Figure 7. The shadowing judgment time with the proposed algorithm was 3.08 seconds and for FEKO it was 27.10 seconds. The scattered far field results are compared in Figure 8, which confirms the accuracy of the proposed algorithm for point source illumination.

IV. CONCLUSION

Shadowing judgment in PO-based scattering analysis can be very time consuming for electrically large objects. Thus it is important to use an optimized $O(N)$ shadowing judgment

Fig. 7. Shadowing judgment result for electric dipole illumination. Red = illuminated; blue = shadowed.

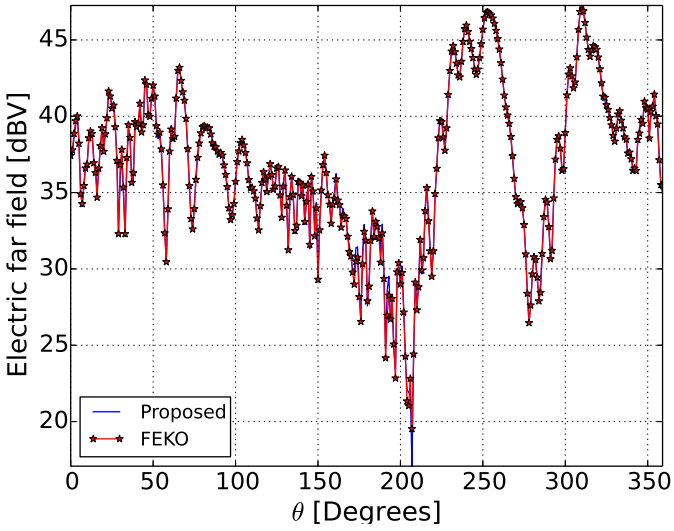

Fig. 8. Scattered far field result for electric dipole illumination.

algorithm. Aspects of such a shadowing judgment algorithm were presented in this paper. The numerical results indicate that the proposed algorithm is fast and accurate.

ACKNOWLEDGMENTS

This work was supported by EM Software & Systems - S.A. (Pty) Ltd, developers of the EM simulation software suite FEKO.

REFERENCES

[1] D. Elking, J. Roedder, D. Car, and S. Alspach, "A review of high-frequency radar cross section analysis capabilities at mcdonnell douglas aerospace," *IEEE Antennas and Propagation Magazine*, vol. 37, no. 5, pp. 33–42, 1995.

[2] U. Jakobus and F. M. Landstorfer, "Improved PO-MM hybrid formulation for scattering from three-dimensional perfectly conducting bodies of arbitrary shape," *IEEE Trans. Antennas Propagat.*, vol. 43, no. 2, pp. 162–169, February 1995.

[3] A. Van Dam, S. Feiner, and J. Hughes, "Computer graphics: Principles and practice," *Reading: Addison Wesley*, 1990.

[4] J. M. Rius, M. Ferrando, and L. Jofre, "GRECO: Graphical electromagnetic computing for RCS prediction in real time," *IEEE Antennas and Propagation Magazine*, vol. 35, no. 2, pp. 7–17, 1993.

[5] F.-T. Zha, S.-X. Gong, Y.-X. Xu, Y. Guan, and W. Jiang, "Fast shadowing technique for electrically large targets using z-buffer," *Journal of Electromagnetic Waves and Applications*, vol. 23, no. 2-3, pp. 341–349, 2009.

[6] EM Software & Systems - S.A. (Pty) Ltd, *FEKO Suite 7.0 User Manual*, May 2014.

Appendix E

Conference paper — fast shadowing [47]

D. P. Xiang and M. M. Botha, **"Further progress with fast and reliable shadowing determination for mesh-based PO analysis,"** in *17th International Conference on Electromagnetics in Advanced Applications (ICEAA2015)*, Torino, Italy, Sep-tember 2015, 4 pages.

Further progress with fast and reliable shadowing determination for mesh-based PO analysis

Dao P. Xiang[1], Matthys M. Botha[2]
[1]Dept of Electrical and Electronic Engineering, Stellenbosch University, South Africa
[2]Dept of Electrical and Electronic Engineering, Stellenbosch University, South Africa
E-mail: mmbotha@sun.ac.za

Abstract

The physical optics (PO) approximation is commonly used for scattering analysis of objects represented by a mesh of triangle elements. For PO-based analysis the shadowing information of each triangle with respect to the illumination is required (point source or plane wave). This task can be efficiently performed by splitting up the field of view into buffer boxes to localize shadowing checking. This works very well, except that inhomogeneous meshes and grazing incidence can have severe adverse effects upon computational efficiency. Further progress toward obtaining an algorithm which may generally be regarded as of O(N) complexity with provision for efficient, robust handling of extreme mesh inhomogeneity and grazing incidence is presented in this paper.

I. INTRODUCTION

The physical optics (PO) approximation is very commonly used for scattering analysis of electrically large, conducting objects [1], [2], [3]. Here the focus is on objects represented by a mesh of sub-wavelength sized triangle elements [4], [5], [6]. To make use of the PO approximation the shadowing information of each triangle in the mesh with respect to the illumination of interest is required. Typical illuminations of interest are a point source (Hertzian dipole) at some specified location or a plane wave with given angles of incidence. Both of these sources will be considered here.

Determining the shadowing information of each element in the mesh can be efficiently achieved by splitting up the field of view into buffer boxes and then compiling lists of all mesh elements projecting into each buffer box. The field of view is defined as the bounding box of the whole mesh, when projected onto an eikonal surface of the illuminating source, with appropriate orthogonal coordinate system defined on that surface. The buffer is then used to determine the small set of elements which need to be considered to determine the shadowing information for a given point.

This works very well and indeed, an optimized $O(N)$ run time algorithm may readily be constructed for the case of plane wave illumination of homogeneous meshes of general structures, as discussed in [7] (where N denotes the number of mesh elements).

However, inhomogeneous meshes and grazing incidence can have severe adverse effects upon computational efficiency. This paper will present further progress relative to [7], with respect to obtaining an algorithm which may generally be regarded as of $O(N)$ complexity with provision for efficient handling of extreme mesh inhomogeneity and grazing incidence, such that it may be fast and robust for general use.

II. REMAINING ISSUES WITH THE BUFFER-BASED SHADOWING ALGORITHM OF [7]

In [7] a buffer-based algorithm was presented which was shown to be very effective for shadowing determination for plane wave illumination of homogeneously meshed objects — complexity of $O(N)$ was achieved. This even held for grazing incidence, since a special

buffer box subdivision was proposed for boxes containing many plane wave grazing view triangles. The algorithm was also formulated for point source illumination, in which case the buffer plane is the $\theta\phi$-surface in spherical coordinates. The grazing incidence treatment does however not translate to the point source setup. Altogether, this will be referred to as the "normal buffer" algorithm.

With this normal buffer algorithm, there are three cases when many triangles will project into a single buffer box. This can possibly lead to a large number of shadowing checks having to be conducted for a test point projecting into such a box, which will cause efficiency to deteriorate. These three cases are illustrated in Figure 1.

With an inhomogeneous mesh many triangles can fall into a single buffer box, since the box dimension is chosen based on the average mesh size. When point source grazing incidence occurs, triangles project into the buffer plane as slivers lying along a curved line and many can fall into a single buffer box. For overlapping surfaces the number of triangles listed in the buffer box will be proportional to the number of overlapping surfaces.

Overlapping surfaces is not a serious problem, as the triangles in each buffer box is sorted according to depth, such that a point is checked first against the closest triangles. This ensures that in the case of overlapping surfaces, only a few checks will typically be necessary, independent of the number of overlapping surfaces. However, the algorithm can sometimes be severely hampered by inhomogeneous meshes and point source grazing incidence. In particular, the point source buffer is more prone to these problems, as even for a homogeneous mesh one finds that after projection into the $\theta\phi$-buffer plane, the projected mesh is most often inhomogeneous.

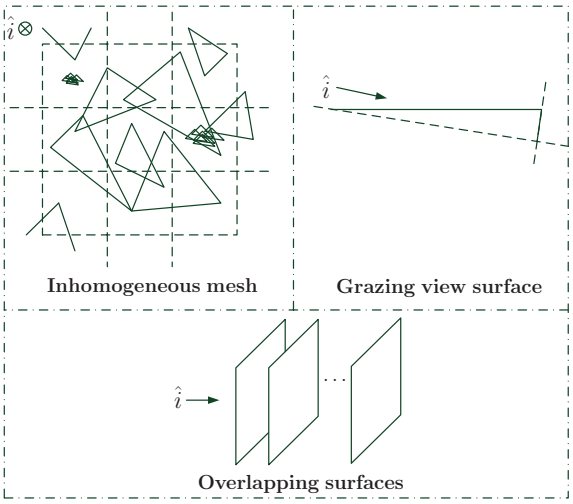

Fig. 1. Cases where a high number of elements can project into a single buffer box in the normal buffer algorithm of [7]. The direction of incidence is indicated by $\hat{i}$.

III. ADAPTIVE BUFFER-BASED SHADOWING ALGORITHM

In order to solve the problems discussed in Section II an adaptive buffer-based algorithm is proposed, which relies on a recursive approach. The general procedure is as follows:

1) Project all triangles into the buffer plane and construct the normal buffer according to [7].
2) Identify buffer boxes containing an excessive number of triangles (e.g. more than 100). All triangles in each of these boxes are then treated as a new object, to which the normal buffer algorithm is applied.
3) Recursively construct the buffer until all buffer boxes contain a small number of triangles.

During this procedure the type of problem case must be identified, because refinement should only be applied to inhomogeneous boxes and not to overlapping surfaces. A test for inhomogeneity is used.

Regarding grazing incidence, it was noted that the normal buffer algorithm already handles grazing incidence well in case of plane wave incidence upon homogeneous meshes. In that case the buffer box is subdivided into a set of flat boxes which lie orthogonal to the average normal vector to the grazing view triangles, as viewed in the buffer plane. This method is not also applicable to point source grazing incidence, because in the point source case due to the spherical coordinate transformation, the projected mesh is generally inhomogeneous in the buffer plane, even if the actual mesh is homogeneous. This inhomogeneity causes inefficiency, even if grazing incidence could be treated.

The solution to the problem is to first subdivide the grazing view triangles such that individual buffer box dimensions are proportional to the average size of the triangles in them. At this point the special grazing view subdivision of those boxes can be carried out to yield a good separation of grazing view triangles in the final buffer, even for inhomogeneous meshes under point source illumination.

Note that both the normal buffer and adaptive buffer algorithms are error free and reliable under all circumstances.

IV. NUMERICAL RESULTS

Three test problems will be considered to demonstrate the superior efficiency of the adaptive buffer shadowing algorithm and to highlight specific algorithmic features.

A. *Point source above a flat strip*

A Hertzian dipole (point source) is located at a distance z above a flat surface with dimensions as shown in Figure 2. The surface is homogeneously meshed with 308, 330 triangle elements. The shadowing determination run time will be considered as a function of the distance z. As the dipole nears the surface, so will the extremity of the grazing incidence increase; also, as it nears the surface, so will the ratio between the distances to the nearest and farthest elements increase and with it, the level of mesh inhomogeneity after projection into the $\theta\phi$-buffer plane. Given the fact that PO is typically applied to large and smooth structures, it follows that this problem will be quite commonly encountered which makes this a very relevant test.

Figure 3 shows the run time results. The adaptive buffer algorithm and normal buffer algorithm are compared. Results obtained with the commercial PO solver in FEKO are also included for reference [8]. The adaptive algorithm run time is virtually independent of the distance to the source, while the other two results exhibit a dramatic decrease in efficiency as the source nears the surface. This result demonstrates the adaptive buffer algorithm's ability to deal effectively with highly inhomogeneous meshes as well as point source grazing incidence.

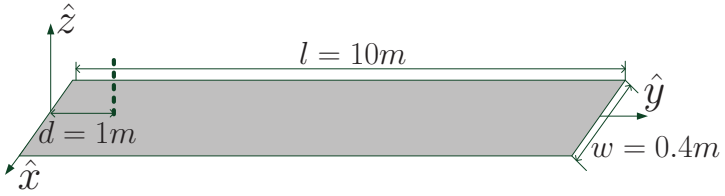

Fig. 2. Flat strip geometry with the dipole locations indicated by a dotted line.

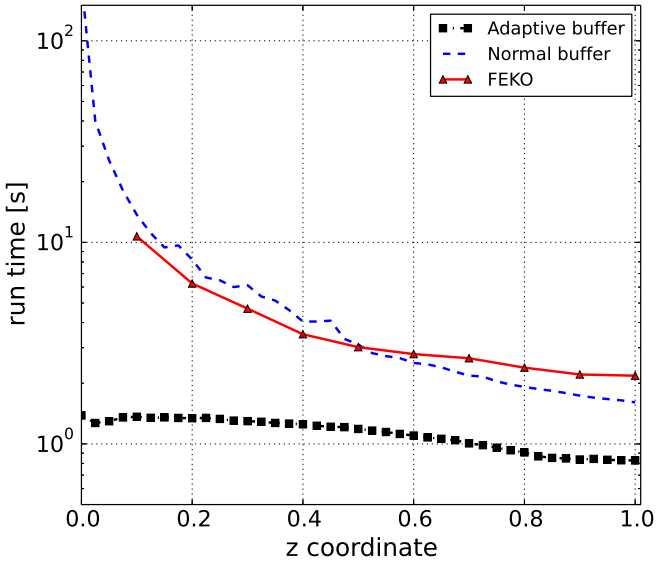

Fig. 3. Shadowing run time on a log scale, for the setup in Figure 2.

B. *Point source above a sphere*

The model is shown in Fig 4. The sphere is centred around the origin with radius 1.5 m. It is uniformly meshed with 775, 800 triangle elements. The dipole is located on the z-axis.

Figure 5 shows the shadowing determination run time results. In this case the number of grazing incidence triangles forms a much smaller portion of the total number of triangles and also, they do not increase as the source nears the surface. This means that the effective mesh inhomogeneity (after projection into the buffer) is much less significant than for the previous example. Consequently, the normal and adaptive buffer algorithms perform very similarly.

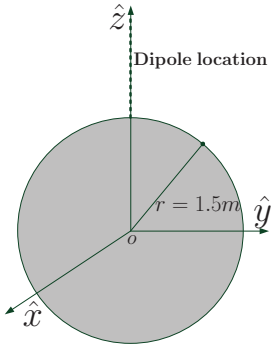

Fig. 4. Sphere surface geometry with the dipole locations indicated by a dotted line.

C. *Plane wave illumination of a realistic aircraft model*

Consider a realistic aircraft model, uniformly meshed with 1, 574, 660 elements. Figure 6 shows the model along with a visualization of the range of incident plane wave directions considered — it is a range of 30°, centred around head-on incidence (occurring at $\theta = 90°$). Grazing incidence will occur as $\theta = 90°$ is approached.

Figure 7 shows the results. As expected, the buffer-based algorithms perform very similarly, with their performances completely unaffected by the angle of incidence. The FEKO result shows an efficiency deterioration around grazing incidence.

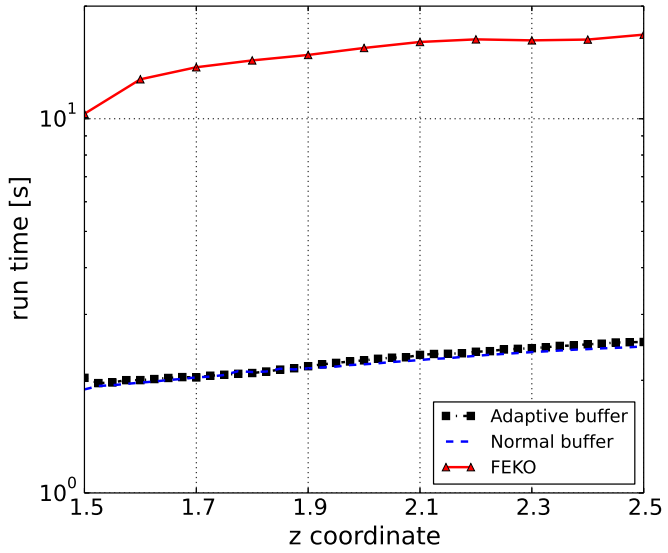

Fig. 5. Shadowing run time on a log scale, for the setup in Figure 4.

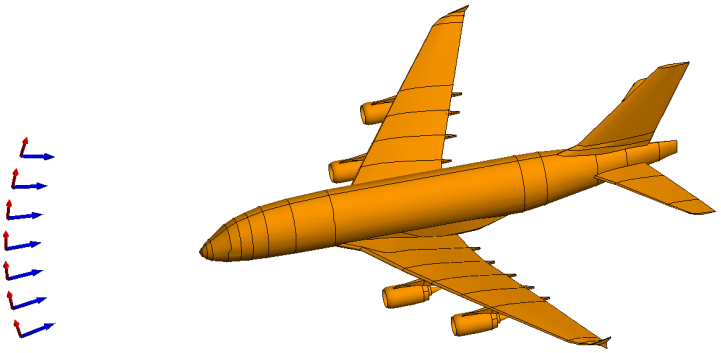

Fig. 6. Aircraft model with the range of plane wave incident angles also visualized.

V. CONCLUSION

A buffer-based algorithm for PO-analysis shadowing determination was proposed by the present authors in a previous paper [7]. Though that algorithm yielded $O(N)$ run time under various circumstances and though it was observed to be generally more efficient that the shadowing determination scheme in the PO solver of FEKO, it was nevertheless found to have some deficiencies. In the present paper these deficiencies were discussed and an overview of the recursive extension of the scheme was given. The new scheme addresses all the deficiencies and results where shown to demonstrate the new scheme's superior stability and efficiency.

ACKNOWLEDGMENT

This work was supported by Altair Development S.A. (Pty) Ltd, developers of the EM simulation software suite FEKO.

REFERENCES

[1] J. S. Asvestas, "The physical optics method in electromagnetic scattering," *Journal of Mathematical Physics*, vol. 21, no. 2, pp. 290–299, 1980.

[2] M. F. Catedra, C. Delgado, S. Luceri, O. G. Blanco, and F. S. de Adana, "Physical optics analysis of multiple interactions in large scatters using current modes," *IEEE Trans. Antennas Propag.*, vol. 54, no. 3, pp. 985–994, 2006.

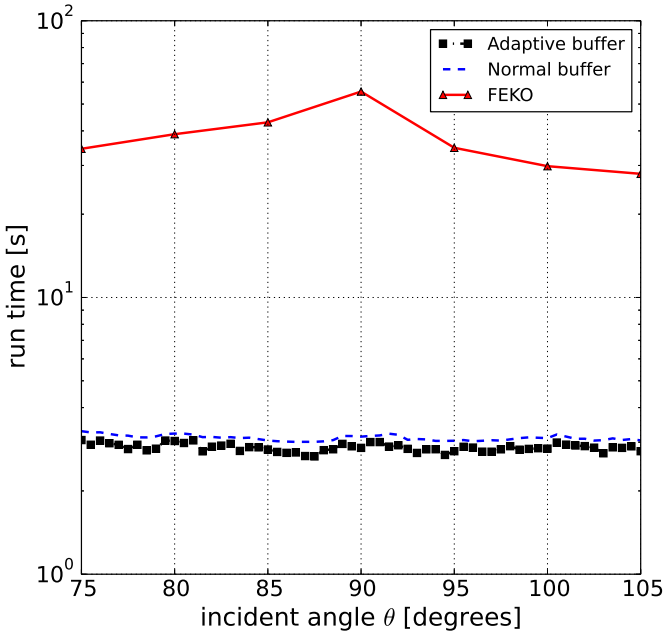

Fig. 7. Shadowing run time on a log scale, for the setup in Figure 6.

[3] N. Bojarski, "A survey of the physical optics inverse scattering identity," *IEEE Trans. Antennas Propag.*, vol. 30, no. 5, pp. 980–989, 1982.

[4] U. Jakobus and F. M. Landstorfer, "Improved PO-MM hybrid formulation for scattering from three-dimensional perfectly conducting bodies of arbitrary shape," *IEEE Trans. Antennas Propag.*, vol. 43, no. 2, pp. 162–169, 1995.

[5] Y. Zhao, "Fast physical optics calculation for SAR imaging of complex scatterers," Master's thesis, The Ohio State University, 2012.

[6] L. N. Medgyesi-Mitschang and D.-S. Wang, "Hybrid methods for analysis of complex scatterers," *Proceedings of the IEEE*, vol. 77, no. 5, pp. 770–779, 1989.

[7] D. P. Xiang and M. M. Botha, "Aspects of efficient shadowing calculation for physical optics analysis of meshed objects," in *International Conference on Electromagnetics in Advanced Applications (ICEAA '14)*, Aug 2014, pp. 492–495, Aruba, Dutch Antilles.

[8] Altair Hyperworks Version 14.0, "FEKO User Manual," December 2015, http://www.feko.info.

Appendix F

Conference paper — fast MRPO [49]

D. P. Xiang and M. M. Botha, **"Acceleration of multiple reflection physical optics scattering analysis with the MLFMM,"** in *10th European Conference on Antennas and Propagation (EuCAP2016)*, Davos, Switzerland, April 2016, 3 pages.

Acceleration of Multiple Reflection Physical Optics Scattering Analysis with the MLFMM

Dao P. Xiang[1], Matthys M. Botha[2]
[1]Dept of Electrical and Electronic Engineering, Stellenbosch University, South Africa
[2]Dept of Electrical and Electronic Engineering, Stellenbosch University, South Africa
E-mail: mmbotha@sun.ac.za

Abstract

The physical optics (PO) approximation is commonly used for scattering analysis of electrically large, conducting objects. The standard PO approximation is purely local and does not take multi-bounce effects into account. The multiple reflection PO (MRPO) method takes multiple reflections into account in an iterative manner. In this paper the mesh-based MRPO with standard RWG basis functions on triangle elements is considered. In cases where shadowing can be pre-specified based on physical insight, the main computational bottleneck is the integration over the currents to obtain the next reflection's contribution to the surface current. It is shown that the multilevel, fast multipole method (MLFMM) can be used to accelerate these calculations significantly, while yielding essentially identical results as the MRPO with conventional integration.

Index Terms

Computational electromagnetics; recursive update; radar cross section (RCS); magnetic field integral equation (MFIE).

I. Introduction

The analysis of scattering from electrically large, conducting objects is important for radar cross section (RCS) calculations. The physical optics (PO) approximation is commonly used for scattering analysis in such cases [1], [2]. The standard PO approximation is purely local and does not take multi-bounce effects into account. The multiple reflection PO (MRPO) method was developed to analyse electromagnetic scattering from arbitrarily shaped open-ended cavities which are electrically large [3], [4]. As its name implies, the principles of physical optics (PO) are applied iteratively to evaluate the induced surface currents, taking multiple reflections into account. MRPO was developed to handle arbitrarily shaped objects and given that full integration over currents is used, it may obtain better accuracy than ray-based methods such as the shooting and bouncing rays (SBR) approach [5].

In this paper the mesh-based MRPO with standard RWG basis functions on triangle elements, is considered [see e.g. [6] on the use of this discretization scheme for single reflection PO (SRPO)]. In cases where shadowing can be pre-specified based on physical insight, the main computational bottleneck is the integration over the currents to obtain the next reflection's contribution to the surface current. Here it is shown that the multilevel, fast multipole method (MLFMM) can be used to accelerate these calculations significantly, while yielding essentially the same results as the MRPO with conventional integration. Such acceleration is not uncommon, as the fast far field approximation (FaFFA) has been used before in this way [3]. However, the MLFMM is generally considered more accurate than the FaFFA and faster.

In Section II the MLFMM-accelerated MRPO method is briefly presented. Sections III and IV present preliminary numerical results and a concluding discussion, respectively.

II. MRPO accelerated with MLFMM

In the case of a fully illuminated structure (i.e. when no shadowing determination is necessary), the MRPO method is limited by an $O(N^2)$ operational count per reflection,

where N is the total number of RWG basis functions representing the current. This is due to the field calculation requirement. Evaluating the field at every basis function can be expressed as a matrix-vector product, hence the computational cost of $O(N^2)$. This matrix-vector product can be accelerated by the MLFMM. This section provides a brief overview of the MLFMM-accelerated MRPO formulation.

A. The MRPO method

The induced currents on a conducting object represented by a mesh, are first found using the PO approximation as in [6].

$$\vec{J}^{(0)}(\vec{r}) = 2\hat{n} \times \vec{H}^{i}(\vec{r}). \tag{1}$$

This is the SRPO method. These currents then radiate towards other parts of the object and induce additional currents according to the PO approximation, which represent successive reflections. The current after l additional reflections is found by way of the following recursive expression [4]:

$$\vec{J}^{(l)}(\vec{r}) = \vec{J}^{(0)}(\vec{r}) + 2\hat{n} \times \int\!\!\!\!\!\!-_{S} \vec{J}^{(l-1)}(\vec{r}') \times \hat{R} \frac{e^{-jkR}}{4\pi R} \left(jk + \frac{1}{R} \right) dS' \tag{2}$$

where $\vec{R} = \vec{r} - \vec{r}'$, $R = |\vec{R}|$, $\hat{R} = \vec{R}/R$; $\vec{r}'$ and $\vec{r}$ are the source and observation points on the surface S, respectively. The symbol $\int\!\!\!\!\!\!-$ denotes the principle value integral. For example, the iteration process can be stopped after a pre-specified number of reflections based on the number of expected significant reflections supported by a given model.

For general complex objects, shadowing will have to be taken into account in (2). As noted already, only cases without shadowing are considered here.

B. MRPO accelerated with MLFMM

Using RWG basis functions to represent the current on the surface and testing for each normal current component across an edge in (2), the MRPO iteration can be expressed as a matrix equation:

$$I^{(l)} = I^{(0)} + AI^{(l-1)} \tag{3}$$

where $I^{(l)}$ represents the vector of current coefficients after l additional reflections and $I^{(0)}$ represents the vector of current coefficients corresponding to the initial, single-reflection PO current. The dimensions of matrix A is $N \times N$.

The complexity of the computer operation count for executing the recursive relation (3) is $O(N^2)$. The MLFMM can be used to speed up the matrix-vector product, as the operation complexity of the MLFMM for this task is $O(N \log N)$.

With the MLFMM the matrix is split up into a sparse near-interaction matrix and the remaining far-interaction part. The latter is represented by the MLFMM in a factorized format.

$$I^{(l)} = I^{(0)} + \left(A^{\text{near}} + A^{\text{far}} \right) I^{(l-1)}. \tag{4}$$

A matrix-vector product involving A^{near} has cost $O(N)$, while a product involving the factorized version of A^{far} has cost $O(N \log N)$ (see e.g. [7] for further details). This may be compared with the scaling achieved using FaFFA acceleration, which is given as $O(N^{5/3})$ in [3].

III. Numerical results

In this section, three methods are compared:

1) MLFMM-MRPO: this is the method described above, namely the MRPO with MLFMM acceleration of the recursive, reflection calculation procedure.
2) MRPO-FEKO: this is the MRPO method using standard integration for the recursive, reflection calculation procedure. The commercial implementation in FEKO is used [8], to assess the new method against a well-implemented reference, both for accuracy and runtime.
3) MLFMM-FEKO: this is the full method of moments (MoM) solution based on the electric field integral equation (MLFMM is used instead of standard MoM, in the interest of efficiency) to obtain a reference to assess the accuracy of the MRPO approach itself.

Two test cases are considered: a dihedral structure and a trihedral structure, as shown in Figure 1. Throughout, $\lambda/10$ meshing is used.

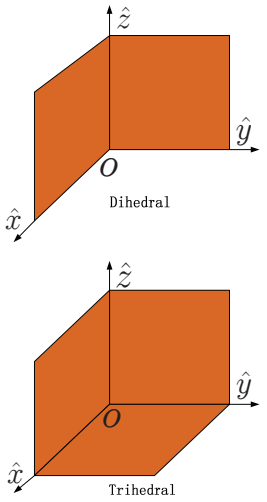

Fig. 1. The two conducting plate models used for testing. The plate dimensions are all 1 m.

A. Dihedral

The accuracy of the new MRPO implementation is verified by solving the dihedral model at 1 GHz. The plane wave incident angles are $\theta = 90°$ and $\phi = 45°$. Three reflections are incorporated with the MRPO ($l = 2$). Figure 2 shows the scattered far field results. It can be seen that the MRPO accelerated with MLFMM indeed produces a result very close to that of the conventional MRPO in FEKO, which confirms the accuracy of the implementation. The difference is also shown in the figure, and ranges between 1% and 5% — this can be readily controlled via the MLFMM algorithm's parameters.

Furthermore, the runtimes are recorded for the same incident field parameters as above at the three frequencies of 1 GHz, 2 GHz and 3 GHz. Table I shows the results. These results demonstrate the dramatic benefit that the MLFMM-acceleration has on the runtime of the MRPO method.

B. Trihedral

For the trihedral, the frequency is set to 3 GHz and the incident plane wave angles are $\theta = 45°$ and $\phi = 45°$.

Figure 3 shows the MLFMM-accelerated MRPO results as the total number of reflections is varied. It can be seen that the results stabilize after three reflections, as expected. With

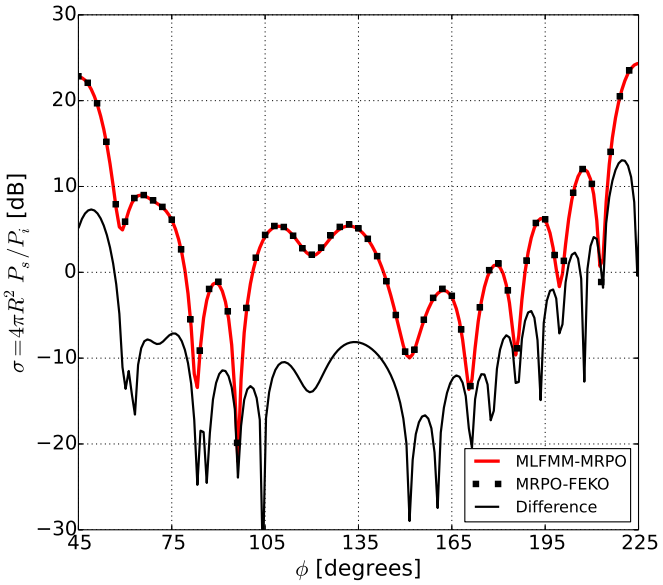

Fig. 2. Dihedral scattered far field results. Three reflections are included for the MRPO results. $\theta = 90°$.

TABLE I
MRPO RUNTIME RESULTS FOR THE DIHEDRAL GEOMETRY, WHEN INCLUDING A TOTAL OF THREE REFLECTIONS. ALL RESULTS WERE GENERATED ON THE SAME PLATFORM.

Frequency	# elements	MRPO-FEKO	MLFMM-MRPO
1 GHz	6, 136	39.49 s	3.076 s
2 GHz	24, 442	613.70 s	12.455 s
3 GHz	55, 612	3251.93 s	31.559 s

the total number of reflections fixed at 4, Figure 4 compares the MRPO to the full MoM. Reasonably accurate results are obtained in the most prominent lobes of the pattern. MRPO accuracy is expected to increase with increased frequency.

IV. CONCLUSION

This paper focussed on the MRPO method for scattering analysis of conducting objects, with surface current represented by RWG basis functions on a mesh of triangle elements. Preliminary results have been presented which show that the MLFMM can be used to dramatically accelerate the recursive calculation of the surface current in the MRPO method, when the scattering objects do not support any internal shadowing.

ACKNOWLEDGMENT

This work was funded by Altair Development S.A. (Pty) Ltd, developers of the EM simulation software suite FEKO.

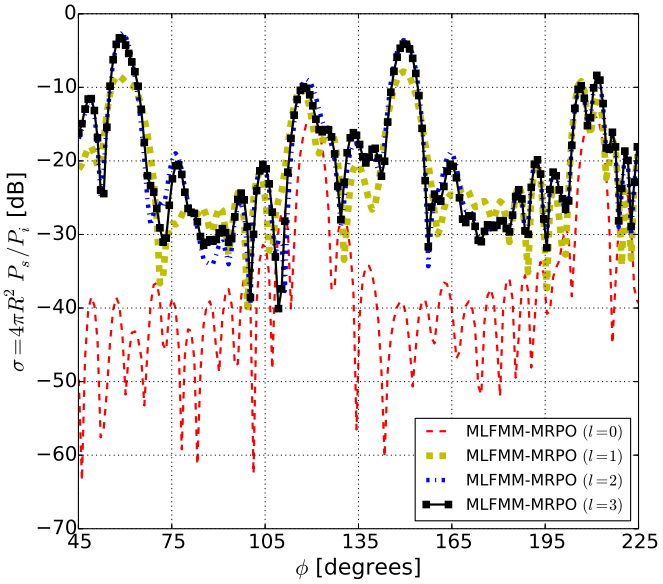

Fig. 3. MLFMM-MRPO scattered far field results, when including a varying total number of reflections; $\theta = 90°$.

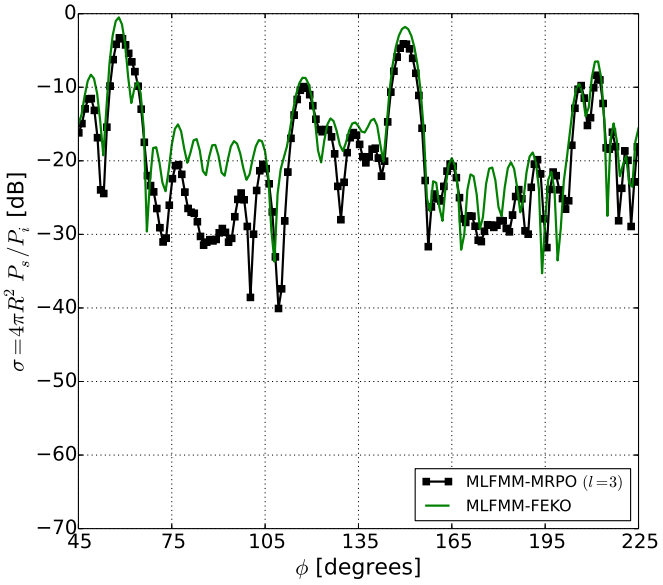

Fig. 4. MLFMM-MRPO vs. MLFMM-FEKO scattered far field results, when including a total number of 4 reflections for the MRPO; $\theta = 90°$.

REFERENCES

[1] D. Elking, J. Roedder, D. Car, and S. Alspach, "A review of high-frequency radar cross section analysis capabilities at McDonnell Douglas Aerospace," *IEEE Antennas Propag. Mag.*, vol. 37, no. 5, pp. 33–42, 1995.

[2] M. F. Cátedra, C. Delgado, S. Luceri, O. G. Blanco, D. Adana, and F. Sáez, "Physical optics analysis of multiple interactions in large scatters using current modes," *IEEE Trans. Antennas Propagat.*, vol. 54, no. 3, pp. 985–994, 2006.

[3] R. J. Burkholder, "A fast and rapidly convergent iterative physical optics algorithm for computing the RCS of open-ended cavities," *Applied Computational Electromagnetics Society Journal*, vol. 16, no. 1, pp. 53–60, 2001.

[4] F. Obelleiro-Basteiro, J. Luis Rodriguez, and R. J. Burkholder, "An iterative physical optics approach for analyzing the electromagnetic scattering by large open-ended cavities," *IEEE Trans. Antennas Propagat.*, vol. 43, no. 4, pp. 356–361, 1995.

[5] H. Ling, R.-C. Chou, and S.-W. Lee, "Shooting and bouncing rays: Calculating the RCS of an arbitrarily shaped cavity," *IEEE Trans. Antennas Propagat.*, vol. 37, no. 2, pp. 194–205, 1989.

[6] U. Jakobus and F. M. Landstorfer, "Improved PO-MM hybrid formulation for scattering from three-dimensional perfectly conducting bodies of arbitrary shape," *IEEE Trans. Antennas Propagat.*, vol. 43, no. 2, pp. 162–169, 1995.

[7] W. C. Chew, E. Michielssen, J. Song, and J. Jin, *Fast and efficient algorithms in computational electromagnetics*. Artech House, Inc., 2001.

[8] Altair Engineering Inc., *FEKO User's Manual Suite 7.0*, Altair Development S.A. (Pty) Ltd., August 2014.

Appendix G

Conference paper — fast shadowing and MRPO [48]

D. P. Xiang and M. M. Botha, **"Acceleration of mesh-based physical optics for electromagnetic scattering analysis,"** in *7th European Congress on Computational Methods in Applied Sciences and Engineering (ECCOMAS2016)*, Crete Island, Greece, June 2016, 9 pages.

Acceleration of mesh-based physical optics for electromagnetic scattering analysis

Dao P. Xiang[1], Matthys M. Botha[2]
[1]Dept of Electrical and Electronic Engineering, Stellenbosch University, South Africa
[2]Dept of Electrical and Electronic Engineering, Stellenbosch University, South Africa
E-mail: mmbotha@sun.ac.za

Abstract

This work is concerned with scattering analysis of electrically large, conducting objects, using the physical optics (PO) approximation. Such analysis is important for radar cross section (RCS) calculations. Scattering objects are represented by a mesh of sub-wavelength sized triangle elements. Upon the mesh, the induced surface current density is represented by standard divergence-conforming basis functions. This is the mesh-based PO approach. It can be applied to take only a single reflection off the scatterer into account, as well as to take multiple, internal reflections into account. Both plane wave and point source illuminations are considered. The paper discusses computational challenges with regards to the fast and robust implementation of mesh-based PO analysis methods. These challenges are shadowing determination, in which the visibility of mesh elements with respect to source locations must be determined, as well as the fast evaluation of observed fields. A multi-level, buffer-based algorithm for efficient, single-reflection shadowing determination is outlined. It is also shown how the recursive field calculations required in the multiple-reflection PO, can be accelerated with the aid of the multilevel, fast multipole method (MLFMM), when the scattering object does not support any internal shadowing. Preliminary results illustrate the current status of this ongoing work on the acceleration of mesh-based PO analysis methods.

Index Terms

Computational electromagnetics, Electromagnetic scattering, Physical optics (PO), Shadowing determination, Recursive update, Multilevel fast multipole method (MLFMM).

I. INTRODUCTION

This work is concerned with scattering analysis of electrically large, conducting objects, using the physical optics (PO) approximation [1]. Such analysis is important for radar cross section (RCS) calculations. Scattering objects are represented by a mesh of sub-wavelength sized triangle elements. Upon the mesh, the induced surface current density is represented by standard divergence-conforming basis functions also used in the Method of Moments (MoM). This is the mesh-based PO approach [2], [3]. This approach can be applied to take only a single reflection off the scatterer into account (when illuminated by a plane wave or point source [Hertzian dipole]), as well as to take multiple, internal reflections into account. In the multiple-reflection case, the PO approximation is applied iteratively. In the interest of brevity, the paper will only be concerned with the standard RWG-type of mixed first-order, edge-associated basis functions, as employed in e.g. [2].

The paper starts off by briefly reviewing the above mesh-based PO analysis methods in Section II. The computational challenges for the efficient (fast and robust) computer implementation of these methods are also discussed in Section II. These include shadowing determination and the fast evaluation of observed fields. The main contribution of this paper follows in Sections III, IV and V. Solutions are proposed to some of these challenges. Preliminary results are included, to illustrate the current status of this ongoing work on the acceleration of mesh-based PO analysis methods.

II. REVIEW OF MESH-BASED PHYSICAL OPTICS FOR PEC SCATTERERS

A. The PO approximation

Firstly, it is noted that for a magnetic field $\boldsymbol{H}^{\text{inc}}$, incident upon an infinite perfect electrically conducting (PEC) half space, the exact solution of the induced surface current is

$$\boldsymbol{J}_s = 2\hat{n} \times \boldsymbol{H}^{\text{inc}} \tag{1}$$

where $\hat{n}$ is the unit normal vector at the interface, pointing away from the PEC region. This simple result is the inspiration for the PO approximation [1], [4], which states that the surface current on a PEC object can be approximated in terms of the incident magnetic field and the outward-pointing unit vector to the surface, as follows:

$$\boldsymbol{J}_s = \begin{cases} 2\hat{n} \times \boldsymbol{H}^{\text{inc}} & \text{for visible surfaces} \\ 0 & \text{for shadowed surfaces.} \end{cases} \tag{2}$$

The status of a location as being visible or in shadow, is established by determining whether there is line-of-sight visibility to the source, or not. For an incident plane wave as source, this means visibility towards infinity, along the negative of the incident direction. For a point source, visible status means an unobstructed view of the source point, from the given position on the scatterer surface.

B. The single-reflection PO method

The single-reflection PO method (SRPO) employs the PO approximation directly, to establish an approximate solution for the induced current density on a PEC scatterer. In order to achieve this, two tasks must be performed: (i) shadowed and visible parts of the scatterer must be identified; and (ii) in the visible regions, the known incident field must be mapped to a description of the surface current. The second of these tasks is quite straightforward in the mesh-based PO context: a local projection procedure is used to obtain the RWG basis function coefficient values, such that they best approximate the tangential components of the incident field according to (2) (see e.g. [2]). This is an $O(N)$ task, where N denotes the number of mesh elements. The first task is much more challenging, with regards to computational efficiency.

C. The multiple-reflection PO method

The first step in the multiple-reflection PO method (MRPO) is to calculate the SRPO solution. This solution is denoted by $\boldsymbol{J}^{(0)}$. It is obtained in the illuminated regions of the scatterer's surface, according to the PO approximation and the local projection procedure:

$$\boldsymbol{J}^{(0)}(\boldsymbol{r}) = 2\hat{n} \times \boldsymbol{H}^{i}(\boldsymbol{r}). \tag{3}$$

In the case where multiple reflections are important, the cumulative radiation from parts of this current distribution is significant towards other parts of the object. Additional currents are induced according to the PO approximation, which represent a second reflection. In general, the current after l additional reflections is found by way of the following recursive expression [5]:

$$\boldsymbol{J}^{(l)}(\boldsymbol{r}) = \boldsymbol{J}^{(0)}(\boldsymbol{r}) + 2\hat{n} \times \fint_S \delta(\boldsymbol{r}')\boldsymbol{J}^{(l-1)}(\boldsymbol{r}') \times \hat{R}\frac{e^{-jkR}}{4\pi R}\left(jk + \frac{1}{R}\right) dS' \tag{4}$$

where $\boldsymbol{R} = \boldsymbol{r} - \boldsymbol{r}'$, $R = |\boldsymbol{R}|$, $\hat{R} = \boldsymbol{R}/R$; $\boldsymbol{r}'$ and $\boldsymbol{r}$ relate to the position vectors of the source and observation points, respectively, on the scatterer's surface. The scatterer's surface is denoted by S. The symbol $\fint$ represents the principle value integral. The factor $\delta(\boldsymbol{r}')$ is the shadowing coefficient, which takes on the value of either 1 or 0, depending on whether the current source point is visible to the observation point, or not.

In other words, the currents re-radiate iteratively, to excite a new set of PO currents at each reflection. The iteration process can be stopped after a pre-specified number of reflections based on the number of expected significant reflections supported by a given model, or until an adequately converged solution is obtained.

D. Computational challenges

For the mesh-based SRPO, the main challenge is to determine the shadowing status of each mesh edge, with respect to the illuminating source. A naïve approach would involve considering each edge in turn, and testing all elements for shadowing relative to the source. This would require $O(N^2)$ operations ($O(N)$ tests per edge, of which there are a total of $O(N)$). Given that the other main task is projection, the cost of which is $O(N)$, shadowing is clearly the bottleneck. This cost can be reduced by making use of the field-of-view buffer concept [6], [7], [3]. A buffer plane is defined upon an eikonal surface of the incident wave. This plane is subdivided into buffer boxes and each mesh element is listed in those boxes into which parts of it project. To test the shadowing status of a given point, it is also projected into the buffer to determine the box it falls into. Subsequently, only shadowing checks need to be performed against those elements which are listed for that particular buffer box. The present authors have been working on efficient shadowing algorithms which employ this general concept [8], [9]. The present status of this ongoing work is reviewed in Sections III and IV.

For the mesh-based MRPO, there are two main challenges. The first challenge is the calculation of subsequent incident fields due to the induced surface current, by way of (4). When using standard integration, the cost of this step is $O(N^2)$, since at every mesh edge, the field must be calculated due to all other mesh elements. This step could be accelerated with a fast field calculation method. Indeed, this has been done using the fast far field approximation (FaFFA) [10], [11], which reduces the cost to $O(N^{5/3})$. However, seeing that field calculation at a specified set of points can be viewed as a Method of Moments (MoM) type of matrix-vector product, the multilevel, fast multipole method (MLFMM) [12] could be used to reduce the cost of this step even further, to $O(N \log N)$. Ongoing work in this direction, is reviewed in Sections V.

The second challenge for the mesh-based MRPO, is efficient shadowing determination. The shadowing status of all mesh edges, as observed from every mesh edge projection point, is required. A naïve approach would require $O(N^2)$ operations for every projection point (as explained above) and hence $O(N^3)$ operations in total. Furthermore, the shadowing data would require $O(N^2)$ storage space, except if calculated on-the-fly. To reduce this cost to a practically feasible scale, is a challenging task. There are however various problems of practical interest where all projection points are visible to all induced current sources. In such cases the shadowing information is trivial and acceleration of the field calculations do suffice. In this paper, the application focus of the MRPO is on such cases.

III. ACCELERATION OF SHADOWING DETERMINATION FOR THE SRPO WITH PLANE WAVE ILLUMINATION

A. Method

In this case, the eikonal surfaces are flat planes transverse to the direction of propagation of the incident wave. The buffer plane is chosen to be such a surface. The steps followed in the shadowing determination algorithm are as follows:

1) Triangles are projected into the buffer plane and the overall buffer bounding box is established, as well as bounding boxes for each projected element.
2) The objective of the algorithm is to separate triangles into small groups in the buffer plane, according to a buffer plane subdivision. Therefore, divide the plane into buffer

boxes of which the size is proportional to the average mesh size. If a box is found which contains an excessive number of elements, then that box is again subdivided according to the same procedure. This yields a multi-level subdivision, capable of handling strongly inhomogeneous meshes as well. In case of a homogeneous mesh, only the first-level subdivision is typically necessary.

3) Now project each edge mid-point into the buffer and do shadowing testing against only those elements listed in the specific buffer box. This yield the visibility status of each corresponding, edge-associated basis function.

Above, some technical details of the algorithm are omitted in the interest of brevity. Also, the above description assumes that no grazing incidence is present. Grazing incidence occurs when the propagation direction of the incident plane wave is close to tangential to certain constituent surfaces of the scatterer. In such cases many elements may end up being listed in individual buffer boxes. The grazing triangles must then be handled with a custom procedure, similar to the one noted in [8].

B. Results

Figure 1 shows examples of the meshes used for shadowing evaluation testing. All meshes represent the same simple model, but will serve to illustrate the capabilities of the algorithm. The series of meshes are of a sphere which is inhomogeneously meshed and progressively refined, as explained in the figure. These progressively refined meshes are used to generate the shadowing determination runtime results shown in Figure 2, as a function of the number of mesh elements. On the same computational platform, results were also generated with the commercial mesh-based PO solver available as part of the FEKO software suite [13]. The direction of incidence is set to be aligned with the point around which the mesh is refined. The results show that the proposed, multilevel buffer subdivision scheme is significantly more efficient than the commercial solver. This is due the effective separation of mesh elements in the buffer, through appropriate localized subdivision. The observed time scaling for the proposed method is of $O(N)$.

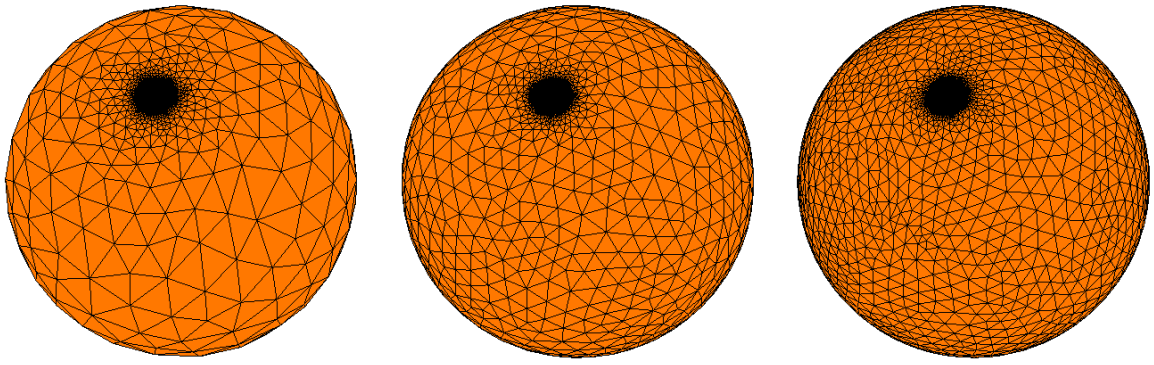

Fig. 1. Progressively refined meshes of a conducting sphere. The sphere has a radius of 1 m. The meshes are all inhomogeneous with a relative element size reduction factor of 100, around a single point.

IV. ACCELERATION OF SHADOWING DETERMINATION FOR THE SRPO WITH POINT SOURCE ILLUMINATION

A. Method

In this case, the eikonal surfaces are spheres centred around the illuminating point source and the spherical coordinate system variables (θ, ϕ) are used to describe point locations in the buffer. Otherwise, the general procedure is the same as discussed above for the plane wave case. It is important to note that even in the case of a homogeneous mesh, the projected

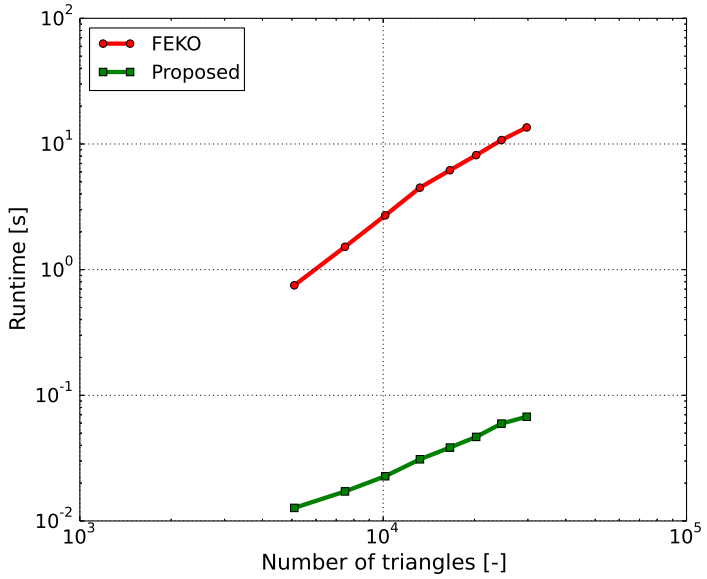

Fig. 2. Shadowing determination runtime as a function of the number of mesh elements, for plane wave illumination of the inhomogeneous meshes shown in Figure 1. The proposed method is compared to a commercial solver.

representation in the buffer plane is often inhomogeneous, due to the specific properties of the spherical coordinate system. This is a further important motivating factor for the recursive buffer subdivision approach. In the interest of brevity, a discussion on the case of grazing incidence for point source illumination will be deferred to a future publication.

B. Results

The set of progressively refined meshes described in Figure 1 is again used. The point source is placed normally above the point on the sphere around which the refinement is centred, at a height of 10^{-2} m. Figure 3 shows the shadowing determination runtime as a function of the number of mesh elements. Again, the results show that the proposed, multilevel buffer subdivision scheme is much more efficient than the commercial solver and that the cost scales as $\mathcal{O}(N)$.

V. MLFMM-BASED ACCELERATION OF INDUCED CURRENT CALCULATION IN THE MRPO

A. Method

To calculate the next solution according to the iterative MRPO expression (4), the observation point $\boldsymbol{r}$ must be placed at each edge mid-point in the mesh. Collectively, this can be expressed as a system of linear equations:

$$I^{(l)} = I^{(0)} + AI^{(l-1)} \tag{5}$$

where $I^{(l)}$ represents the vector of current coefficients after l additional reflections and $I^{(0)}$ represents the vector of current coefficients corresponding to the initial, single-reflection PO current. The dimension of square matrix A is $\mathcal{O}(N)$. The cost of conventionally evaluating the matrix-vector product $AI^{(l-1)}$ is thus $\mathcal{O}(N^2)$.

The matrix A in (5) can be split up into a sparse near-interaction matrix and the remaining far-interaction part, per the specifications of the MLFMM algorithm [12]:

$$I^{(l)} = I^{(0)} + \left(A^{\text{near}} + A^{\text{far}}\right) I^{(l-1)}. \tag{6}$$

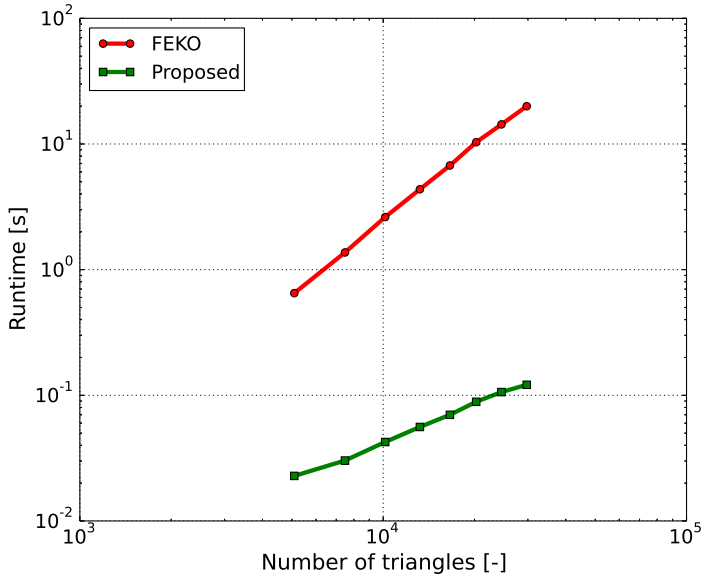

Fig. 3. Shadowing determination runtime as a function of the number of mesh elements, for point source illumination of the inhomogeneous meshes shown in Figure 1. The proposed method is compared to a commercial solver.

The cost of the matrix-vector product $A^{\text{near}}I^{(l-1)}$ is $O(N)$. Using the MLFMM, the matrix-vector product $A^{\text{far}}I^{(l-1)}$ has cost $O(N \log N)$ (see e.g. [12] for further details). This can be compared with the scaling achieved using FaFFA acceleration, which as noted already, is given as $O(N^{5/3})$ in [11].

B. Results

Consider the trihedral structure shown in Figure 4. It is illuminated by a plane wave with incident angles $\theta^{\text{inc}} = 45°$ and $\phi^{\text{inc}} = 45°$. It is homogeneously meshed with mesh size of $\lambda_0/10$, where λ_0 denotes the free space wavelength. On the illuminated side, all triangles are visible to each other, thus shadowing determination is trivial and consequently, the MRPO can be accelerated with the MLFMM in this case. Three reflections are incorporated with the MRPO ($l = 2$). Figure 5 shows how the runtime for the solution scales as a function of the number of mesh elements. Different data points are obtained by varying the excitation frequency (and thus wavelength) and remeshing (the frequency range used is 0.5 GHz to 2.25 GHz). Clearly, the standard MRPO scales as $O(N^2)$, due to the conventional evaluation of the matrix-vector product in (5). The MLFMM-accelerated MRPO has much lower runtime and as N becomes larger, the relative saving becomes increasingly significant. Note that $O(N \log N)$ behaviour cannot be clearly observed in these preliminary accelerated results. This is ongoing work and further tests are still being conducted.

VI. CONCLUSIONS

Computational challenges with regards to the fast implementation of mesh-based PO methods for scattering analysis of conducting objects, were discussed. Both single-reflection and multiple-reflection formulations were considered. These challenges are efficient shadowing determination and efficient calculation of observed fields. A multi-level, buffer-based algorithm for efficient, single-reflection shadowing determination was outlined and results were presented for a strongly inhomogeneous mesh. The results exhibit linear time scaling and are superior to the runtimes achieved with the commercial PO solver in FEKO. It was further shown how the recursive field calculations required in the MRPO, can be accelerated

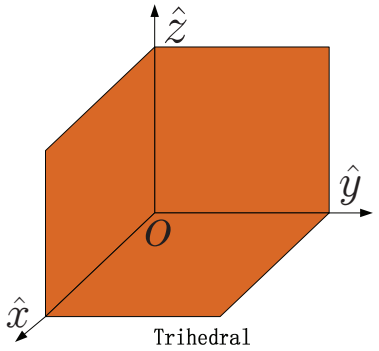

Fig. 4. Conducting plate, trihedral model. The plate dimensions are all 1 m.

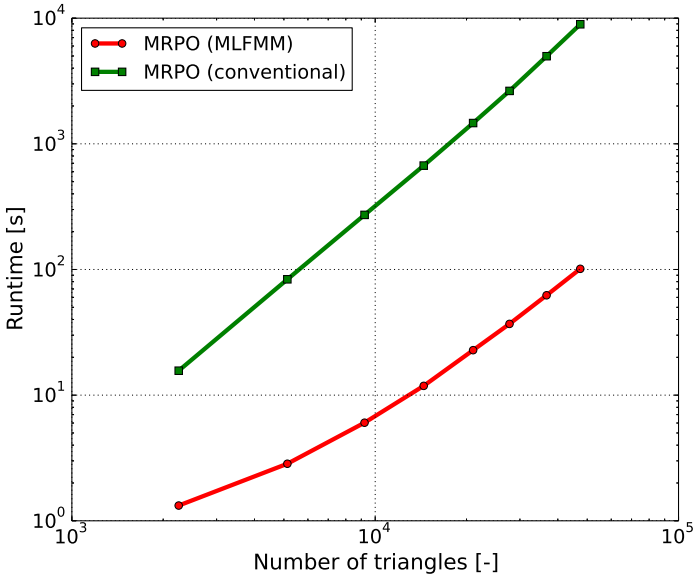

Fig. 5. Runtime as a function of the number of mesh elements, for the conventional and MLFMM-accelerated MRPO implementations.

with the aid of the MLFMM. Preliminary results demonstrate significantly reduced runtime, when the scattering object does not support any internal shadowing.

ACKNOWLEDGMENT

This work was funded by Altair Development S.A. (Pty) Ltd, developers of the EM simulation software suite FEKO.

REFERENCES

[1] N. Bojarski, "A survey of the physical optics inverse scattering identity," *IEEE Trans. Antennas Propag.*, vol. 30, no. 5, pp. 980–989, 1982.

[2] U. Jakobus and F. M. Landstorfer, "Improved PO-MM hybrid formulation for scattering from three-dimensional perfectly conducting bodies of arbitrary shape," *IEEE Trans. Antennas Propagat.*, vol. 43, no. 2, pp. 162–169, 1995.

[3] F.-T. Zha, S.-X. Gong, Y.-X. Xu, Y. Guan, and W. Jiang, "Fast shadowing technique for electrically large targets using z-buffer," *Journal of Electromagnetic Waves and Applications*, vol. 23, no. 2-3, pp. 341–349, 2009.

[4] W. L. Stutzman and G. A. Thiele, *Antenna Theory and Design*. New York: John Wiley and Sons, 2nd ed., 1998.

[5] F. Obelleiro-Basteiro, J. L. Rodriguez, and R. J. Burkholder, "An iterative physical optics approach for analyzing the electromagnetic scattering by large open-ended cavities," *IEEE Trans. Antennas Propagat.*, vol. 43, no. 4, pp. 356–361, 1995.

[6] E. A. Haines and D. P. Greenberg, "The light buffer: A shadow-testing accelerator," *IEEE Computer Graphics and Applications*, pp. 6–16, September 1986.

[7] J. M. Rius, M. Ferrando, and L. Jofre, "GRECO: Graphical electromagnetic computing for RCS prediction in real time," *IEEE Antennas and Propagation Magazine*, vol. 35, no. 2, pp. 7–17, 1993.

[8] D. P. Xiang and M. M. Botha, "Aspects of efficient shadowing calculation for physical optics analysis of meshed objects," in *International Conference on Electromagnetics in Advanced Applications (ICEAA '14)*, pp. 492–495, Aug 2014. Aruba, Dutch Antilles.

[9] D. P. Xiang and M. M. Botha, "Further progress with fast and reliable shadowing determination for mesh-based PO analysis," in *International Conference on Electromagnetics in Advanced Applications (ICEAA '15)*, pp. 958–961, Sept 2015. Torino, Italy.

[10] C.-C. Lu and W. C. Chew, "Fast far-field approximation for calculating the RCS of large objects," *Micro. Opt. Tech. Lett.*, vol. 8, no. 5, pp. 238–241, 1995.

[11] R. J. Burkholder, "A fast and rapidly convergent iterative physical optics algorithm for computing the RCS of open-ended cavities," *Applied Computational Electromagnetics Society Journal*, vol. 16, no. 1, pp. 53–60, 2001.

[12] W. C. Chew, E. Michielssen, J. M. Song, and J. M. Jin, *Fast and efficient algorithms in computational electromagnetics*. Artech House, Inc., 2001.

[13] Altair Hyperworks Version 14.0, "FEKO User Manual," December 2015. http://www.feko.info.